รหัสโครงการ SUT7-706-55-24-01

รายงานการวิจัย

การวิเคราะห์กลไกการระเหยน้ำวัตถุดิบของเหลวที่ใช้กับเครื่องพ่นฝอยสำหรับการผลิตผงแห้งมูลค่าสูง

(Analysis of slurry drying mechanism in industrial spray dryer for production of high value particles)

ได้รับทุนอุดหนุนการวิจัยจาก
มหาวิทยาลัยเทคโนโลยีสุรนารี

ผลงานวิจัยเป็นความรับผิดชอบของหัวหน้าโครงการวิจัยแต่เพียงผู้เดียว

รหัสโครงการ SUT7-706-55-24-01

รายงานการวิจัย

การวิเคราะห์กลไกการระเหยน้ำวัตถุดิบของเหลวที่ใช้กับเครื่องพ่นฝอยสำหรับการผลิตผงแห้งมูลค่าสูง

(Analysis of slurry drying mechanism in industrial spray dryer for production of high value particles)

คณะผู้วิจัย

หัวหน้าโครงการ

Assistant Professor Dr. Boris Golman

สาขาวิชาวิศวกรรมเคมี

สำนักวิชาวิศวกรรมศาสตร์

มหาวิทยาลัยเทคโนโลยีสุรนารี

ได้รับทุนอุดหนุนการวิจัยจากมหาวิทยาลัยเทคโนโลยีสุรนารี ปีงบประมาณ พ.ศ. 2555

ผลงานวิจัยเป็นความรับผิดชอบของหัวหน้าโครงการวิจัยแต่เพียงผู้เดียว

พฤษภาคม 2557

Acknowledgement

The author would like to thank the National Research Council of Thailand for their funding of this research. The assistance of the staff of the Institute of Research and Development and the Institute of Engineering of Suranaree University of Technology in preparing, approving and submitting the research proposal and the final research report is highly appreciated. The author wish to thank Mr. Wittaya Julklang, master course student at the School of Chemical Engineering of Suranaree University of Technology, for his essential role in simulation and preparation of final report.

(Assistant Professor Dr. Boris Golman)

Abstract

Spray drying technology is one of the most popular techniques used for the production of high value particles by transforming slurry droplets into particles. Its ubiquitous applications are found in numerous industries such as food, pharmaceutical, chemical and biological to enhance particle properties, powder handling and storage. However, the scaling-up of spray dryer for industrial implementation customarily requires construction of pilot-plant apparatus which is a time-consuming and costly process. The key problem is lack of reliable mathematical models for dryer design as spray drying is a complex process involving simultaneous heat, mass and momentum transfer between the drying gas and slurry droplets as well as heat and mass transport inside the partly dried agglomerates. This study aims to analyze the drying mechanism of slurry droplets in an industrial scale spray dryer for production of high-value particles.

At first, the comprehensive model is established for description of drying kinetics of a slurry droplet in the constant and falling drying rate periods. The heat and mass transfer resistances are taken into account both inside and outside the droplet together with the movement of evaporation interface as drying progresses. The system of partial differential equations with moving boundary is solved numerically by an implicit finite-difference method. The model is validated by comparison of simulation results with published experimental data. The effects of the drying gas temperature and flow rate, slurry concentration, initial droplet size and porosity of agglomerated product are analyzed on the drying kinetics of the droplet containing nanosized particles.

Thereupon, the mathematical model is developed to simulate the drying of slurry droplets in the industrial scale spray dryer. The developed model of drying kinetics of a slurry droplet is incorporated into the model of spray dryer to simulate the velocity, humidity and temperature profiles of drying gas and droplets along the axial distance of the drying chamber as well as the distributions of temperature and water vapor concentration inside the droplet at any axial position in the dryer. The effects

of the operational parameters such as drying air temperature and flow rate, slurry concentration, droplet size and the nozzle type are investigated on the drying behavior of slurry droplets of nanosized silica in the spray dryer. Finally, the drying mechanism of high-value hydroxyapatite particles is examined numerically in the industrial spray dryer and compared with that of silica droplets of the same final size.

The results of the present analysis are intended to be used for optimization of spray dryers utilized in various industries.

บทคัดย่อ

เทคโนโลยีการอบแห้งแบบพ่นฝอย เป็นหนึ่งในเทคนิคที่ได้รับความนิยมสำหรับใช้ในการผลิตอนุภาคมูลค่าสูงโดยการเปลี่ยนรูปของหยดสเลอรีไปเป็นอนุภาค เพื่อเพิ่มคุณสมบัติของอนุภาค การขนถ่ายอนุภาคและการจัดเก็บ เครื่องอบแห้งแบบพ่นฝอยถูกพบว่ามีการใช้งานที่แพร่หลายในอุตสาหกรรมหลากหลายประเภท เช่น อุตสาหกรรมอาหาร อุตสาหกรรมยา อุตสาหกรรมเคมีและชีวภาพ เป็นต้น อย่างไรก็ตาม การขยายขนาดของเครื่องอบแห้งแบบพ่นฝอยในระดับอุตสาหกรรมโดยทั่วต้องใช้การสร้างโรงงานต้นแบบ ซึ่งเป็นกระบวนการที่เสียค่าใช้จ่ายสูงและต้องใช้เวลามาก หัวใจสำคัญของปัญหานี้คือการขาดแคลนแบบจำลองทางคณิตศาสตร์ที่มีความน่าเชื่อถือสำหรับออกแบบเครื่องอบแห้งแบบพ่นฝอย เนื่องจากการอบแห้งแบบพ่นฝอยเป็นกระบวนการที่ซับซ้อนที่เกี่ยวข้องกับการถ่ายเทความร้อน การถ่ายเทมวล และการถ่ายเทโมเมนตัม ระหว่างก๊าซอบแห้งและหยดของสเลอรี รวมถึงการขนส่งความร้อนและมวลภายในอนุภาคบางส่วนที่แห้งแล้วในเวลาเดียวกัน งานวิจัยนี้จึงมีวัตถุประสงค์เพื่อที่จะวิเคราะห์กลไกการอบแห้งของหยดสเลอรีในเครื่องอบแห้งแบบพ่นฝอยระดับอุตสาหกรรมสำหรับการผลิตอนุภาคมูลค่าสูง

ในขั้นแรก แบบจำลองที่มีเนื้อหาคลอบคลุมสำหรับใช้อธิบายจลนศาสตร์การอบแห้งของหนึ่งหยดสเลอรีในช่วงของการอบแห้งคงที่และช่วงของการอบแห้งลดลงได้ถูกสร้างขึ้น ความต้านทานการถ่ายเทความร้อนและมวลทั้งภายในและภายนอกของหยดสเลอรีได้ถูกนำเข้ามาพิจารณาร่วมด้วยกับการเคลื่อนที่ของพื้นผิวการระเหยเนื่องจากความต่อเนื่องของการอบแห้ง ระบบของสมการเชิงอนุพันธ์ย่อยร่วมกับขอบเขตที่เคลื่อนที่ได้ถูกนำมาใช้ในการแก้ปัญหาเชิงตัวเลขโดยระเบียบวิธีผลต่างสืบเนื่องแบบปริยาย แบบจำลองที่สร้างขึ้นถูกตรวจสอบโดยการเปรียบเทียบกับข้อมูลการทดลองที่ถูกตีพิมพ์ ผลกระทบของ อุณหภูมิและอัตราการไหลของก๊าซอบแห้ง ความเข้มข้นของสเลอรี ขนาดของหยดเริ่มต้น และช่องว่างภายในของอนุภาคที่เกิดรวมตัวกันแล้ว ได้ถูกนำมาวิเคราะห์ในจลนศาสตร์ของการอบแห้งของหยดสเลอรีที่มีอนุภาคขนาดนาโนบรรจุอยู่ภายใน

ในขั้นต่อมา แบบจำลองทางคณิตศาสตร์เพื่อใช้ในการจำลองการอบแห้งของหยดสเลอรีในเครื่องอบแห้งแบบพ่นฝอยในระดับอุตสาหกรรมได้ถูกพัฒนาขึ้น โดยที่แบบจำลองจลนศาสตร์การอบแห้งของหนึ่งหยดสเลอรีที่ถูกสร้างขึ้นได้ถูกรวมเข้าไปในแบบจำลองของเครื่องอบแห้งนี้ด้วย เพื่อใช้จำลองรูปแบบของ ความเร็ว ความชื้น และอุณหภูมิของก๊าซอบแห้งและหยดของสเลอรีตลอดทั้งระยะทางตามแนวแกนของห้องอบแห้ง ตลอดทั้งการกระจายตัวของอุณหภูมิและความเข้มข้นของไอน้ำภายในหยดสเลอรีที่ตำแหน่งต่างๆตามแนวแกนภายในเครื่องอบแห้ง ผลกระทบของตัวแปรปฏิบัติการต่างๆ เช่น อุณหภูมิและอัตราการไหลของก๊าซอบแห้ง ความเข้มข้นของสเลอรี ขนาดของ

หยดสเลอรี และชนิดของหัวฉีด ได้ถูกศึกษาในพฤติกรรมการอบแห้งของหยดสเลอรีของนาโนซิลิกาในเครื่องอบแห้งแบบพ่นฝอย

ในขั้นตอนสุดท้าย กลไกการอบแห้งอนุภาคมูลค่าสูงของไฮดรอกซีแอปาไทต์ ได้ถูกศึกษาเชิงตัวเลขในเครื่องอบแห้งแบบพ่นฝอยระดับอุตสาหกรรม และถูกเปรียบเทียบกับผลการศึกษาของซิลิกาที่ขนาดของอนุภาคสุดท้ายเท่ากัน

ผลของการวิเคราะห์จากงานวิจัยนี้ มีจุดประสงค์ที่จะใช้สำหรับการหาค่าที่เหมาะสมที่สุดของเครื่องอบแห้งแบบพ่นฝอยที่มีการใช้งานในอุตสาหกรรมที่หลากหลาย

List of Figures

List of Tables

มหาวิทยาลัยเทคโนโลยีสุรนารี

Nomenclature

A_i	coefficient of system of linear equations Eq. (124)
A_p	droplet projected area, m^2
B_i	coefficient of system of linear equations Eq. (124)
a	droplet acceleration, m/s^2
b	thickness of liquid film at nozzle orifice, m
C	concentration, $kmol/m^3$
c	dimensionless concentration of water vapor
C_D	drag force coefficient
C_i	coefficient of system of linear equations Eq. (124)
Cp	heat capacity, J/(kg K)
D_{cr}	effective diffusivity of water vapor in crust layer, m^2/s
D_i	coefficient of system of linear equations Eq. (124)
D_{wv}	diffusivity of water vapor in air, m^2/s
$D_{3,2}$	Sauter mean droplet diameter, m
d	diameter of nozzle wheel, m
d_o	nozzle orifice diameter, m
d_p	droplet diameter, m
F	force, N
F_b	buoyant force, N
F_c	Coriolis force, N
F_d	drag force, N
F_r	centrifugal force, N
g	gravitational acceleration, m/s^2
H_{air}	air humidity, $kg_{lv}/kg_{dry\ gas}$
h	height of drying chamber, m
h_r	height of vane of rotary nozzle, m

I_{max}	maximum number of iterations in Eq. (143)
i	enthalpy, J/kg
J_{max}	maximum number of iterations in Eq. (178)
K_{max}	maximum number of iterations in Eq. (176)
k	thermal conductivity, W/(m K)
k_h	convective heat transfer coeffcient, W/(m^2 K)
k_m	convective mass transfer coeffcient, m/s
M_l	molecular weight of water, kg/kmol
m_p	mass of droplet, kg
N	nozzle wheel rotation speed, r.p.s.
n	number of vanes of rotary nozzle
N_A	mass flux, kmol/m^2 s
Nu	Nusselt number
P^{vap}	vapor pressure of water, atm
Pr	Prandtl number
Q	slurry volumetric flow rate, m^3/s
q	heat flux, W/m^2
R	droplet radius, m
r	radial position in droplet, m
r_c	radial position of droplet in drying chamber, m
r_o	nozzle orifice radius, m
r_{wd}	nozzle wheel diameter, m
R_{gas}	universal gas constant, atm m^3/kmol K
Re	Reynolds number
s	position of evaporation interface, m
s'	dimensionless position of evaporation interface
Sc	Schmidt number
Sh	Sherwood number

T	temperature, K
t	time, s
$T_{f,init}$	droplet temperature at the end of constant rate period, K
U_{gi}	gas velocity in i direction, m/s
U_{pi}	droplet velocity in i direction, m/s
$\dot{V}_{\text{air}}$	volumetric flow rate of air in nozzle, m^3/s
$\dot{V}_{\text{fluid}}$	volumetric flow rate of fluid in nozzle, m^3/s
V_1	liquid velocity at nozzle inlet, m/s
v_{rel}	relative velocity in Eq. (3), m/s
w	mass flow rate, kg/s
W_t	droplet weight, mg
$W_{t,crit}$	critical droplet weight, mg
$W_{t,final}$	final droplet weight, mg
$W_{t,init}$	initial droplet weight, mg
X	solid moisture content on wet basis, kg_{water}/kg_{slurry}
Y	humidity of drying medium, $kg_{water}/kg_{dry\ air}$

Greek Symbols

α_{1-5}	model parameter
β_{1-7}	model parameter
δ	incremental decrease of interface position
ε	porosity
ζ	dimensionless radial position in falling rate period
θ	dimensionless temperature
θ	half spray angle
λ_l	latent heat of evaporation, J/(kg K)
μ	viscosity, kg/(m s)
ξ	dimensionless radial position in constant rate period

π	π number
ρ	density, kg/m^3
σ	fluid surface tension, N/m
τ	droplet residence time, s
Φ_s	percent tolerance in Eq.(177)
Φ_T	percent tolerance in Eq.(178)
Φ_ξ	percent tolerance in Eq.(144)

Subscripts

av	average
co	core
cr	crust
fp	final product
gas	gas
H	humid drying medium
in	inner
$init$	initial
l	liquid
lv	water vapor
mx	air-water vapor mixture
out	outer
s	solid
sl	slurry
0	inlet

Contents

1 Introduction

1.1 Background of the study

The production of particles in submicrometer and nanometer size ranges has increased greatly in recent years because of their superior physical and chemical properties allowed for broad application in manufacturing of high-value functional materials (Bhushan et al., 2007). However, nanoparticles are difficult to handle in industrial scale production of advanced material (Iskandar et al., 2001) and their effects on the health and environment becomes of serious concern (Lam et al., 2006). Due to problems mentioned above, attempts to produce nanoparticle agglomerates of size larger than submicrometer were reported recently (Suh et al., 2006). The handing, processing and separation of particles in this range is easier giving them good potential for industrial use (Iskandar et al., 2001, Iskandar et al., 2007).

Spray drying is an efficient method of slurry drying due to the large surface area available for heat and mass transfer as a result of atomizing the slurry into very small droplets (Mujumdar,2007). Currently, agglomerates of fine particles produced by spray drying have found expanding applications in pharmaceutical, food, agriculture and chemical industries.

Spray drying is a complex process involving simultaneous heat, mass and momentum transfer between the drying gas and droplets as well as the mass and heat transfer in the droplet complicated by formation of solid phase during drying etc. (Masters, 1985). The conventional way to scaling-up the spray dryer involves construction of pilot-scale apparatus that requires considerable financial expenditures as well as consumes a lot of time. Therefore, there is a need in developing of reliable mathematical models of spray drying process based on which the scaling-up could be done, instead of construction of pilot-scale equipment.

Theoretical models of drying of a slurry droplet are mainly based on the droplet average temperature, and the moisture concentration and temperature distributions

within the droplet are considered only in the crust region during the final drying period (Mezhericher et al., 2010). Therefore, there is a need to develop a detail model capable to describe the temperature and moisture distributions within the slurry droplet during all periods of drying.

The flow patterns of drying gas and slurry droplets inside the spray chamber are complex and scaling-up spray dryers is a challenging task due to the variety of length and velocity scales, i.e. the chamber diameter, droplet diameters and atomizer dimensions (Masters, 1985). The Computational Fluid Dynamics (CFD) has particularly been applied to spray dryers, due partly to the complexity of the gas and particle flow patterns and partly to the overall complexity of the spray drying process (Oakley, 1994; Langrish, 2007). However, CFD simulations requires some experience in the programming and calculation of systems with distributed parameters as well as extremely long computational time for large-scale 3D flows. Furthermore, only simple models of drying kinetics of a slurry droplet have been combined with CFD models. Therefore, there is a need to develop models of spray dryer that include advanced modeling of drying kinetics for design and optimization of spray drying process

1.2 Aims of this research

The main aim of this research is to analyze the drying mechanism of slurry droplets in an industrial scale spray dryer for production of high-value particles. For this purpose, the first task of the present research is to develop the detail mathematical model for drying a slurry droplet including simulation of the heat and mass transfer inside the droplet. The effects of wide range of operational conditions and particle morphology is to be analyzed on the drying behavior of a slurry droplet.

The second task is to formulate the mathematical model of spray dryer based on the mass, heat and momentum balances for the drying gas and slurry droplets. Using the developed models, the detail analysis is to be carried out on influences of operational parameters, particle morphology and different nozzle types on the drying

characteristics of slurry droplets in the industrial scale spray dryer. Finally, the formation of hydroxyapatite agglomerates, as an example of high-value particles, is to be investigated by spray drying.

1.3 Scope of research

The research consisted of two major parts. The first part dealt with modeling of drying behavior of a slurry droplet. This step is essential to ensure the correct description of drying rate hindered due to the presence of solids as the drying rate of high-value materials, such as pharmaceuticals or food additives, produced in the small scale dryers could be limited by the droplet drying rate. The drying kinetic model is also required for correct prediction of droplet temperature and moisture content to avoid possible deposition and accumulation of solid on dryer walls. The detail models were developed for description of the temperature and moisture distributions within the slurry droplet during the first (constant rate) and the second (failing rate) drying periods. The numerical algorithms were derived for solution of partial differential equations with moving boundaries. The results of model simulations were compared with experimental data published in the literature. In addition, the influence of operational conditions and particle morphology on the drying kinetics of a slurry droplet was studied in this work.

The modeling of a spray dryer was considered in the second part of this project. In this part, the models of drying kinetics of a slurry droplet developed in the first part were incorporated into the heat, mass and momentum balances of the spray dryer. The effect of operational parameters, particle morphology and different nozzle types were investigated on the drying characteristics of slurry droplets in the spray dryer. The formation of high-value hydroxyapatite agglomerates was studied in the industrial scale spray dryer.

มหาวิทยาลัยเทคโนโลยีสุรนารี

2 Literature Review

2.1 Application of spray drying for production of advanced materials

Recently, there are many publications in scientific literature on application of agglomerates of fine particles produced by spray drying for manufacturing of high value products in food, pharmaceutical and chemical industries.

Arujo et al. (2010) successfully prepared the ternary solid dispersions of herbal drug using the spray drying technology. This method is more efficient in preparation of small size primary particles than the conventional milling process. The fine particles are required for improving the drug bioavailability. Also, by formation of agglomerates of primary particles, it is possible to improve the handling of drug particles. Spray drying has also been used for the preparation of microencapsulated active pharmaceutical ingredients (Riveros et al., 2009), biopharmaceuticals (Ameri M. and Maa Y.-F., 2006), special drug delivery systems (Re, 2006), etc.

Researchers at the Center of Excellence in Particle Technology of Chulangkorn University reported the numerous applications of spray drying in the food and agricultural industries. For example, the microencapsulation of extracted citronella oil with rice starch to be used as a main ingredients in mosquitoes-repelling products (Singkhimuk et al., 2010), the microencapsulation of phytase and multiple enzymes for animal feed additives (Klinkulabhira et al., 2010), the encapsulation of lemongrass oil with modified starch for flavor additives (Kaewpanha et al., 2010) were successfully carried out using the spray drying technology.

Okuyama et al. (2006) reviewed publications on application of spray drying for generation of various inorganic functional particles from carbon nanotubes to raw material for lithium-ion batteries.

Several developments of the technique involving spraying of liquid or slurry feed have been reported: spray pyrolysis, spray drying, flame spray, low pressure spray, and

electro spray (Iskandar, 2009). All these processes are similar as they are based on the same principle of formation of droplets by spraying feed material dissolved or dispersed in the liquid phase. The spray drying technology is well-trusted in practical uses, which has been confirmed by its use in the manufacturing of dried food, fertilizers, oxide ceramics, and pharmaceuticals. A large number of the applications of this method have been reported, in which more than 15,000 industrial-size spray dryers are currently in operation. This number would approximately double if the use in pilot plants and laboratories is added to the calculation (Wange et al., 2009).

The spray drying is similar to other types of spray method. The ability to produce agglomerates of spherical shape and relatively narrow size distribution with average diameter in the size range from several micron to several hundred micron is one of the main advantages of this method. Other merit gained from this method is that when the feed suspension consists nanoparticles (primary particles), the resulting agglomerated particles are comprised of nanoparticles that form a nanostructured powder. Therefore, the spray-drying method may be suitable for consolidating nanoparticles into macroscopic compacts, that possess nanoscale properties.

2.2 Spray drying process

In a typical spray drying operation, a liquid or slurry feedstock is sprayed into a drying chamber where the hot stream of the drying medium of low moisture content is supplied. Atomization of the feed into small droplets generates the large surface area for both heat and mass transfer. Heat supplied by drying medium is used for evaporation of liquid within the droplets and the generated vapor is transferred to the medium. The agglomerated particles are formed during drying and finally they are collected as a dry powder. The drying proceeds until the desired moisture content in the dried agglomerates is achieved. Process parameters such as inlet and outlet temperatures, humidity of the drying medium, liquid feed rate and the atomization pressure influence the properties of produced agglomerates. The spray drying is a

continuous process that can be scaled up and down to suit the prescribed capacity and tuned to satisfy the requirements on product size distribution.

The spray drying system comprises of feed preparation unit, atomizer, drying medium heater and distributor, drying chamber, system for powder recovery and exhaust drying medium cleaning, and it can operate on an open cycle or a closed cycle (Masters, 2004). Typically the industrial spray dryers use open cycle systems for drying of water based feeds. Air for drying is drawn from atmosphere and the exhaust air is discharged to atmosphere. The product agglomerates are recovered in a cyclone and the exhaust air is cleaned from the dust using combinations of bag filters, electrostatic precipitators and scrubbers. Direct and indirect heating are applied for heating the drying gas.

Closed cycle spray dryers are utilized for evaporation of flammable solvents and drying of toxic or oxygen sensitive products in order to recover the evaporated solvent and to avoid atmospheric pollution. An inert gas such as nitrogen is usually used in such system. The closed cycle systems are equipped with the indirect heaters of drying medium and the condenser of solvent vapor in addition to the cyclone, bag filter and wet scrubbers.

The spray drying consists of four process stages: atomization, spray-air contact, drying and agglomerate formation, and product agglomerate separation from the drying air. In the first stage, the liquid feed is atomized into a spray of droplets. The are three basic designs of atomizers, classified by the source of energy used in the droplet formation process: centrifugal energy in rotating wheel or disc atomizers, kinetic energy in pneumatic nozzle and pressure energy in pressure nozzle atomizers. Atomizers are selected according to the desired droplet sizes and throughput, as summarized in Table 1 (Masters, 2004).

For drying applications using rotary atomization, the liquid feed enters at the centre of high speed rotating wheel, accelerates across the vanes forming a thin film of liquid that is ejected at the wheel rotating speed and rapidly disintegrates into droplets form-

Table 1: Median droplet size of different atomizers

Atomization device	Median Droplet size (μm)
Rotary nozzle (wheel)	10 - 200
Pressure nozzle	30 - 350
Pneumatic nozzle (two/thee-fluid)	5 - 100

ing a wide jet with an umbrella shape (Masters, 2004). The droplet size distribution depends on the rotating speed and geometry of the rotary atomizer, and on the flow rate and physical properties of liquid (King et al., 1984). The Sauter mean diameter $D_{3,2}$, defined as the ratio of the total droplets volume to the total droplets surface, is often used to characterize the average size of droplets. The empirical correlation is proposed to evaluate the Sauter mean diameter for rotary atomizer (Mujumdar, 1995)

$$D_{3,2} = 1.62 \cdot 10^{-3} N^{-0.53} {w_{sl}}^{0.21} (2r_{wd})^{-0.39}, \tag{1}$$

where $D_{3,2}$ is the Sauter mean droplet diameter in meters, N is the wheel rotation speed in r.p.s. and r_{wd} is the wheel diameter.

The size distribution of droplets generated by rotary atomizer is mainly controlled by the wheel velocity. The rotary atomizer is more flexible than other types of atomizers, because it can operate at different liquid feed rates while keeping the droplet size distribution nearly constant, it is able to use the concentrated slurry and the slurry feed containing abrasive solids, and it can handle the large amount of feed.

As a disadvantage, the rotary atomizer consumes more energy than the pressure nozzle and it requires the drying chamber of a large diameter to avoid collisions between the radially ejected partially-dried droplets and the chamber wall. Another problem is related to the possible air entrapment into the droplets due to the aspiration of air by the rotating wheel.

For pressure nozzle atomization, the spray is formed owing to the conversion of the pressure energy into kinetic energy as liquid is forced through an orifice by a high pressure pump. The liquid enters tangentially into the nozzle, rotates inside and exits

from the orifice forming a cone.

The size distribution of droplets generated by pressure nozzle is more uniform than the one produced by rotary atomizer. The pressure applied to the liquid influences the angle of the cone and the droplet size. The Sauter diameter can be estimated by using the following empirical correlations (Mujumdar, 1995)

$$D_{3,2} = 286\left[\left(2.54 \cdot 10^{-2}\right) d_0 + 0.17\right] \exp\left[\frac{39}{U_{px}} - \left(3.13 \cdot 10^{-3}\right) V_1\right], \tag{2}$$

where $D_{3,2}$ is the Sauter mean droplet diameter in micron, d_o is the orifice diameter, V_1 is the inlet velocity of the slurry and U_{px} is the axial droplet velocity.

A single pressure nozzle can handle a liquid feed rate up to 100 kg/h. For this reason several nozzles are frequently used inside industrial spray drying towers.

The main advantages of the pressure nozzle are the formation of air-free droplets, the possibility of designing the multiple spray systems to avoid collisions between droplets, the small diameter of the drying chamber, and the low cost due to the absence of moving parts.

One disadvantage of the pressure nozzle is that the variation of the liquid flow rate modifies the droplet size distribution with higher flow rate leading to formation of smaller droplets. Also, the concentrated slurry can block the outlet orifice and the abrasive particles can damage the nozzle.

The pneumatic nozzle atomization uses compressed air to atomize the liquid. The Sauter droplet diameter produced by pneumatic nozzle atomization follows the relation (Mujumdar, 1995)

$$D_{3,2} = \frac{535 \cdot 10^3 \sqrt{\sigma}}{v_{\text{rel}} \sqrt{\rho}} + 597\left(\frac{\mu}{\sqrt{\sigma\rho}}\right)^{0.45} \cdot \left(\frac{1000 \dot{V}_{\text{fluid}}}{\dot{V}_{\text{air}}}\right), \tag{3}$$

where σ, ρ and μ are the fluid surface tension, density, and viscosity, respectively. v_{rel} is the relative velocity, $\dot{V}_{\text{fluid}}$ and $\dot{V}_{\text{air}}$ are the volumetric flow rates of fluid and air, respectively.

With two-fluid nozzles it is possible to maintain the same droplet size distribution for different liquid flow rates by adjusting the compressed air flow rate.

The main disadvantages of this kind of atomizer are the high cost of compressed air and the relatively low liquid throughput.

The second process stage of spray drying involves the contact of spray with drying air, mixing and droplet flow. The mode of contact between spray droplets and drying air controls the rate of evaporation, the final moisture content, the droplet residenc

In a co-current flow, the feed is sprayed in the same direction as the flow of the heated drying medium in the drying chamber. The droplets of high moisture content contact with the hot drying medium resulting in an optimal solvent evaporation for spray drying of heat-sensitive materials (Master, 2002; Huang and Mujumdar, 2003), such as enzymes, peptides and proteins.

In a counter-current flow design, the atomized feed and drying medium move in the opposite direction through the drying chamber. The agglomerates which are almost dried contact with hot air yielding in a product of low moisture content and consequently of good flowability. This contact mode is suitable for drying of non-heat-sensitive products (Masters, 2002).

Spray dryer designs that combine co-current and counter-current flow modes are classified as mixed flow spray dryers. The coarse free-flowing spray dried agglomerates can be produced in such systems using the drying chambers of relatively small dimensions. In mixed flow systems, partially dried particles contact with hot drying medium near the distributor.

The third process stage of spray drying combines drying and particle formation. Evaporation of the solvent takes place immediately after contact between spray droplets and the drying air. Initially, the evaporation occurs at the droplet surface and drying proceeds at constant rate until the dry layer starts to form at the droplet surface. Then, the drying rate decreases as the evaporation interface moves inside the droplet.

Finally, the fourth process step of spray drying includes the product separation

from the drying air and the exhaust gas cleaning before discharge using the particle collection systems, i.e. cyclone, filter bag, scrubber, etc.

2.3 Modeling of a slurry droplet drying

An in-depth understanding of the drying behavior of a single feed droplet is essential for the design of a spray dryer. The drying kinetics of droplets including solid particles inside is usually described separately for two drying periods (Elperin and Krasovitov, 1995). Water evaporates from the outer surface of the slurry droplet at constant rate as a result of heat transfer from surrounding gas by convective flow during the first period of drying. The liquid evaporation results in droplet diameter shrinking and simultaneous increase of solid concentration inside the droplet. The evaporation lead to solid commencing at the surface of the droplet and, eventually, the surface becomes covered with a layer of solid component called a ′crust′ (Charlesworth et al., 1960). This is a beginning of the second period of drying. In this period, the evaporation will take place inside the wet particle and the drying process is hindered by the addition of heat and mass transfer resistances inside the wet particle due to an increase of crust layer thickness. The second drying period continues until the particle moisture content is reduced to an equilibrium value with the drying medium. At this moment, the drying process actually stops.

The typical evolution of the droplet temperature during drying process is illustrated in Fig. 1. In this figure, the interval between points 0 and 1 corresponds to the droplet initial heating, the period between points 1 and 2 is related to the droplet evaporation period, and the interval between points 2 and 3 corresponds to the second drying period.

Parti and Palancz (1974) presented a mathematical model of single droplet/porous particle for spray drying. The model equations were developed in the general form, so the model can be applied for droplets with insoluble as well as dissolved solid. This model neglected the temperature gradient inside the droplet because of the small

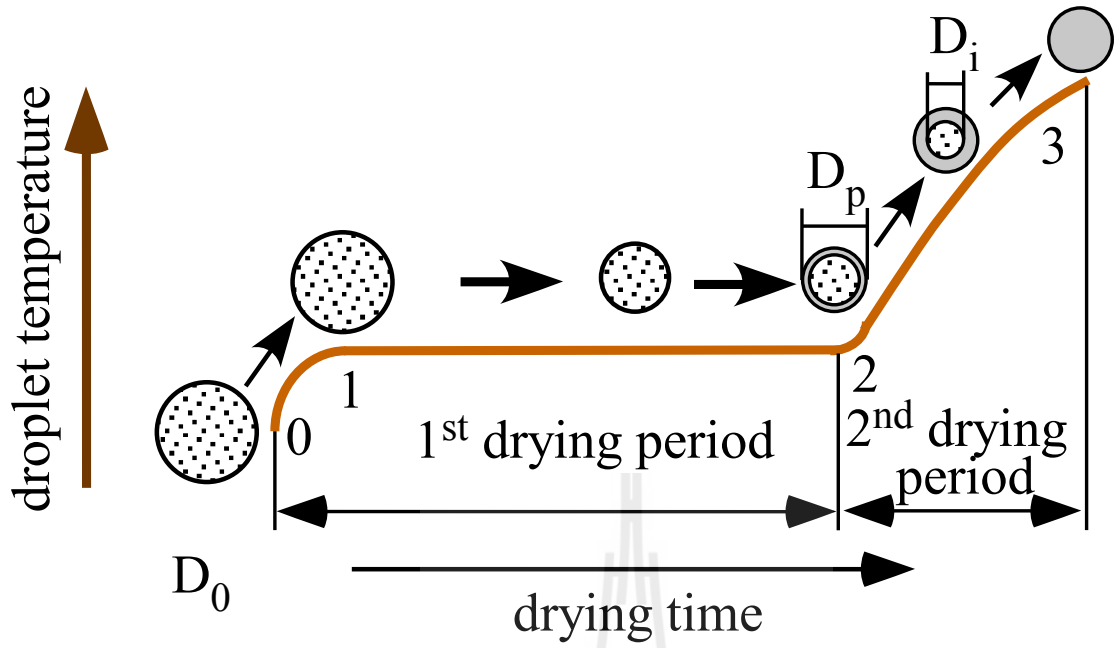

Figure 1: Typical drying behaviour of a slurry droplet. D_0: initial diameter, D_p: particle diameter, D_i: wet core diameter.

size of droplet and assumed the droplet diameter receded similar to shrinkage of a balloon. The droplet shrinks until the critical moisture content is attained, then the solid particles arrange the morphologies, the pores are formed inside the particle and its diameter remained constant. One of the major model deficiencies was the assumption of the saturated particle surface during the whole drying process, which led to incorrect prediction of the particle temperature to be constant in the falling drying rate period. Furthermore, the calculated temperature gradient between the drying air and particle surface was abnormally high.

Nesic (1990) and Nesic and Vodnik (1991) developed a theoretical drying model of a single droplet containing insoluble or dissolved solids. The temperature gradients in the droplet were neglected during the first and second periods of drying process. The moisture concentration gradient was described by the partial differential equation of Fick's diffusion. The moisture diffusion coefficient used in simulation was considered to be a function of local moisture concentration and the temperature influence was ignored. The equation of energy conservation was developed for the quasi steady-state

conditions. A good agreement of the predicted droplet temperature and mass with experimentally obtained data was observed for colloidal silica and sodium sulphate droplets, but, for the drying of skim milk, the calculated and experimental droplet temperatures demonstrated a strong discrepancy in the second period of drying.

A theoretical drying model of single droplet with insoluble/dissolved solids developed by Farid (2003) was based on an average droplet moisture content. The model comprises the temperature profile inside the droplet during the initial heating-up period. After that, the droplet temperature distribution was assumed to be uniform and equal to the wet bulb temperature of the drying air. In the second period of drying, the temperature and moisture concentration profiles inside the droplet were neglected, but a common equation of energy conservation was proposed for both crust and wet core regions of the wet particle. However, Farid (2003) unjustifiably assumed that the temperature over the crust-wet core interface was constant and equal to the wet bulb temperature during drying. Furthermore, the crust porosity was not taken into account in the heat balance boundary condition at the crust-wet core interface.

Dalmaz et al. (2007) presented a computational model of single droplet drying accounting for the droplet temperature profile in both drying periods. In their model, the authors implemented an assumption that the morphology of the droplet was fixed during both drying periods. At first, this solid frame was considered to be covered with excess of liquid. The evaporation occurred when the surface of the droplet reached to the wet bulb temperature and continued until removing the liquid excess and uncovering the solid frame, At this moment, the second drying period began and all the solid frame was divided into two regions, dry crust (dry part of the frame) and internal wet core (part of the frame still filled with liquid). Further in the second drying period, drying was assumed to occur under the crust layer by means of vapor diffusion from the wet core through the crust pores filled with air. The energy and mass balances were developed for both drying periods and the differential equation also was generated for the description of the liquid vapor diffusion through crust

pores. To validate the proposed model, simulations of droplet drying behavior were performed and the obtained results were compared to experimental data published by Nesic and Vodnik (1991). The validation demonstrated a satisfactory agreement of the predicted droplet average temperature and mass evolutions with the experimental results. However, it must be noted that the authors assumed an extreme value of the particle porosity of 0.588 in order to fit the experimental data. Consequently, agglomerates of higher porosity can be obtained using small and uniform primary particles in comparison with ones made of large particles having size distribution. Also, it is unclear how primary particles can compose the final agglomerated particle with such a great porosity.

2.4 Modeling of spray dryer

Keey (1987) and Strumillo and Kudra (1986) developed the model of spray dryer by using the overall mass and energy balances inside the drying chamber. The uniform gas conditions where assumed in the well-mixed dryer. The outlet solids moisture content was presumed to be in equilibrium with gas humidity and gas and solids outlet temperatures were almost equal. However, the well-mixed dryers models are oversimplified as they do not take into account distributions of temperature, humidity and velocity of drying medium and droplet in the drying chamber. Thus, they are not suitable for the analysis of drying mechanism of high value particles.

The two basic types of spray dryer are short-form and tall-form designs. Tall-form designs have height-to-diameter aspect ratios of greater than 5:1, giving a significant plug-flow zone inside these dryers (Keey and Pham, 1976). With short-form dryers, the complexity of the flow patterns is greater than that in tall-form dryers, in the sense that many short-form dryers have no plug-flow zone and a wide range of gas residence times. At the same time, the short-form design can be regarded as having a well-mixed gas flow pattern due to its small aspect ratio. The mass and energy balances are quite simple in this case and a well-mixed approach to modeling of spray

dryers is a simple but useful first step (Ozmen and Langrish, 2003a).

The parallel flow model for spray dryers was reported by Keey and Pham (1976) and have been used by a number of authors, including Zbicinski (1995), Truong et al. (2005), Pearce (2006) and Chiou et al. (2008). The parallel flow model is more appropriate for tall-form dryer than short-form ones, due to the overall flow pattern, as discussed above. The drying chamber was divided into the small control volumes. The equation of droplet trajectory has been included together with the equations of heat and mass balances for droplet and drying gas. But, a simple correlation was utilized to model the drying kinetics of a droplet.

Reay (1988) extended the parallel flow model by using combinations of well-mixed and parallel-flow zones, or the axial dispersion model. The first problem with such combinations is that they require accurate measurements to be performed in existing dryers using helium-injection and flow visualisation equipment. Therefore, they are unsuitable for designing new drying chambers. The second problem was that combinations of well-mixed and parallel flow zones were often not unique, with a variety of fitted combinations (well-mixed, plug-flow, bypass) being equally good representations. The third problem was that the fitted combinations were typically not generally applicable to scale up, scale down, different geometries or even changing operating conditions.

Crowe (1980) utilized the computational fluid dynamic (CFD) approach to describe the fluid flow within the spray drying chamber. The discrete approximations were used to solve the time-averaged conservation equations applying a concept known as the Particle Source-in-Cell or discrete droplet model. This concept essentially involves treating the gas as a continuous phase and the spray as a discrete tracked phase. The effects of the droplets are initially neglected when calculating the axial, radial and tangential components of the gas velocities.

Oakley et al. (1988) reported one of the first careful and complete CFD studies of flow patterns in spray dryers, finding that the values of the turbulence parameters

selected at the annular air inlet of the dryer affected the predictions of the air flow patterns significantly and that the availability of experimental measurements of these parameters is often limited. Hence either the parameters need to be obtained from a separate numerical simulation of the air inlet or they must be treated as fitting parameters (which reduces the predictive power of the model for design purposes).

The development of powerful workstations at a reasonable cost has enabled the expanded use of CFD. However, the CFD model is usually combined with the simple model of drying kinetics of the slurry droplet due to the prohibitively long calculation time.

3 Spray Drying Modeling

The drying mechanism inside the spray drying chamber is complicated by the exchange of heat, mass and momentum between the drying medium and droplets. In this chapter, the drying model of the slurry droplets inside the drying chamber was separated into two sections. In the first section, the mathematical model of drying kinetics of a slurry droplet was formulated by the condition of the humidity, velocity and the temperature of the drying medium surrounding the droplet were constant. In the second section, a droplet drying model was used together with the model of heat and mass transfer between the drying medium and droplets inside the spray drying chamber. The mathematical model of three-dimensional droplets flow in the drying medium was included in the drying model inside the chamber.

The finite difference method was utilized for solving the system of partial differential equations of heat and mass transfer inside and outside the droplet. The system of ordinary differential equations governing the droplets flow, and heat and mass transfer in the chamber was solved numerically.

3.1 Modeling of a slurry droplet drying

The numerical simulation for a slurry droplet drying model was separated into two periods by the mechanism of droplet drying, i.e. the constant rate and the falling rate periods.

3.1.1 Constant rate period

In the constant rate period, the droplet receives heat from the drying medium (air, steam, nitrogen, etc.) by the mechanism of convective heat transfer. The liquid excess in the droplet is eliminated by evaporation, resulting in droplet diameter shrinking and increasing the concentration of solid inside the droplet. Eventually, the droplet surface is covered with a crust layer of solid component. This is a beginning of the

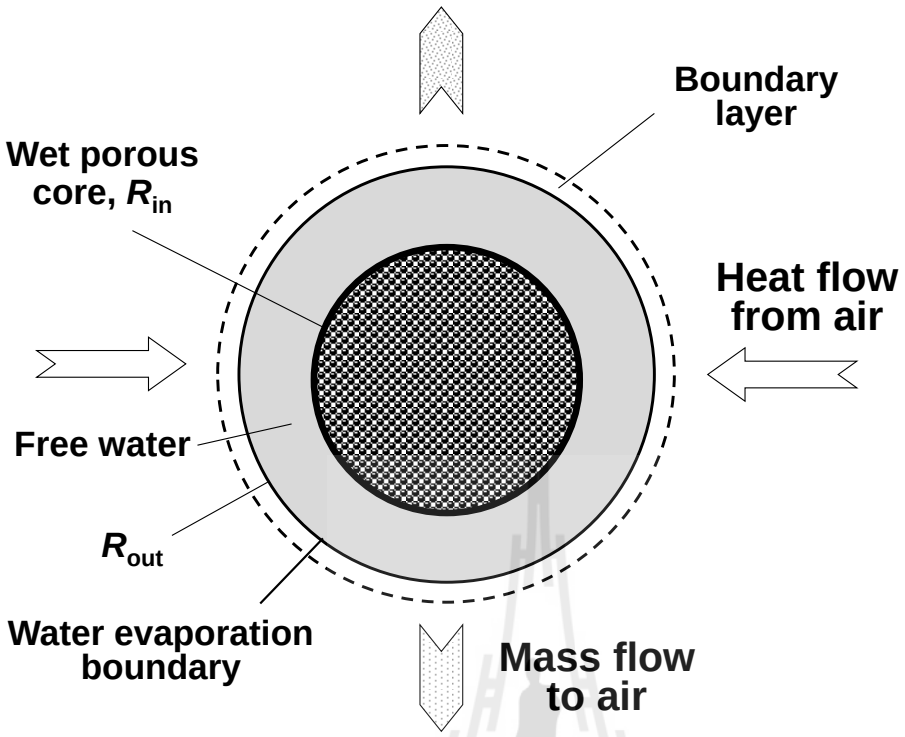

Figure 2: Droplet drying in constant rate period

falling rate period.

The following assumptions are made in the derivation of governing equations:

1. Constant drying conditions, i.e. the humidity, temperature and velocity of the drying medium surrounding the droplet remain constant during drying.

2. Droplet is spherical in shape.

3. Wet core radius of the droplet is constant.

4. Temperature varies only in the radial direction.

5. Air-liquid vapor mixture obeys the ideal gas law.

To set up the drying model in the constant rate period, the droplet is separated into two regions. The first region is a wet core, which occupies the central part of the droplet from $r = 0$ to $r = R_{in}$, and solid particles are located in this part of the

droplet. The second region from $r = R_{in}$ to $r = R_{out}$ is a free liquid, with the most liquid appear in this part.

Governing model equation of heat transfer in wet core region

The energy balance over a spherical shell of thickness Δr in the wet core region includes the following terms:

$$\begin{pmatrix} Rate\ of \\ Energy \\ in\, shell \end{pmatrix} - \begin{pmatrix} Rate\, of \\ Energy \\ out\, of\, shell \end{pmatrix} = \begin{pmatrix} Rate\, of \\ Energy \\ accumulation \end{pmatrix}$$

The energy balance could be written as

$$q_{co} \cdot 4\pi r^2\big|_r - q_{co} \cdot 4\pi r^2\big|_{r+\Delta r} = \frac{\partial}{\partial t}\left[4\pi r^2 \Delta r \cdot (\varepsilon \rho_l Cp_l T_{co} + (1-\varepsilon)\rho_s Cp_s T_{co})\right], \quad (4)$$

where q_{co} is the heat flux, T_{co} is the wet core temperature, t is time, r is the radial position in the droplet, ε is the porosity of agglomerated product, k_{co} is the heat conductivity of wet core, Cp_l and ρ_l are the heat capacity and the density of liquid,respectively, and Cp_s and ρ_s are the heat capacity and the density of solid, respectively.

Dividing by $4\pi\Delta r$ and taking the limit $\Delta r \to 0$ yields

$$-\frac{\partial}{\partial r}\left(r^2 q_{co}\right) = r^2 \left(\varepsilon \rho_l Cp_l + (1-\varepsilon)\rho_s Cp_s\right) \frac{\partial T_{co}}{\partial t}$$

Applying Fourier's law $q_{co} = -k_{co}\dfrac{\partial T_{co}}{\partial r}$ results in

$$-\frac{\partial}{\partial r}\left(-r^2 k_{co}\frac{\partial T_{co}}{\partial r}\right) = r^2 \left(\varepsilon \rho_l Cp_l + (1-\varepsilon)\rho_s Cp_s\right) \frac{\partial T_{co}}{\partial t} \quad (5)$$

Rearranging Eq. (5) gives

$$\frac{1}{r^2}\frac{\partial}{\partial r}\left(r^2\frac{\partial T_{co}}{\partial r}\right) = \frac{(\varepsilon\rho_l Cp_l + (1-\varepsilon)\rho_s Cp_s)}{k_{co}}\frac{\partial T_{co}}{\partial t} \tag{6}$$

Defining the coefficient α_1 as

$$\alpha_1 = \frac{(\varepsilon\rho_l Cp_l + (1-\varepsilon)\rho_s Cp_s)}{k_{co}}, \tag{7}$$

Eq. (6) becomes

$$\frac{1}{r^2}\frac{\partial}{\partial r}\left(r^2\frac{\partial T_{co}}{\partial r}\right) = \alpha_1\frac{\partial T_{co}}{\partial t} \tag{8}$$

Using the product rule of differentiation, Eq. (8) can be rewritten as

$$\alpha_1\frac{\partial T_{co}}{\partial t} = \frac{1}{r^2}\left(r^2\frac{\partial^2 T_{co}}{\partial r^2} + 2r\frac{\partial T_{co}}{\partial r}\right) \tag{9}$$

Finally, the temperature distribution in the wet core is described by the following partial differential equation

$$\alpha_1\frac{\partial T_{co}}{\partial t} = \frac{\partial^2 T_{co}}{\partial r^2} + \frac{2}{r}\frac{\partial T_{co}}{\partial r} \tag{10}$$

Making the spatial variable r dimensionless results in

$$\alpha_1'\frac{\partial T_{co}}{\partial t} = \frac{\partial^2 T_{co}}{\partial \xi^2} + \frac{2}{\xi}\frac{\partial T_{co}}{\partial \xi}, \tag{11}$$

where ξ is the dimensionless distance in constant rate period defined as $\xi = r/R_{init}$ and R_{init} is the initial radius of the droplet. The coefficient α_1' is defined as

$$\alpha_1' = \frac{R_{init}^2\,(\varepsilon\rho_l Cp_l + (1-\varepsilon)\rho_s Cp_s)}{k_{co}} \tag{12}$$

An initial condition and two boundary conditions are required to solve Eq. (11).

- **Initial condition**

The temperature of a wet core region at $t = 0$ is assumed to be equal to an initial temperature of the droplet.

$$T_{co}(t = 0) = T_{init}, \tag{13}$$

where T_{init} is the initial temperature of the droplet.

- **Boundary equation at the center of droplet**

There is no temperature gradient at the particle center because of the symmetrical temperature distribution. Hence,

$$\left.\frac{\partial T_{co}}{\partial r}\right|_{r=0} = 0 \quad \text{or} \quad \left.\frac{\partial T_{co}}{\partial \xi}\right|_{\xi=0} = 0 \tag{14}$$

- **Boundary condition on the outer surface of wet core**

The temperature profile is assumed to be continuous at the boundary of wet core and free liquid regions. Hence,

$$T_{co}|_{r=R_{in}} = T_l|_{r=R_{in}} \quad \text{or} \quad T_{co}|_{\xi=\xi_{in}} = T_l|_{\xi=\xi_{in}}\,, \tag{15}$$

where T_l is the free liquid temperature.

Governing model equation of heat transfer in free liquid region

The energy balance over a spherical shell in the free water region is

$$\begin{pmatrix} Rate\ of \\ Energy \\ in\ shell \end{pmatrix} - \begin{pmatrix} Rate\ of \\ Energy \\ out\ of\ shell \end{pmatrix} = \begin{pmatrix} Rate\ of \\ Energy \\ accumulation \end{pmatrix}$$

$$q_l \cdot 4\pi r^2\big|_r - q_l \cdot 4\pi r^2\big|_{r+\Delta r} = \frac{\partial}{\partial t}\left(4\pi r^2 \cdot \Delta r \rho_l C p_l T_l\right) \tag{16}$$

Dividing by $4\pi\Delta r$ and taking the limit $\Delta r \to 0$ yields

$$-\frac{\partial}{\partial r}\left(r^2 q_l\right) = r^2 \rho_l C p_l \frac{\partial T_l}{\partial t} \tag{17}$$

Applying Fourier's law $q_l = -k_l \frac{\partial T_l}{\partial r}$, Eq. (17) can be rewritten as

$$-\frac{\partial}{\partial r}\left(-r^2 k_l \frac{\partial T_l}{\partial r}\right) = r^2 \rho_l C p_l \frac{\partial T_l}{\partial t}, \tag{18}$$

where k_l is the thermal conductivity of liquid phase.

Simplifying Eq. (18)

$$\frac{1}{r^2}\frac{\partial}{\partial r}\left(r^2 \frac{\partial T_l}{\partial r}\right) = \frac{\rho_l C p_l}{k_l}\frac{\partial T_l}{\partial t} \tag{19}$$

and introducing the coefficient α_2

$$\alpha_2 = \frac{\rho_l C p_l}{k_l} \tag{20}$$

results in

$$\frac{1}{r^2}\frac{\partial}{\partial r}\left(r^2 \frac{\partial T_l}{\partial r}\right) = \alpha_2 \frac{\partial T_l}{\partial t} \tag{21}$$

Using the product rule of differentiation, Eq. (21) is transformed as

$$\alpha_2 \frac{\partial T_l}{\partial t} = \frac{\partial^2 T_l}{\partial r^2} + \frac{2}{r}\frac{\partial T_l}{\partial r} \tag{22}$$

The temperature distribution in the free liquid region can be obtained as

$$-\frac{\partial}{\partial r}\left(-r^2 k_l \frac{\partial T_l}{\partial r}\right) = r^2 \rho_l C p_l \frac{\partial T_l}{\partial t} \tag{23}$$

Using the dimensionless distance ξ, Eq. (23) is rearranged as

$$\alpha_2' \frac{\partial T_l}{\partial t} = \frac{\partial^2 T_l}{\partial \xi^2} + \frac{2}{\xi}\frac{\partial T_l}{\partial \xi}, \tag{24}$$

where

$$\alpha_2' = \frac{R_{init}^2 \rho_l C p_l}{k_l} \tag{25}$$

The initial condition and two boundary conditions for Eq. (24) are

- **Initial condition**

The temperature of free liquid region is equal to the initial droplet temperature at the beginning of the drying process

$$T_l(t = 0) = T_{init} \tag{26}$$

- **Boundary condition on the inner surface of free liquid region**

Assuming the continuity of the heat flux across the boundary of free liquid and wet core regions, the following equation is obtained.

$$q_l|_{r=R_{in}} = q_{co}|_{r=R_{in}} \quad \text{or} \quad q_l|_{\xi=\xi_{in}} = q_{co}|_{\xi=\xi_{in}} \tag{27}$$

Applying Fourier's law to both sides of Eq. (27) results in

$$-k_l \frac{\partial T_l}{\partial r}\bigg|_{r=R_{in}} = -k_{co} \frac{\partial T_{co}}{\partial r}\bigg|_{r=R_{in}} \tag{28}$$

and rearranging Eq. (28) in dimensionless form gives

$$-k_l \frac{\partial T_l}{\partial \xi}\bigg|_{\xi=\xi_{in}} = -k_{co} \frac{\partial T_{co}}{\partial \xi}\bigg|_{\xi=\xi_{in}} \tag{29}$$

- **Boundary condition on the outer surface of droplet**

The heat from the drying medium is supplied to the outer droplet surface by convection. At the same time, heat is transferred from the surface to the center of the droplet by conduction mechanism. After receiving heat from the drying medium, the droplet heats up to the wet bulb temperature and starts to evaporate. Thus, both mechanisms at the droplet surface are occurred, gaining and loosing heat, at the

same time. Assuming that there is no accumulation of heat on the droplet surface, the steady state heat balance is

$$\begin{pmatrix} Rate\ of \\ Energy \\ in\ shell \end{pmatrix} - \begin{pmatrix} Rate\ of \\ Energy \\ out\ of\ shell \end{pmatrix} + \begin{pmatrix} Rate\ of \\ Energy \\ generated \end{pmatrix} = 0$$

$$k_h \left(T_l - T_{gas}\right) \cdot 4\pi r^2\big|_{r=R_{out}} - q_l \cdot 4\pi r^2\big|_{r=R_{out}} - \rho_l \lambda_l \frac{dV}{dt}\bigg|_{r=R_{out}} = 0, \tag{30}$$

where T_{gas} is the drying medium temperature, k_h is the convective heat transfer coefficient, λ_l is the latent heat of evaporation and V is the droplet volume, $V = \frac{4}{3}\pi r^3$.

Using the chain rule of differentiation, Eq. (30) is rearranged as

$$\begin{aligned} k_h \left(T_l - T_{gas}\right) \cdot 4\pi r^2\big|_{r=R_{out}} - q_l \cdot 4\pi r^2\big|_{r=R_{out}} &= \rho_l \lambda_l \frac{4}{3}\pi \frac{dr^3}{dr}\frac{dr}{dt}\bigg|_{r=R_{out}} \\ &= \rho_l \lambda_l \frac{4}{3}\pi \left(3r^2\right) \frac{dr}{dt}\bigg|_{r=R_{out}} \end{aligned} \tag{31}$$

Dividing by $4\pi r^2$ and applying Fourier's law $q_l = -k_l \dfrac{\partial T_l}{\partial r}$ results in

$$k_l \frac{\partial T_l}{\partial r}\bigg|_{r=R_{out}} + k_h \left(T_l - T_{gas}\right) = \rho_l \lambda_l \frac{dR_{out}}{dt} \tag{32}$$

Using coefficients α_3 and α_4,

$$\alpha_3 = \frac{k_h}{\rho_l} \quad \text{and} \quad \alpha_4 = \frac{k_l}{\rho_l}, \tag{33}$$

Eq. (32) becomes

$$\lambda_l \frac{dR_{out}}{dt} = \alpha_3 \left(T_l - T_{gas}\right) + \alpha_4 \frac{\partial T_l}{\partial r}\bigg|_{r=R_{out}} \tag{34}$$

Rearranging Eq. (32) and making the radial position dimensionless gives

$$\lambda_l \frac{d\xi_{out}}{dt}\bigg|_{\xi=\xi_{out}} = \alpha_3' \left(T_l - T_{gas}\right) + \alpha_4' \frac{\partial T_l}{\partial \xi}\bigg|_{\xi=\xi_{out}}, \tag{35}$$

where

$$\alpha_3' = \frac{k_h}{R_{init}\rho_l} \quad \text{and} \quad \alpha_4' = \frac{k_l}{R_{init}^2\rho_l} \tag{36}$$

The steady state mass balance on the outer droplet surface is

$$-N_A \cdot 4\pi r^2\big|_{r=R_{out}} - \frac{\rho_l}{M_l}\frac{dV}{dt}\bigg|_{r=R_{out}} = 0 \tag{37}$$

The mass flux is defined as

$$N_A = k_m \left(C_{lv} - C_{gas}\right), \tag{38}$$

where k_m is the convective mass transfer coefficient, C_{lv} is the liquid vapor concentration, C_{gas} is the bulk concentration and M_l is the molecular weight of liquid.

Using the chain rule of differentiation and dividing by $4\pi r^2$ yields

$$-k_m \left(C_{lv} - C_{gas}\right) = \frac{\rho_l}{M_l}\frac{dR_{out}}{dt} \tag{39}$$

Rearranging Eq. (39) results in

$$\frac{dR_{out}}{dt} = -\frac{k_m M_l}{\rho_l}\left(C_{lv} - C_{gas}\right) \tag{40}$$

Introducing the coefficient α_5,

$$\alpha_5 = \frac{k_m M_l}{\rho_l}, \tag{41}$$

Eq. (40) can be rewritten as

$$\frac{dR_{out}}{dt} = -\alpha_5 \left(C_{lv} - C_{gas}\right) \tag{42}$$

The dimensionless form of Eq. (42) is

$$\frac{d\xi_{out}}{dt} = -\alpha_5' \left(C_{lv} - C_{gas}\right), \tag{43}$$

where

$$\alpha_5' = \frac{k_m M_l}{R_{init}\rho_l} \tag{44}$$

To solve the differential equation Eq. (43), an initial condition is needed as

$$\xi_{out}(t = 0) = 1 \tag{45}$$

3.1.2 Falling rate period

In the falling rate period, the evaporation will take place inside the agglomerated particle and the drying process is hindered by addition of heat and mass transfer resistances inside the particle due to increasing crust thickness. The second drying period proceeds until the particle moisture content is reduced to an equilibrium value with the drying medium. At this moment, the drying process actually stops and then particle will be heated up to the final temperature.

The following assumptions are made in derivation of the governing equations:

1. Constant drying conditions, i.e. the humidity, temperature and velocity of the drying medium surrounding the particle remain constant during drying.

2. Particle is spherical in shape.

3. Radius of the particle R_{in} does not change during drying.

4. The morphology of the particle does not change during drying.

5. Temperature and liquid vapor concentration vary only in the radial direction.

6. Pore of the dry crust region are filled by air, which is stagnant, and liquid vapor diffuses through these pores.

7. Fick's law of diffusion with an effective diffusion coefficient describes diffusion of liquid vapor through the pores of the dry crust.

8. Air-liquid vapor mixture obeys the ideal gas law.

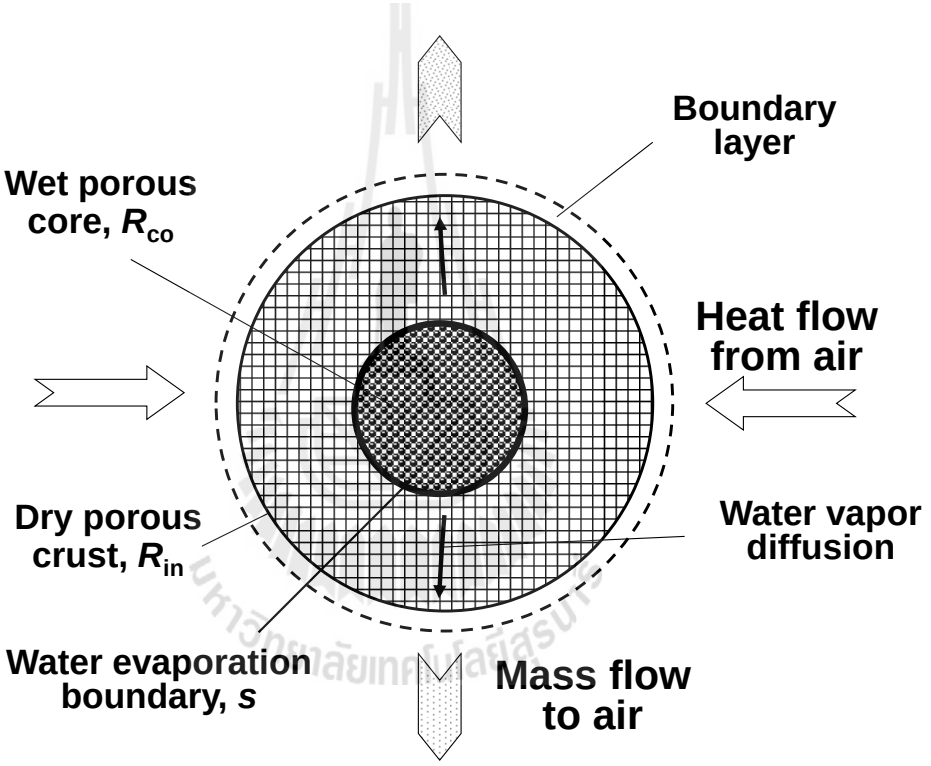

Figure 3: Particle drying in falling rate period.

The particle in the falling rate period is separated into two regions: a wet core from $r = 0$ to $r = s$ and a dry crust from $r = s$ to $r = R_{in}$.

Governing model equation of heat transfer in wet core region

The energy balance over the shell of wet core region is derived similar to Eq. (5) as

$$-\frac{\partial}{\partial r}\left(-r^2 k_{co}\frac{\partial T_{co}}{\partial r}\right) = r^2\left(\varepsilon\rho_l Cp_l + (1-\varepsilon)\rho_s Cp_s\right)\frac{\partial T_{co}}{\partial t} \tag{46}$$

Rearranging Eq. (46) and making the radial position dimensionless results in

$$\beta_1' \frac{\partial T_{co}}{\partial t} = \frac{\partial^2 T_{co}}{\partial \zeta^2} + \frac{2}{\zeta} \frac{\partial T_{co}}{\partial \zeta} \tag{47}$$

where ζ is the dimensionless distance in the falling rate period defined as $\zeta = r/R_{in}$ and β' is the coefficient,

$$\beta_1' = \frac{R_{in}^2 \left(\varepsilon \rho_l C p_l + (1-\varepsilon)\rho_s C p_s\right)}{k_{co}} \tag{48}$$

An initial condition and two boundary conditions are required to solve Eq. (47).

- **Initial condition**

The falling rate period initiates when the free liquid is depleted and the crust layer is just started to form. Thus, the wet core region occupies almost all droplet volume. Hence, the initial temperature of the wet core in the falling rate period is equal to the final core temperature in the constant rate period.

$$T_{co}(t=0) = T_{f,init}\,, \tag{49}$$

where $T_{f,init}$ is the final temperature of the wet core in the constant rate period.

- **Boundary equation at the center of particle**

$$\left.\frac{\partial T_{co}}{\partial r}\right|_{r=0} = 0 \quad \text{or} \quad \left.\frac{\partial T_{co}}{\partial \zeta}\right|_{\zeta=0} = 0 \tag{50}$$

- **Boundary condition at the evaporation interface**

The temperature profile is assumed to be continuous at the boundary of wet core and dry crust regions. Hence,

$$T_{co}|_{r=s} = T_{cr}|_{r=s} \quad \text{or} \quad T_{co}|_{\zeta=s'} = T_{cr}|_{\zeta=s'}\,, \tag{51}$$

where T_{cr} is the dry crust temperature and s' is the dimensionless radius of wet core

defined as $s' = s/R_{in}$.

Governing model equations of heat and mass transfer in dry crust region

The model equation of heat transfer in the dry crust region is

$$\frac{\partial}{\partial t}\left[(1-\varepsilon)\,\rho_s C p_s T_{cr}\right] = \frac{1}{r^2}\frac{\partial}{\partial r}\left(r^2 k_{cr}\frac{\partial T_{cr}}{\partial r}\right), \tag{52}$$

where k_{cr} is the thermal conductivity of dry crust.

Rearranging Eq. (52)

$$\frac{(1-\varepsilon)\rho_s C p_s}{k_{cr}}\frac{\partial T_{cr}}{\partial t} = \frac{1}{r^2}\frac{\partial}{\partial r}\left(r^2\frac{\partial T_{cr}}{\partial r}\right) \tag{53}$$

and introducing the constant β_2,

$$\beta_2 = \frac{(1-\varepsilon)\,\rho_s C p_s}{k_{cr}}, \tag{54}$$

results in

$$\beta_2\frac{\partial T_{cr}}{\partial t} = \frac{1}{r^2}\frac{\partial}{\partial r}\left(r^2 k_{cr}\frac{\partial T_{cr}}{\partial r}\right) \tag{55}$$

Using the dimensionless distance ζ, Eq. (55) is rearranged as

$$\beta_2'\frac{\partial T_{cr}}{\partial t} = \frac{\partial^2 T_{cr}}{\partial \zeta^2} + \frac{2}{\zeta}\frac{\partial T_{cr}}{\partial \zeta}, \tag{56}$$

where

$$\beta_2' = \frac{R_{in}^2(1-\varepsilon)\,\rho_s C p_s}{k_{cr}}, \tag{57}$$

An initial and two boundary conditions are given at the evaporation interface and on the outer surface of the droplet:

- **Initial condition**

It is assumed that the dry crust region appears immediately after the falling rate period starts. Therefore, the initial temperature of the dry crust is equal to the final

temperature of the constant rate period.

$$T_{cr}(t=0) = T_{f,init} \tag{58}$$

- **Boundary equation at the evaporation interface**

The heat balance at the evaporation interface is derived as

$$\varepsilon\rho_l\lambda_l\frac{ds}{dt} = -\,k_{cr}\frac{\partial T_{cr}}{\partial r}\bigg|_{r=s} + k_{co}\frac{\partial T_{co}}{\partial r}\bigg|_{r=s} \tag{59}$$

The left hand side of Eq. (59) corresponds to the amount of heat consumed for liquid evaporation. The first term on the right hand side describes the heat supply to the interface by conduction across the crust layer and the second one characterizes the heat flow from interface to particle center by conduction through the wet core region.

Rearranging Eq. (59) and making the radial position dimensionless gives

$$\lambda_l\frac{ds'}{dt} = -\,\beta_4'\frac{\partial T_{cr}}{\partial \zeta}\bigg|_{\zeta=s'} + \beta_5'\frac{\partial T_{co}}{\partial \zeta}\bigg|_{\zeta=s'}, \tag{60}$$

where

$$\beta_4' = \frac{k_{cr}}{R_{in}^2\varepsilon\rho_l} \tag{61}$$

and

$$\beta_5' = \frac{k_{co}}{R_{in}^2\varepsilon\rho_l} \tag{62}$$

The mass balance of liquid vapor at the evaporation interface is

$$\frac{ds'}{dt} = \beta_7'\frac{\partial C_{lv}}{\partial \zeta}\bigg|_{\zeta=s'}, \tag{63}$$

where

$$\beta_7' = \frac{D_{cr}M_l}{R_{in}^2\varepsilon\rho_l} \tag{64}$$

An initial condition is required to solve Eq. (63).

$$s'(t=0) = 1 \tag{65}$$

- **Boundary condition at the outer surface of droplet**

Assuming that there is no heat accumulation at the outer droplet surface, all heat supplied to this surface by convection is transferred toward the droplet center by conduction through the crust layer. The heat balance at the outer surface of the droplet is described as

$$-k_{cr}\frac{\partial T_{cr}}{\partial r}\bigg|_{r=R_{in}} = k_h\left(T_{cr}(r=R_{in}) - T_{gas}\right) \tag{66}$$

Using the dimensionless radial position ζ, Eg. (66) can be rewritten as

$$-k_{cr}\frac{\partial T_{cr}}{\partial \zeta}\bigg|_{\zeta=1} = R_{in}k_h\left(T_{cr}(\zeta=1) - T_{gas}\right) \tag{67}$$

The liquid vapor generated at the evaporation interface is transported to the droplet surface by the driving force arising from the concentration gradient between the evaporation interface and the outer droplet surface. The mass transfer of liquid vapor through the dry crust is described as

$$\varepsilon\frac{\partial C_{lv}}{\partial t} = \frac{D_{cr}}{r^2}\frac{\partial}{\partial r}\left(r^2\frac{\partial C_{lv}}{\partial r}\right), \tag{68}$$

where C_{lv} is the concentration of liquid vapor, Cp_{lv} is the heat capacity of liquid vapor, D_{cr} is the effective diffusivity of dry crust and M_l is the molecular weight of liquid.

Rearranging Eq. (68) and using dimensionless radial position gives

$$\beta_6'\frac{\partial C_{lv}}{\partial t} = \frac{\partial^2 C_{lv}}{\partial \zeta^2} + \frac{2}{\zeta}\frac{\partial C_{lv}}{\partial \zeta} \tag{69}$$

where

$$\beta_6' = \frac{R_{in}^2 \varepsilon}{D_{cr}} \tag{70}$$

An initial and two boundary conditions for Eq. (69) are:

- **Initial condition**

The vapor concentration at $t = 0$ is calculated using the ideal gas law at temperature equal to $T_{f,init}$

$$C_{lv}(t = 0) = \frac{P^{vap}\left(T_{f,init}\right)}{R_{gas} T_{f,init}} \tag{71}$$

- **Boundary equation at the evaporation interface**

At $r = s(t)$ or $\zeta = s'(t)$, the vapor concentration is also described by the ideal gas law as

$$C_{lv}(r = s(t)) = \frac{P^{vap}\left(T_{cr}|_{r=s(t)}\right)}{R_{gas} T_{cr}|_{r=s(t)}} \quad \text{or} \quad C_{lv}(\zeta = s'(t)) = \frac{P^{vap}\left(T_{cr}|_{\zeta=s'(t)}\right)}{R_{gas} T_{cr}|_{\zeta=s'(t)}} \tag{72}$$

- **Boundary condition at outer surface of droplet**

The mass balance of vapor at the outer droplet surface is given as

$$-D_{cr} \left.\frac{\partial C_{lv}}{\partial r}\right|_{r=R_{in}} = k_m \left(C_{lv}(r = R_{in}) - C_{gas}\right), \tag{73}$$

where k_m is the convective mass transfer coefficient.

Using the dimensionless radial position ζ, Eq. (73) is rearranged as

$$-D_{cr} \left.\frac{\partial C_{lv}}{\partial \zeta}\right|_{\zeta=1} = R_{in} k_m \left(C_{lv}(\zeta = 1) - C_{gas}\right) \tag{74}$$

3.2 Modeling of drying in spray dryer chamber

The drying mechanism of slurry droplets in a spray drying chamber is considered in this section. The humidity and temperature of drying medium surrounding the droplets change along the drying chamber height due to the heat and mass transfer

between droplets and medium.

The drying medium model is formulated taking into account the heat, mass and momentum exchange between droplets and the drying medium in the chamber. The model of a slurry droplet drying developed in the first section is combined with the drying medium model to study the drying kinetics and the mechanism of droplets drying in the spray drying chamber. The equations of droplet trajectory gives the droplet velocity distribution in the drying chamber, and the heat and mass balances around the shell in the chamber yield the distributions of humidity and temperature of drying medium along the chamber height.

3.2.1 Droplet formation by atomization

In this work, a centrifugal-pressure nozzle and a rotary atomizer are adopted in simulation to represent two types of atomizers frequently used in industry. The trajectory of droplets in a spray dryer depends on the type of atomizer. The initial velocity of droplets generated from liquid feed by atomizer are calculated according to Master (1985).

Centrifugal-Pressure Nozzle

A spray of droplets is created by forcing the slurry feed under pressure through an orifice. The slurry feed is usually supplied in such a way that it forms a patterns of swirling motion in the centrifugal- or swirling-pressure nozzle, as shown in Fig. 4. Droplets leaving the nozzle spread radially outward forming a hollow cone spray and we can assume that they have two predominant velocity components, axial (U_{px}) and tangential velocities (U_{pt}).

The axial droplet velocity as a function of slurry feed rate can be calculated as

$$U_{px} = \frac{w_{sl}}{2\pi\rho_{sl} r_{\mathrm{o}} b}, \tag{75}$$

where r_{o} is the orifice radius, w_{sl} is the mass flow rate of slurry, ρ_{sl} is the slurry density

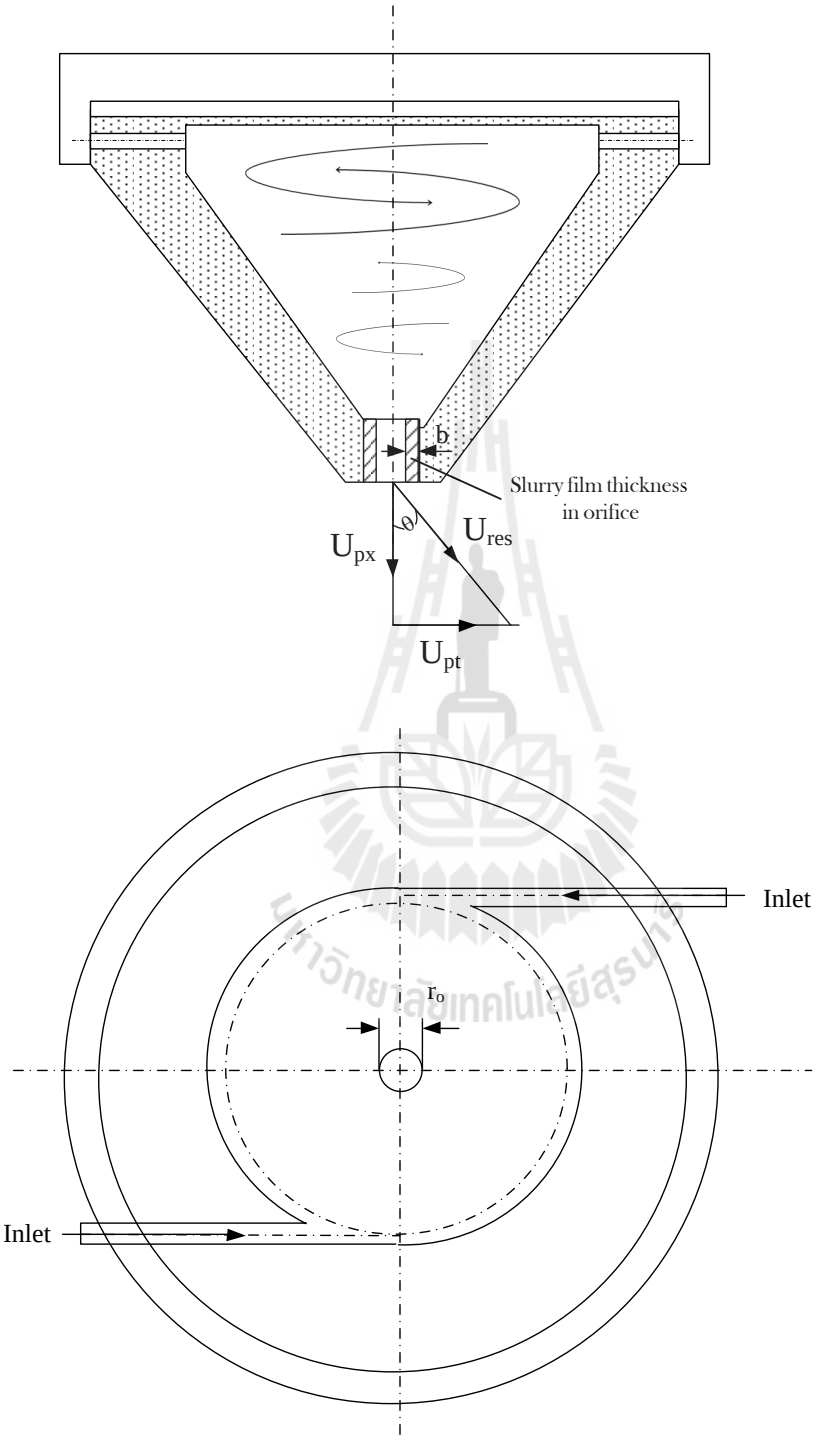

Figure 4: Illustration of centrifugal-pressure nozzle.

and b is the thickness of the liquid film at the orifice.

In general, the orifice does not run full of slurry and the air core within the orifice occupies a space ranging from 0.4 to 0.8 of the orifice diameter. Thus, the liquid film thickness at the orifice will be known if the air core and orifice diameters are specified.

The slurry density is defined as

$$\rho_{sl} = \frac{\rho_s \rho_l}{\rho_l \left(1 - X_{sl}\right) + X_{sl} \rho_s} \tag{76}$$

where X_{sl} is the moisture content of slurry.

Taking into account the nozzle geometry, it can be assumed that the droplet leaving atomizer travels in a straight line at an angle θ to atomizer tip. Therefore, the half spray angle is defined as

$$\theta = \tan^{-1}\left(\frac{U_{pt}}{U_{px}}\right), \tag{77}$$

where θ is a half spray angle.

Consequently, the tangential velocity is expressed as

$$U_{pt} = U_{px} \tan\theta \tag{78}$$

Rotary Nozzle

The formation of droplets from the slurry feed is taking place during rotary atomization since the centrifugal energy of the feed stream generated by the rotating disk results in the high relative velocity between air and slurry, as shown in Fig. 5.

Droplets discharging from the edge of the disk have two predominant velocity components, radial (U_{pr})and tangential velocities (U_{pt}). The radial velocity of droplets generated by wheel atomizer can be determined as

$$U_{pr} = 0.0024\left(\frac{\rho_{sl}\pi^2 N^2 d Q^2}{\mu h_r^2 n^2}\right)^{1/3} \tag{79}$$

where d is the diameter of wheel, Q is the slurry volumetric feed rate, N is the speed

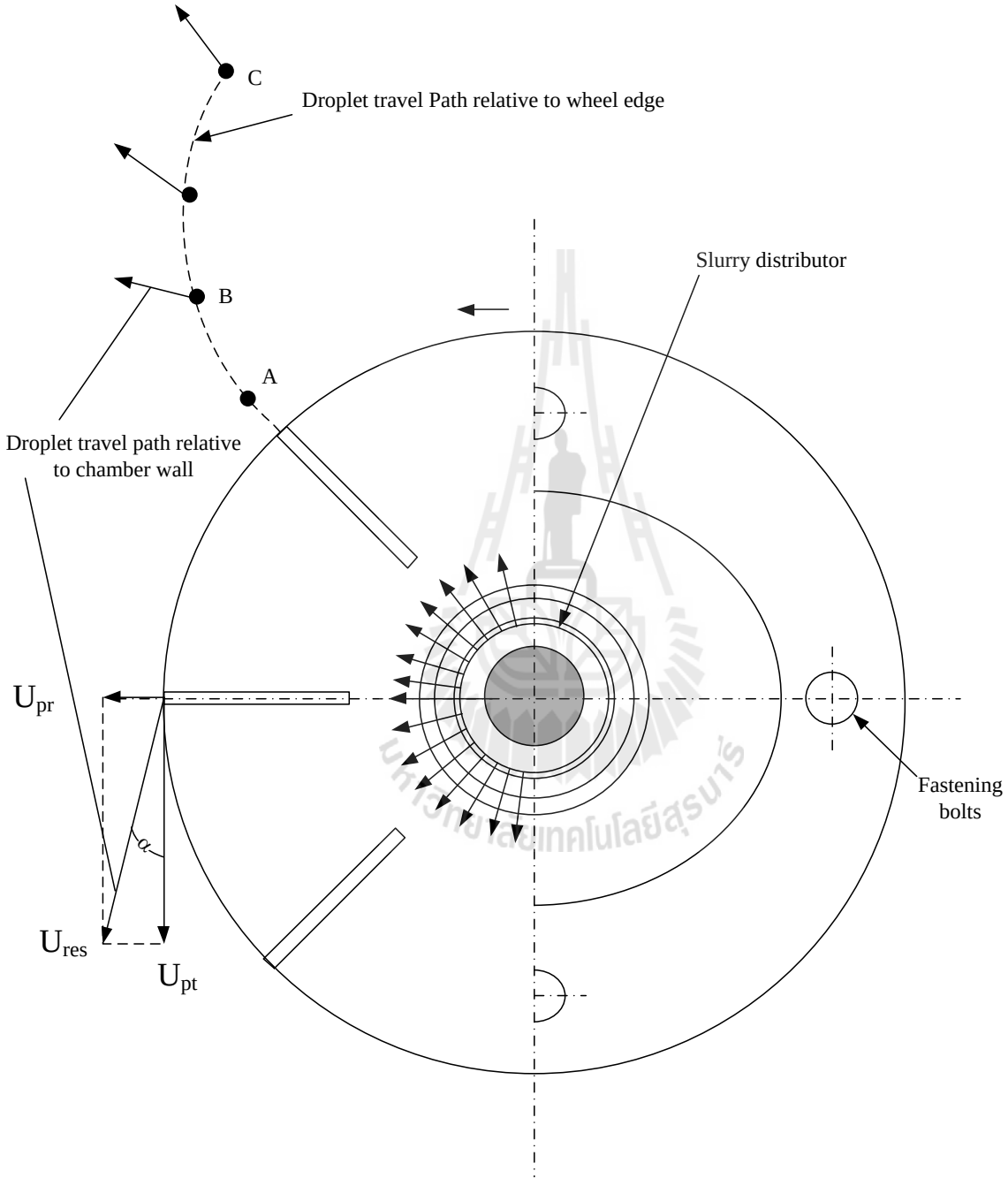

Figure 5: Illustration of rotary nozzle.

of rotation in r.p.m, μ is the viscosity of slurry in cP, n is the number of vanes or hole and h_r is the height of vanes or hole.

The tangential velocity can be calculated as

$$U_{pt} = \pi dN \tag{80}$$

3.2.2 Droplet trajectories in spray dryer

Atomizers of different types generate diverse flow patterns of droplets inside the spray drying chamber resulting in distinct droplet velocity profiles that affects the drying kinetics of droplets.

In this work, the droplets are assumed to be generated by the rotary atomizer and the air flow pattern is presumed to be flat in the radial direction of the drying chamber. The governing equations of the trajectory of droplets are derived below. Figure 6 illustrates the derivation.

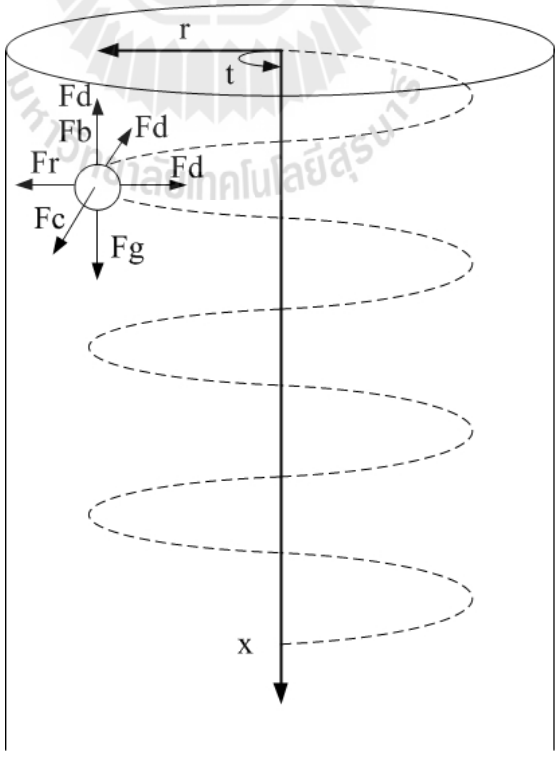

Figure 6: Trajectory of the droplet in the drying chamber.

From Newton's second law

$$m_p a = F, \tag{81}$$

where m_p is the mass of a droplet (particle), a is the droplet acceleration and F is the force acting on a droplet.

In the case of more than one force

$$m_p \frac{dU_{pi}}{d\tau} = \sum \text{Forces acting on an droplet}, \tag{82}$$

where U_{pi} is the droplet velocity in i-direction, τ is the droplet residence time, $\tau = h/U_{px}$, and h is the height of the drying chamber. Thus, summation of forces acting on the droplet are given as:

- in the x-direction

$$m_p \frac{dU_{px}}{d\tau} = F_g - F_b - F_d, \tag{83}$$

where F_g is the acceleration force, $F_g = m_p g$, F_b is the buoyant force, $F_b = \frac{m_p \rho_a g}{\rho_p}$, and F_d is the drag force, $F_d = \frac{C_D \rho_a A_p U_p^2}{2}$. Here, ρ_g is the gas density, ρ_p is the droplet density, g is the gravitational acceleration, C_D is the drag force coefficient and U_p is the relative droplet velocity.

- in the r-direction

$$m_p \frac{dU_{pr}}{d\tau} = F_r - F_d, \tag{84}$$

where F_r is the centrifugal force, $F_r = \frac{m_p U_{pt}^2}{r}$.

- in the τ-direction

$$m_p \frac{dU_{pt}}{d\tau} = -F_c - F_d, \tag{85}$$

where F_c is the Coriolis force, $F_c = \frac{m_p U_{pr} U_{pt}}{r}$.

Substitution of equations for forces into Eqs (83) - (85) yields

$$m_p \frac{dU_{px}}{d\tau} = m_p g - \frac{m_p \rho_a g}{\rho_p} - \frac{C_D \rho_a A_p U_p^2}{2} \tag{86}$$

$$m_p \frac{dU_{pr}}{d\tau} = \frac{m_p U_{pt}^2}{r} - \frac{C_D \rho_a A_p U_p^2}{2} \tag{87}$$

$$m_p \frac{dU_{pt}}{d\tau} = -\frac{m_p U_{pr} U_{pt}}{r} - \frac{C_D \rho_a A_p U_p^2}{2} \tag{88}$$

In case of a spherical droplet, the projected area is $A_p = \frac{\pi}{4} {d_p}^2$ and the mass is $m_p = \frac{\rho_p \pi d_p^3}{6}$. The relative droplet velocity is expressed as $U_p^2 = U_p \left(U_{pi} - U_{gi}\right)$, where U_{gi} is the gas velocity in i direction.

The final equations after rearranging Eqs. (83),(84) and(85) are given as

$$\frac{dU_{px}}{dh} = \left[\left(1 - \frac{\rho_g}{\rho_p}\right) g - \frac{3}{4} \frac{\rho_g C_D U_p \left(U_{px} - U_{gx}\right)}{\rho_p d_p}\right] \frac{1}{U_{px}} \tag{89}$$

$$\frac{dU_{pr}}{dh} = \left[\frac{U_{pt}^2}{r_c} - \frac{3}{4} \frac{\rho_g C_D U_p \left(U_{pr} - U_{gr}\right)}{\rho_p d_p}\right] \frac{1}{U_{px}} \tag{90}$$

$$\frac{dU_{pt}}{dh} = \left[-\frac{U_{pr} U_{pt}}{r_c} - \frac{3}{4} \frac{\rho_g C_D U_p \left(U_{pt} - U_{gt}\right)}{\rho_p d_p}\right] \frac{1}{U_{px}}, \tag{91}$$

where r_c is the radial position of droplets in the drying chamber.

The relative droplet velocity can be calculated as

$$U_p = \left[\left(U_{px} - U_{gx}\right)^2 + \left(U_{pr} - U_{gr}\right)^2 + \left(U_{pt} - U_{gt}\right)^2\right]^{1/2} \tag{92}$$

The radial location of droplets is determined from the following equation

$$\frac{dr_c}{dh} = \frac{U_{pr}}{U_{px}} \tag{93}$$

The following empirical equation was used to evaluate the drag force coefficient

(Holterman, 2003)

$$C_D = \left(\left(\frac{a}{Re}\right)^c + b^c\right)^{1/c}, \tag{94}$$

with constants $a = 24, b = 0.32$ and $c = 0.52$.

3.2.3 Mass balance of drying medium

Figure 7 illustrates the derivation of heat and mass balances in the drying chamber.

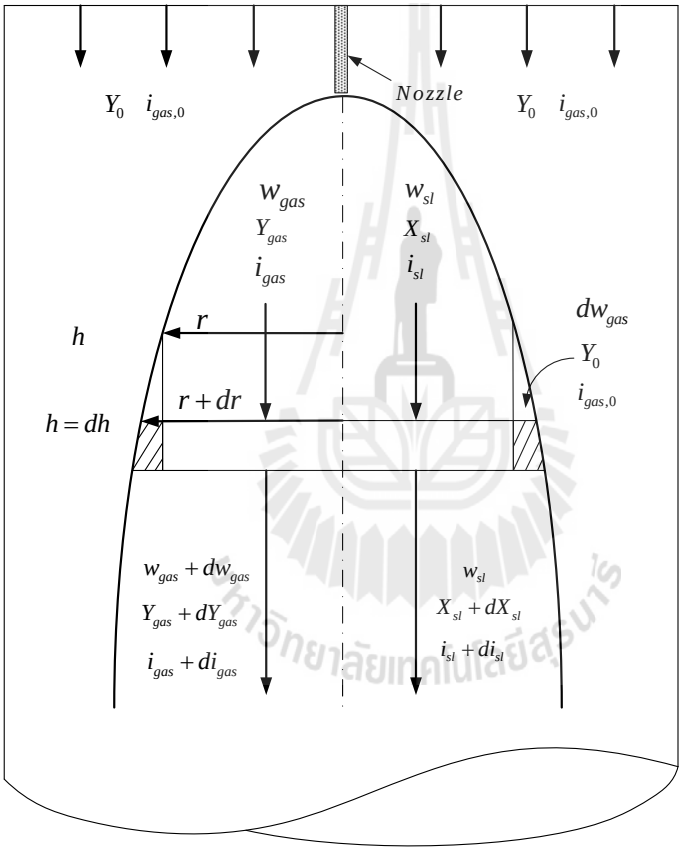

Figure 7: Illustration of heat and mass transfer balances in drying chamber.

The mass balance over the shell in the drying chamber is formulated as

$$w_{gas}Y + w_{sl}X_{sl,d} + dw_{gas}Y_0 = (w_{gas} + dw_{gas})(Y + dY) + w_{sl}(X_{sl,d} + dX_{sl,d}) \tag{95}$$

where w_{gas} is the mass flow rate of drying medium on dry basis, w_{sl} is mass flow rate

of slurry, Y_0 is the humidity of drying medium at inlet conditions, Y is the humidity of drying medium, $X_{sl,d}$ is the droplet moisture content on wet basis and dw_{gas} is the term which accounts for spray expansion, as illustrated in Fig. 7.

Simplifying Eq. (95) results in

$$dw_{gas}Y_0 = dw_{gas}Y + w_{gas}dY + dw_{gas}dY + w_{sl}dX_{sl,d} \tag{96}$$

The term $dw_{gas}dY$ is small in comparison with other terms, hence it can be neglected.

$$dw_{gas}Y_0 = dw_{gas}Y + w_{gas}dY + w_{sl}dX_{sl,d} \tag{97}$$

Combining similar terms yields

$$w_{gas}dY = (Y_0 - Y)\, dw_{gas} - w_{sl}dX_{sl,d} \tag{98}$$

Rearranging Eq. (98) results in

$$\frac{dY}{dh} = \frac{(Y_0 - Y)}{w_{gas}}\frac{dw_{gas}}{dh} - \frac{w_{sl}}{w_{gas}}\frac{dX_{sl,d}}{dh} \tag{99}$$

3.2.4 Energy balance of drying medium

The energy balance over the shell in the drying chamber is derived as

$$w_{gas}i_{gas} + w_{sl}i_{sl} + dw_{gas}i_{gas,0} = (w_{gas} + dw_{gas})\,(i_{gas} + di_{gas}) + w_{sl}\,(i_{sl} + di_{sl})\,, \tag{100}$$

where i_{gas} is the enthalpy of drying medium, i_{sl} is the enthalpy of slurry, $i_{gas,0}$ is the enthalpy of drying media at inlet conditions.

Simplifying Eq. (100)

$$dw_{gas}i_{gas,0} = w_{gas}di_{gas} + dw_{gas}i_{gas} + dw_{gas}di_{gas} + w_{sl}di_{sl}$$

and neglecting the term $dw_{gas}di_{gas}$ gives

$$dw_{gas}i_{gas,0} = w_{gas}di_{gas} + dw_{gas}i_{gas} + w_{sl}di_{sl}$$

The enthalpy of drying medium is defined as

$$i_{gas} = Cp_{gas}T_{gas} + (Cp_{lv}T_{gas} + \lambda_l)\, Y, \tag{101}$$

where Cp_{gas} is the specific heat capacity of drying medium, T_{gas} is the gas temperature, Cp_{lv} is the specific heat capacity of liquid vapor and λ_l is the latent heat of vaporization.

The enthalpy of slurry is given as

$$i_{sl} = (X_{sl,d}Cp_l + (1 - X_{sl,d})Cp_s)\, T_{sl}, \tag{102}$$

where Cp_l is the specific heat capacity of liquid, Cp_s is the specific heat capacity of solid and T_{sl} is the slurry temperature.

The derivative of i_{gas} by Eq. (101) is

$$\begin{aligned} di_{gas} &= Cp_{gas}dT_{gas} + Cp_{lv}T_{gas}dY + Cp_{lv}Y\,dT_{gas} + \lambda_l dY \\ &= (Cp_{gas} + Cp_{lv}Y)\, dT_{gas} + (Cp_{lv}T_{gas} + \lambda_l)\, dY \\ &= Cp_H dT_{gas} + (Cp_{lv}T_{gas} + \lambda_l)\, dY, \end{aligned} \tag{103}$$

where Cp_H is the specific heat capacity of humid media, $Cp_H = Cp_{gas} + Cp_{lv}Y$.

The derivative of i_{sl} by Eq. (102) is

$$\begin{aligned} di_{sl} &= Cp_l X_{sl,d}dT_{sl} + Cp_l T_{sl}dX_{sl,d} + (1 - X_{sl,d})Cp_s dT_{sl} - Cp_s T_{sl}dX_{sl,d} \\ &= (X_{sl,d}Cp_l + (1 - X_{sl,d})Cp_s)\, dT_{sl} + (Cp_l - Cp_s)T_{sl}dX_{sl,d} \end{aligned} \tag{104}$$

Substitution of Eqs. (103) and (104) into Eq. (102) yields

$$\begin{aligned} dw_{gas}\left(i_{gas,0}-i_{gas}\right) = w_{gas}\left[Cp_H dT_{gas} + \left(Cp_{lv}T_{gas}+\lambda_l\right)dY\right] + \\ w_{sl}\left[\left(X_{sl,d}Cp_l + (1-X_{sl,d})Cp_s\right)dT_{sl} + (Cp_l - Cp_s)T_{sl}dX_{sl,d}\right] \end{aligned} \tag{105}$$

Rearranging Eq. (105) results in

$$\begin{aligned} \left(i_{gas,0}-i_{gas}\right)dw_{gas} =& w_{gas}Cp_H dT_{gas} + w_{gas}\left(Cp_{lv}T_{gas}+\lambda_l\right)dY + \\ & w_{sl}\left(X_{sl,d}Cp_l + (1-X_{sl,d})Cp_s\right)dT_{sl} + w_{sl}(Cp_l - Cp_s)T_{sl}dX_{sl,d} \end{aligned}$$

or

$$\begin{aligned} w_{gas}Cp_H dT_{gas} =& \left(i_{g0}-i_{gas}\right)dw_{gas} - w_{gas}\left(Cp_{lv}T_{gas}+\lambda_l\right)dY - \\ & w_{sl}\left(X_{sl,d}Cp_l + (1-X_{sl,d})Cp_s\right)dT_{sl} - w_{sl}(Cp_l - Cp_s)T_{sl}dX_{sl,d} \end{aligned}$$

Finally, the distribution of temperature of drying medium along the height of the drying chamber is obtained as

$$\begin{aligned} \frac{dT_{gas}}{dh} = \frac{1}{w_{gas}Cp_H}\Bigg[&\left(i_{gas,0}-i_{gas}\right)\frac{dw_{gas}}{dh} - w_{gas}\left(Cp_{lv}T_{gas}+\lambda_l\right)\frac{dY}{dh} \\ &-w_{sl}\left(X_{sl,d}Cp_l + (1-X_{sl,d})Cp_s\right)\frac{dT_{sl}}{dh} - w_{sl}(Cp_l - Cp_s)T_{sl}\frac{dX_{sl,d}}{dh}\Bigg] \end{aligned} \tag{106}$$

The term to account for expansion of spray, dw_{gas}/dh, can be determined on the basis of the increment of stream cross-section as

$$dw_{gas} = \frac{U_{gx}\rho_g}{1+Y}\left[\pi(r+dr)^2 - \pi r^2\right] \tag{107}$$

Dividing both sides of Eq. (107) by Δh and taking limits as $\Delta h \to 0$ yields

$$\frac{dw_{gas}}{dh} = 2\pi r\frac{U_{gx}\rho_g}{1+Y}\frac{dr}{dh} \tag{108}$$

3.3 Physical Properties and Correlations

The heat conductivity of wet core is defined as

$$k_{co} = \varepsilon k_l + (1 - \varepsilon) k_s \tag{109}$$

The heat conductivity of dry crust region is given as

$$k_{cr} = \varepsilon k_{mx} + (1 - \varepsilon) k_s \tag{110}$$

The heat conductivity of air-water mixture is evaluated as (Pakowski and Mujumdar, 1995)

$$k_{mx} = 2.425 \times 10^{-2} - 7.899 \times 10^{-5} T - 1.790 \times 10^{-8} T^2 - 8.570 \times 10^{-12} T^3, \tag{111}$$

where temperature T is given in degrees Celsius.

The effective diffusivity of water vapor in dry crust is calculated as (Ochoa-Tapia et al., 1994)

$$D_{cr} = \frac{2\varepsilon D_{wv}}{3 - \varepsilon} \tag{112}$$

and the diffusivity of water vapor is given as

$$D_{wv} = 0.22 \times 10^{-4} \left(\frac{T}{273.15} \right)^{1.75}, \tag{113}$$

where temperature T is given in degrees Kelvin.

The density, viscosity, heat capacity and heat conductivity of air are estimated as

$$\rho_{gas} = 1.2929 \cdot \left(\frac{273.15}{273.15 + T} \right) \tag{114}$$

$$\mu_{gas} = 1.720 \times 10^{-5} + 4.568 \times 10^{-8} T \tag{115}$$

$$Cp_{gas} = 969.542 + 6.801 \times 10^{-2}T + 16.569 \times 10^{-5}T^2 - 67.828 \times 10^{-9}T^3 \quad (116)$$

$$k_{gas} = 1.731 \cdot \left(0.014 + 4.296 \times 10^{-5}T\right), \quad (117)$$

where temperature is given in degrees Celsius for all correlations except the one for Cp_{gas}.

The correlation for the latent heat of evaporation is

$$\lambda_l = 3.15 \times 10^6 - 2.38 \times 10^3 T, \quad (118)$$

where temperature T is given in degrees Celsius.

The thermodynamic properties of water are calculated using the subset of equations developed for industrial use by the International Association for the Properties of Water and Steam, IAPWS-IF97 (2007).

The convective heat and mass transfer coefficients are calculated by utilizing Ranz and Marshall (1952) correlations

$$k_h = \frac{\mathrm{Nu} \cdot k_{gas}}{d_p}, \quad \mathrm{Nu} = 2 + 0.65 \cdot \mathrm{Re}^{1/2}\mathrm{Pr}^{1/3} \quad (119)$$

$$k_m = \frac{\mathrm{Sh} \cdot D_{wv}}{d_p}, \quad \mathrm{Sh} = 2 + 0.65 \cdot \mathrm{Re}^{1/2}\mathrm{Sc}^{1/3}, \quad (120)$$

where Nu, Sh, Re, Pr and Sc are the Nusselt, Sherwood, Reynolds, Prandtl and Schmidt numbers for drying air, respectively. These dimensionless numbers are defined as

$$\mathrm{Re} = \frac{\rho_{gas} d_p U_{gas}}{\mu_{gas}}, \quad \mathrm{Pr} = \frac{Cp_{gas}\mu_{gas}}{k_{gas}}, \quad \mathrm{Sc} = \frac{\mu_{gas}}{\rho_{gas} D_{wv}} \quad (121)$$

The droplet moisture is defined as

$$X_{sl,d} = 1 - \left[\frac{4\pi R_{in}^3 \rho_s \left(1 - \varepsilon\right)}{3W_t}\right], \quad (122)$$

where W_t is the variation of droplet weight with drying time calculated as a function

of position of evaporation interface s

$$W_t = \frac{4}{3}\pi \left[\rho_l \varepsilon s^3 + \rho_s \left(1-\varepsilon\right) R_{in}^3\right] \tag{123}$$

4 Numerical Approach

A fully implicit finite-difference method is used for the numerical solution of partial differential equations. The various difference approximations of derivatives are summarized in Table 2.

Table 2: Summary of difference approximations of partial derivatives.

First-order spatial derivative:	
- forward difference	$\frac{\partial \varphi}{\partial r} = \frac{\varphi_{i+1} - \varphi_i}{\Delta r}$
- backward difference	$\frac{\partial \varphi}{\partial r} = \frac{\varphi_i - \varphi_{i-1}}{\Delta r}$
- central difference	$\frac{\partial \varphi}{\partial r} = \frac{\varphi_{i+1} - \varphi_{i-1}}{2\Delta r}$
Second-order spatial derivative:	
- central difference	$\frac{\partial^2 \varphi}{\partial r^2} = \frac{\varphi_{i+1} - 2\varphi_i + \varphi_{i-1}}{(\Delta r)^2}$
First-order time derivative:	
- fully implicit difference	$\frac{\partial \varphi}{\partial t} = \frac{\varphi_i^{t+\Delta t} - \varphi_i^t}{\Delta t}$

The tridiagonal system of linear equations is obtained by discretizaton of partial differential equations using the corresponding finite difference approximations.

$$A_i \cdot \varphi_i = B_i \cdot \varphi_{i+1} + C_i \cdot \varphi_{i-1} + D_i, \tag{124}$$

where A_i, B_i, C_i and D_i are coefficients.

4.1 Simulation of a droplet drying in constant rate period

The uniform spatial grid is utilized in the constant rate period, as illustrated in Fig. 8. The grid is divided into two parts; the wet core region, nodes 1 to M, and the free liquid region, nodes M to N.

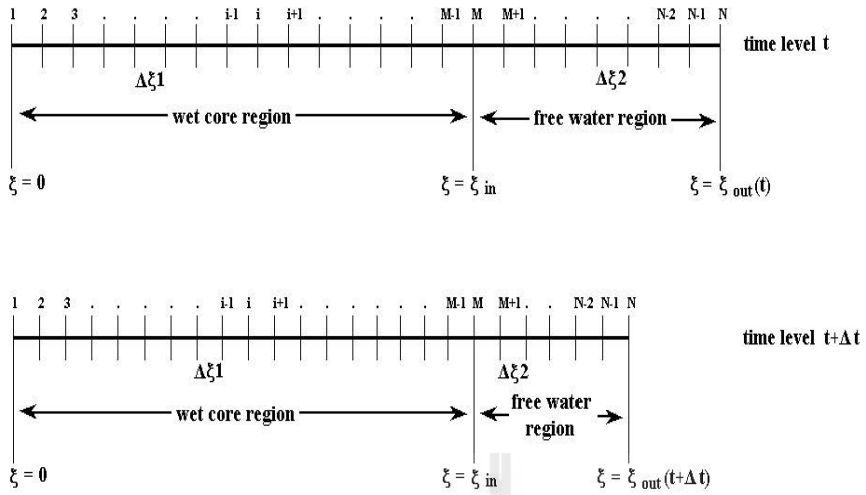

Figure 8: Grid distribution in the constant rate period.

Using the forward difference approximation of the first-order derivative, the boundary equation at the droplet center, node 1, by Eq. (14) is discretized as

$$\frac{\varphi_2 - \varphi_1}{\Delta\xi_1} = 0, \tag{125}$$

where φ corresponds to T_{co}.

Equation (125) is simplified as

$$\varphi_1 = \varphi_2 \tag{126}$$

Thus, the coefficients of linear system of equation are

$$A_1 = 1;\ B_1 = 1;\ C_1 = 0;\ D_1 = 0 \tag{127}$$

Using the central difference approximations of the first- and second-order spatial derivatives, and the fully implicit scheme for the time derivative, Eq. (11) that describes the temperature distribution in the wet core is discretized at the interior nodes $2 \leq i \leq M-1$ as

$$\alpha_1' \frac{\varphi_i - \varphi_i^*}{\Delta t} = \frac{\varphi_{i+1} - 2\varphi_i + \varphi_{i-1}}{(\Delta\xi_1)^2} + \frac{2}{\xi} \cdot \frac{\varphi_{i+1} - \varphi_{i-1}}{2\Delta\xi_1}, \tag{128}$$

where φ_i represents temperature at the time level $t + \Delta t$ and φ_i^* at t, respectively.

Rearranging Eq. (128) results in

$$\left(\frac{\alpha_1'}{\Delta t} + \frac{2}{(\Delta\xi_1)^2}\right)\varphi_i = \left(\frac{1}{(\Delta\xi_1)^2} + \frac{1}{\xi\,(\Delta\xi_1)}\right)\varphi_{i+1} + \left(\frac{1}{(\Delta\xi_1)^2} - \frac{1}{\xi\,(\Delta\xi_1)}\right)\varphi_{i-1} + \frac{\alpha_1'\varphi_i^*}{\Delta t} \tag{129}$$

Multiplying all terms by $\dfrac{\Delta t}{\alpha_1'}$ gives

$$\left(1 + \frac{2\Delta t}{\alpha_1'(\Delta\xi_1)^2}\right)\varphi_i = \left(\frac{\Delta t}{\alpha'_1(\Delta\xi_1)^2} + \frac{\Delta t}{\alpha'_1\xi\,(\Delta\xi_1)}\right)\varphi_{i+1} + \left(\frac{\Delta t}{\alpha_1'(\Delta\xi_1)^2} - \frac{\Delta t}{\alpha_1'\xi\,(\Delta\xi_1)}\right)\varphi_{i-1} + \varphi_i^* \tag{130}$$

Therefore, the coefficients of system of linear equations (124) are

$$\begin{aligned} A_i &= 1 + \frac{2\Delta t}{\alpha_1'(\Delta\xi_1)^2} \\ B_i &= \frac{\Delta t}{\alpha_1'(\Delta\xi_1)^2} + \frac{\Delta t}{\alpha'_1\xi\,(\Delta\xi_1)} \\ C_i &= \frac{\Delta t}{\alpha_1'(\Delta\xi_1)^2} \frac{\Delta t}{\alpha_1'\xi\,(\Delta\xi_1)} \\ D_i &= \varphi_i^* \end{aligned} \tag{131}$$

The boundary equation (29) at the outer surface of wet core, node M is discretized using the backward an forward difference approximations of the first-order derivatives as

$$-k_{co}\frac{\varphi_M - \varphi_{M-1}}{\Delta\xi_1} = -k_l\frac{\varphi_{M+1} - \varphi_M}{\Delta\xi_2} \tag{132}$$

Collecting terms for the same node results in

$$\left(\frac{k_l}{\Delta\xi_2} + \frac{k_{co}}{\Delta\xi_1}\right)\varphi_M = \frac{k_l}{\Delta\xi_2}\varphi_{M+1} + \frac{k_{co}}{\Delta\xi_1}\varphi_{M-1} \tag{133}$$

The coefficients of the system of linear equation are

$$\begin{aligned} A_M &= \frac{k_{co}}{\Delta\xi_1} + \frac{k_w}{\Delta\xi_2} \\ B_M &= \frac{k_l}{\Delta\xi_2} \\ C_M &= \frac{k_{co}}{\Delta\xi_1} \\ D_M &= 0 \end{aligned} \tag{134}$$

Equation (24) describing the temperature distribution in the free liquid region is written in the discrete form at the interior nodes $M+1 \leq i \leq N-1$ as

$$\alpha_2' \frac{\varphi_i - \varphi_i^*}{\Delta t} = \frac{\varphi_{i+1} - 2\varphi_i + \varphi_{i-1}}{(\Delta\xi_2)^2} + \frac{2}{\xi} \cdot \frac{\varphi_{i+1} - \varphi_{i-1}}{2(\Delta\xi_2)} \tag{135}$$

Rearranging Eq. (135) results in

$$\begin{aligned} \left(1 + \frac{2\Delta t}{\alpha_2'(\Delta\xi_2)^2}\right)\varphi_i = &\left(\frac{\Delta t}{\alpha_2'(\Delta\xi_2)^2} + \frac{\Delta t}{\alpha_2'\xi\,(\Delta\xi_2)}\right)\varphi_{i+1} + \\ &\left(\frac{\Delta t}{\alpha_2'(\Delta\xi_2)^2} - \frac{\Delta t}{\alpha_2'\xi\,(\Delta\xi_2)}\right)\varphi_{i-1} + \varphi_i^* \end{aligned} \tag{136}$$

The coefficients of the system of linear equations are

$$\begin{aligned} A_i &= 1 + \frac{2\Delta t}{\alpha_2'(\Delta\xi_2)^2} \\ B_i &= \frac{\Delta t}{\alpha_2'(\Delta\xi_2)^2} + \frac{\Delta t}{\alpha_2'\xi\,(\Delta\xi 2)} \\ C_i &= \frac{\Delta t}{\alpha_2'(\Delta\xi_2)^2} - \frac{\Delta t}{\alpha_2'\xi\,(\Delta\xi_2)} \\ D_i &= \varphi_i^* \end{aligned} \tag{137}$$

Equation (35) at node N is discretized using the backward difference approximation

of the first-order spatial derivative as

$$\lambda_l \frac{\xi_{out} - \xi^*_{out}}{\Delta t} = \alpha'_3 \left(\varphi_N - \varphi_{\text{gas}}\right) + \alpha'_4 \frac{\varphi_N - \varphi_{N-1}}{\Delta \xi_2} \tag{138}$$

Collecting terms for the same node results in

$$\left(\alpha'_3 + \frac{\alpha'_4}{\Delta \xi_2}\right) \varphi_i = \frac{\alpha'_4}{\Delta \xi_2} \varphi_{N-1} + \left(-\lambda_l \frac{\xi_{out} - \xi^*_{out}}{\Delta t} + \alpha'_3 \varphi_{\text{gas}}\right) \tag{139}$$

The coefficients of the system of linear equations are

$$\begin{aligned} A_N &= \alpha'_3 + \frac{\alpha'_4}{\Delta \xi_2} \\ B_N &= 0 \\ C_N &= \frac{\alpha'_4}{\Delta \xi_2} \\ D_N &= -\lambda_l \frac{\xi_{out} - \xi^*_{out}}{\Delta t} + \alpha'_3 \varphi_{\text{gas}} \end{aligned} \tag{140}$$

The discrete form of Eq. (43) is

$$\frac{\xi_{out} - \xi^*_{out}}{\Delta t} = -\alpha'_5 \left(C_{lv} - C_{gas}\right) \tag{141}$$

The position of evaporation interface is calculated using Eq. (141) as

$$\xi_{out} = \xi^*_{out} + \alpha'_5 \Delta t \left(C_{lv} - C_{gas}\right), \tag{142}$$

where the vapor concentration at the interface C_{lv} is evaluated using Eq. (72) at the known value of the interface temperature φ_N.

To start iterations at time $t + \Delta t$, the position of evaporation interface is estimated as

$$\xi_{out} = \xi^*_{out} - i \cdot \delta\xi \qquad i = 1, \ldots, I_{max}, \tag{143}$$

where i and $\delta\xi$ represent the iteration level and the incremental decrease, respectively, and I_{max} is the maximum number of iterations.

Using the estimated value of interface position, the temperature distributions are calculated in the wet core and free liquid regions by solution of the linear tridiagonal system of equations, Eq. (124). Then, the temperature at the node φ_N is used to calculate position by Eq. (141). Finely, the estimated value of ξ_{out} is compared with the calculated one.

The convergence criterion is defined as

$$\frac{\left|\left(\xi_{out}-\xi^*_{out}\right)_{\text{calc.}}\right|-\left|\left(\xi_{out}-\xi^*_{out}\right)_{\text{est.}}\right|}{\left|\left(\xi_{out}-\xi^*_{out}\right)_{\text{calc.}}\right|}\times 100\leq\Phi_\xi, \tag{144}$$

where Φ_ξ is the percent tolerance.

The simulation of the constant rate period is terminated at $\xi_{out}=\xi_{in}$. Thus, the termination criterion is defined as

$$M=N-2, \tag{145}$$

where N and M correspond to the grid levels at ξ_{out} and ξ_{in}, respectively.

The variation of the droplet weight during drying process in the constant rate period is calculated as

$$W_t(t)=\frac{4}{3}\pi\left[\rho_l\left(R^3_{\text{out}}(t)-R^3_{\text{in}}\right)+\rho_l\varepsilon R^3_{\text{in}}+\rho_s\left(1-\varepsilon\right)R^3_{\text{in}}\right], \tag{146}$$

where $R_{\text{out}}(t)=R_{\text{init}}\xi_{\text{out}}(t)$.

The droplet average temperature is estimated as

$$T_{av}=\frac{3}{R^3_{\text{out}}(t)}\int_0^{R_{\text{out}}(t)}r^2T(r)dr \tag{147}$$

The integral above is evaluated by using a trapezoidal rule.

The flowchart of the calculation procedure of slurry drying in the constant rate period is illustrated in Fig. 9. The coefficients for all nodes are summarized in Table 3.

Table 3: Summary of coefficients of system of linear algebraic equations (124) for temperature in the constant rate period.

Node	Coefficients A, B, C, D
1	$A = 1, B = 1, C = 0, D = 0$
$2 \leq i \leq M-1$	$A = 1 + \dfrac{2\Delta t}{\alpha_1'(\Delta\xi_1)^2}, \quad B = \dfrac{\Delta t}{\alpha_1'(\Delta\xi_1)^2} + \dfrac{\Delta t}{\alpha_1'\xi\,(\Delta\xi_1)}$ $C = \dfrac{\Delta t}{\alpha_1'(\Delta\xi_1)^2} - \dfrac{\Delta t}{\alpha_1'\xi\,(\Delta\xi_1)}, \quad D = \varphi_i^*$
M	$A = \dfrac{k_{co}}{\Delta\xi_1} + \dfrac{k_w}{\Delta\xi_2}, \quad B = \dfrac{k_l}{\Delta\xi_2}$ $C = \dfrac{k_{co}}{\Delta\xi_1}, \quad D = 0$
$M+1 \leq i \leq N-1$	$A = 1 + \dfrac{2\Delta t}{\alpha_2'(\Delta\xi_2)^2}, \quad B = \dfrac{\Delta t}{\alpha_2'(\Delta\xi_2)^2} + \dfrac{\Delta t}{\alpha_2'\xi\,(\Delta\xi_2)}$ $C = \dfrac{\Delta t}{\alpha_2'(\Delta\xi_2)^2} - \dfrac{\Delta t}{\alpha_2'\xi\,(\Delta\xi_2)}, \quad D = \varphi_i^*$
N	$A = \alpha_3' + \dfrac{\alpha_4'}{\Delta\xi_2}, \quad B = 0$ $C = \dfrac{\alpha_4'}{\Delta\xi_2}, \quad D = -\lambda_l \dfrac{\xi_{out} - \xi_{out}^*}{\Delta t} + \alpha_3'\varphi_{\text{gas}}$

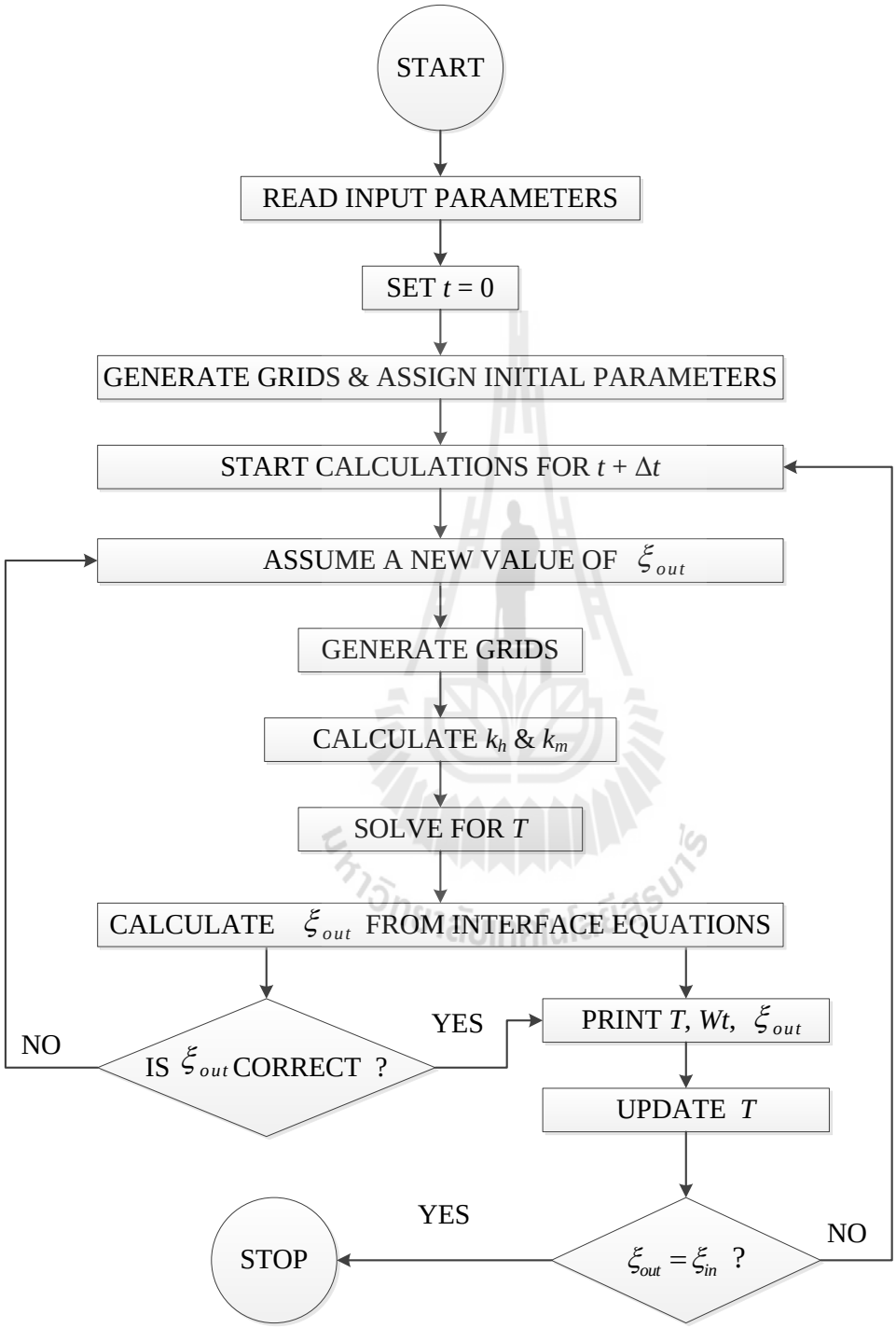

Figure 9: Calculation procedure for slurry drying in the constant rate period.

4.2 Simulation of a droplet drying in falling rate period

The grid distributions in the falling rate period are illustrated in Fig. 10. The grid is divided into two parts; the wet core region, nodes 1 to M and the dry crust region, nodes M to N. The nodes are distributed uniformly.

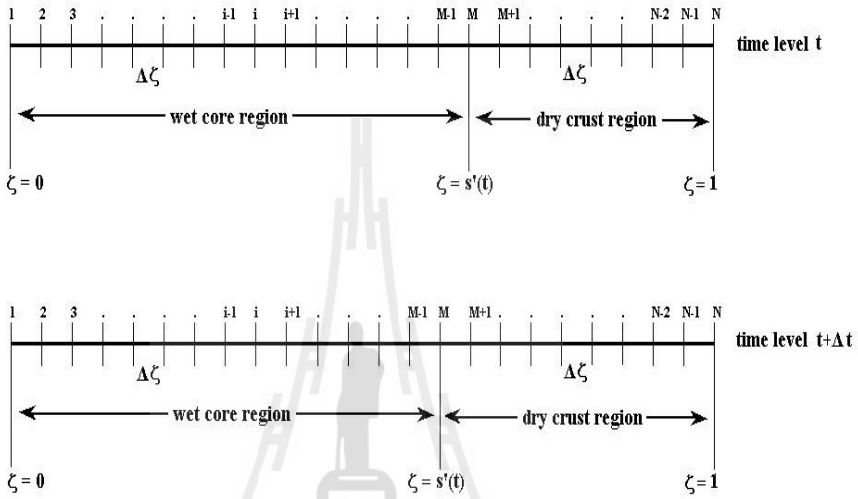

Figure 10: Grid distribution in the falling rate period.

The boundary equation (50) for temperature at the particle center is discretized using the forward difference approximation of derivative.

$$\frac{\varphi_2 - \varphi_1}{\Delta\zeta} = 0 \tag{148}$$

or

$$\varphi_1 = \varphi_2 \tag{149}$$

The coefficients of the system of linear equations are

$$A_1 = 1;\ B_1 = 1;\ C_1 = 0;\ D_1 = 0 \tag{150}$$

The temperature in the wet core region at the node i, $2 \leq i \leq M-1$, is obtained

by substitution of derivatives in Eq. (47) with the central difference approximations

$$\beta_1' \frac{\varphi_i - \varphi_i^*}{\Delta t} = \frac{\varphi_{i+1} - 2\varphi_i + \varphi_{i-1}}{(\Delta\zeta)^2} + \frac{2}{\zeta} \cdot \frac{\varphi_{i+1} - \varphi_{i-1}}{2\Delta\zeta} \tag{151}$$

Rearranging Eq. (151) results in

$$\begin{aligned} \left(1 + \frac{2\Delta t}{\beta_1'(\Delta\zeta)^2}\right) \varphi_i = &\left(\frac{\Delta t}{\beta_1'(\Delta\zeta)^2} + \frac{\Delta t}{\beta_1'\zeta\,(\Delta\zeta)}\right) \varphi_{i+1} + \\ &\left(\frac{\Delta t}{\beta_1'(\Delta\zeta)^2} - \frac{\Delta t}{\beta_1'\zeta\,(\Delta\zeta)}\right) \varphi_{i-1} + \varphi_i^* \end{aligned} \tag{152}$$

The coefficients of Eq. (124) are

$$\begin{aligned} A_i &= 1 + \frac{2\Delta t}{\beta_1'(\Delta\zeta)^2} \\ B_i &= \frac{\Delta t}{\beta_1'(\Delta\zeta)^2} + \frac{\Delta t}{\beta'_1\zeta\,(\Delta\zeta)} \\ C_i &= \frac{\Delta t}{\beta_1'(\Delta\zeta)^2} - \frac{\Delta t}{\beta_1'\zeta\,(\Delta\zeta)} \\ D_i &= \varphi_i^* \end{aligned} \tag{153}$$

The concentration of water vapor in the wet core region is assigned to zero

$$C_{wv} = 0 \tag{154}$$

Thus,

$$C_i = 0, \tag{155}$$

for $1 \leq i \leq M-1$ and the corresponding coefficients of Eq. (11) are

$$A_i = 1;\ B_i = 0;\ C_i = 0;\ D_i = 0 \tag{156}$$

The equation for temperature at the evaporation interface $\zeta = s'(t)$, node M, is

derived by discretizaton of Eq. (60) using the forward and backward finite difference approximations of derivatives

$$\lambda_l \frac{s' - s'^*}{\Delta t} = -\beta_4' \frac{\varphi_{M+1} - \varphi_M}{\Delta\zeta} + \beta_5' \frac{\varphi_M - \varphi_{M-1}}{\Delta\zeta} \tag{157}$$

Rearranging Eq. (157) results in

$$\left(-\frac{\beta_4'}{\Delta\zeta} - \frac{\beta_5'}{\Delta\zeta}\right)\varphi_M = -\left(\frac{\beta_4'}{\Delta\zeta}\right)\varphi_{M+1} - \left(\frac{\beta_5'}{\Delta\zeta}\right)\varphi_{M-1} - \frac{\lambda_l\left(s' - s'^*\right)}{\Delta t} \tag{158}$$

The coefficients of Eq. (124) are

$$\begin{aligned} A_M &= -\frac{\beta_4'}{\Delta\zeta} - \frac{\beta_5'}{\Delta\zeta} \\ B_M &= -\frac{\beta_4'}{\Delta\zeta} \\ C_M &= -\frac{\beta_5'}{\Delta\zeta} \\ D_M &= -\frac{\lambda_l\left(s' - s'^*\right)}{\Delta t} \end{aligned} \tag{159}$$

The vapor concentration at the evaporation interface is calculated using the discrete form of Eq. (11)

$$C_M = \frac{P^{vap}\left(\varphi_M\right)}{R_{gas}\varphi_M} \tag{160}$$

and the corresponding coefficients are

$$A_M = 1;\ B_M = 0;\ C_M = 0;\ D_M = \frac{P^{vap}\left(\varphi_M\right)}{R_{gas}\varphi_M} \tag{161}$$

The temperature in the crust layer at interior nodes $M+1 \le i \le N-1$ is obtained using the discretized Eq. (56)

$$\beta_2' \frac{\varphi_i - \varphi_i^*}{\Delta t} = \frac{\varphi_{i+1} - 2\varphi_i + \varphi_{i-1}}{\left(\Delta\zeta\right)^2} + \frac{2}{\zeta} \cdot \frac{\varphi_{i+1} - \varphi_{i-1}}{2\Delta\zeta} \tag{162}$$

Collecting terms for the same node results in

$$\left(1+\frac{2\Delta t}{\beta_2'\left(\Delta\zeta\right)^2}\right)\varphi_i=\left(\frac{\Delta t}{\beta_2'(\Delta\zeta)^2}+\frac{\Delta t}{2\beta_2'\zeta\left(\Delta\zeta\right)}\right)\varphi_{i+1}+\left(\frac{\Delta t}{\beta'_2(\Delta\zeta)^2}-\frac{\Delta t}{2\beta_2'\zeta\left(\Delta\zeta\right)}\right)\varphi_{i-1}+\varphi_i^* \tag{163}$$

The coefficients are

$$\begin{aligned}A_i&=1+\frac{2\Delta t}{\beta_2'\left(\Delta\zeta\right)^2}\\B_i&=\frac{\Delta t}{\beta_2'(\Delta\zeta)^2}+\frac{\Delta t}{2\beta_2'\zeta\left(\Delta\zeta\right)}\\C_i&=\frac{\Delta t}{\beta_2'(\Delta\zeta)^2}-\frac{\Delta t}{2\beta_2'\zeta\left(\Delta\zeta\right)}\\D_i&=\varphi_i^*\end{aligned} \tag{164}$$

The vapor concentration in the crust layer is calculated by the discretized form of Eq. (69)

$$\beta_6'\frac{C'_i-{C'_i}^*}{\Delta t}=\frac{C'_{i+1}-2C'_i+C'_{i-1}}{\left(\Delta\zeta\right)^2}+\frac{2}{\zeta}\cdot\frac{C'_{i+1}-C'_{i-1}}{2\Delta\zeta}, \tag{165}$$

which can be rearranged as

$$\left(1+\frac{2\Delta t}{\beta'_6(\Delta\zeta)^2}\right)C'_i=\left(\frac{\Delta t}{\beta_6'(\Delta\zeta)^2}+\frac{\Delta t}{\beta_6'\zeta\left(\Delta\zeta\right)}\right)C'_{i-1}+\left(\frac{\Delta t}{\beta_6'(\Delta\zeta)^2}-\frac{\Delta t}{\beta_6'\zeta\left(\Delta\zeta\right)}\right)C'_{i+1}+{C'_i}^* \tag{166}$$

The coefficients are

$$\begin{aligned}A_i&=1+\frac{2\Delta t}{\beta_6'(\Delta\zeta)^2}\\B_i&=\frac{\Delta t}{\beta_6'(\Delta\zeta)^2}+\frac{\Delta t}{\beta_6'\zeta\left(\Delta\zeta\right)}\\C_i&=\frac{\Delta t}{\beta_6'(\Delta\zeta)^2}-\frac{\Delta t}{\beta_6'\zeta\left(\Delta\zeta\right)}\\D_i&={C'_i}^*\end{aligned} \tag{167}$$

The temperature at the outer droplet surface is obtained using the discrete form of

Eq. (67)

$$-k_{cr}\frac{\varphi_N-\varphi_{N-1}}{\Delta\zeta}=R_{in}k_h\left(\varphi_N-1\right) \tag{168}$$

Simplifying Eq. (168) results in

$$\left(1+\frac{\Delta\zeta R_{in}k_h}{k_{cr}}\right)\varphi_N=\varphi_{N-1}+\frac{\Delta\zeta R_{in}k_h}{k_{cr}} \tag{169}$$

The coefficients are

$$A_N=1+\frac{\Delta\zeta R_{in}k_h}{k_{cr}};\ B_N=0;\ C_N=1;\ D_N=\frac{\left(\Delta\zeta\right)R_{in}k_h}{k_{cr}} \tag{170}$$

The boundary condition for vapor concentration at $\zeta = 1$ by Eq. (74) can be rewritten in discrete form as

$$-D_{cr}\frac{C'_N-C'_{N-1}}{\Delta\zeta}=R_{\text{in}}k_m\left(C'_N-1\right) \tag{171}$$

or

$$\left(1+\frac{R_{\text{in}}k_m\Delta\zeta}{D_{cr}}\right)C'_N=C'_{N-1}+\frac{R_{\text{in}}k_m\left(\Delta\zeta\right)}{D_{cr}} \tag{172}$$

The coefficients are

$$A_N=1+\frac{R_{\text{in}}k_m\left(\Delta\zeta\right)}{D_{cr}};\ B_N=0;\ C_N=1;\ D_N=\frac{R_{in}k_m\left(\Delta\zeta\right)}{D_{cr}} \tag{173}$$

The discrete form of the mass balance of vapor at the evaporation interface, Eq. (63), is

$$\frac{s'-s'^*}{\Delta t}=\beta'_7\frac{C'_{M+1}-C'_M}{\left(\Delta\zeta\right)} \tag{174}$$

The position of interface is calculated as

$$s'=s'^*+\beta'_7\frac{C'_{M+1}-C'_M}{\left(\Delta\zeta\right)}\Delta t \tag{175}$$

The time step is estimated assuming that the interface moves exactly one grid in Δt

$$\Delta t = \Delta t_{guess} - k \cdot \delta t, \qquad k = 1, \ldots, K_{\max}, \tag{176}$$

where k is the iteration level, $K_{\max}$ is the maximum number of iterations, δt is the incremental time and Δt_{guess} is the initial guess of time step.

The convergence criterion for the interface position is

$$\frac{\left|(s' - s'^{*})_{\text{calc.}} - \Delta\zeta\right|}{\Delta\zeta} \times 100 \leq \Phi_s, \tag{177}$$

where Φ_s is the percent of tolerance.

The convergence criterion for the interface temperature is

$$\frac{\left|T_M^{j+1} - T_M^{j}\right|}{T_M^{j+1}} \times 100 \leq \Phi_T, \qquad j = 1, \ldots, J_{\max}, \tag{178}$$

where j represents the iteration level and $J_{\max}$ is the maximum number of iterations.

The variation of the droplet weight during drying process in the falling rate period is calculated as

$$W_t(t) = \frac{4}{3}\pi \left[\rho_l \varepsilon s^3(t) + \rho_s(1-\varepsilon)R_{\text{in}}^3\right], \tag{179}$$

where $s(t) = R_{\text{in}} s'(t)$

The droplet average temperature is calculated as

$$T_{av} = \frac{3}{R_{\text{in}}^3} \int_0^{R_{\text{in}}} r^2 T(r) dr \tag{180}$$

The flowchart of the calculation procedure of slurry drying in the falling rate period is illustrated in Fig. 11. The coefficients for all nodes are summarized in Tables 4 and 5.

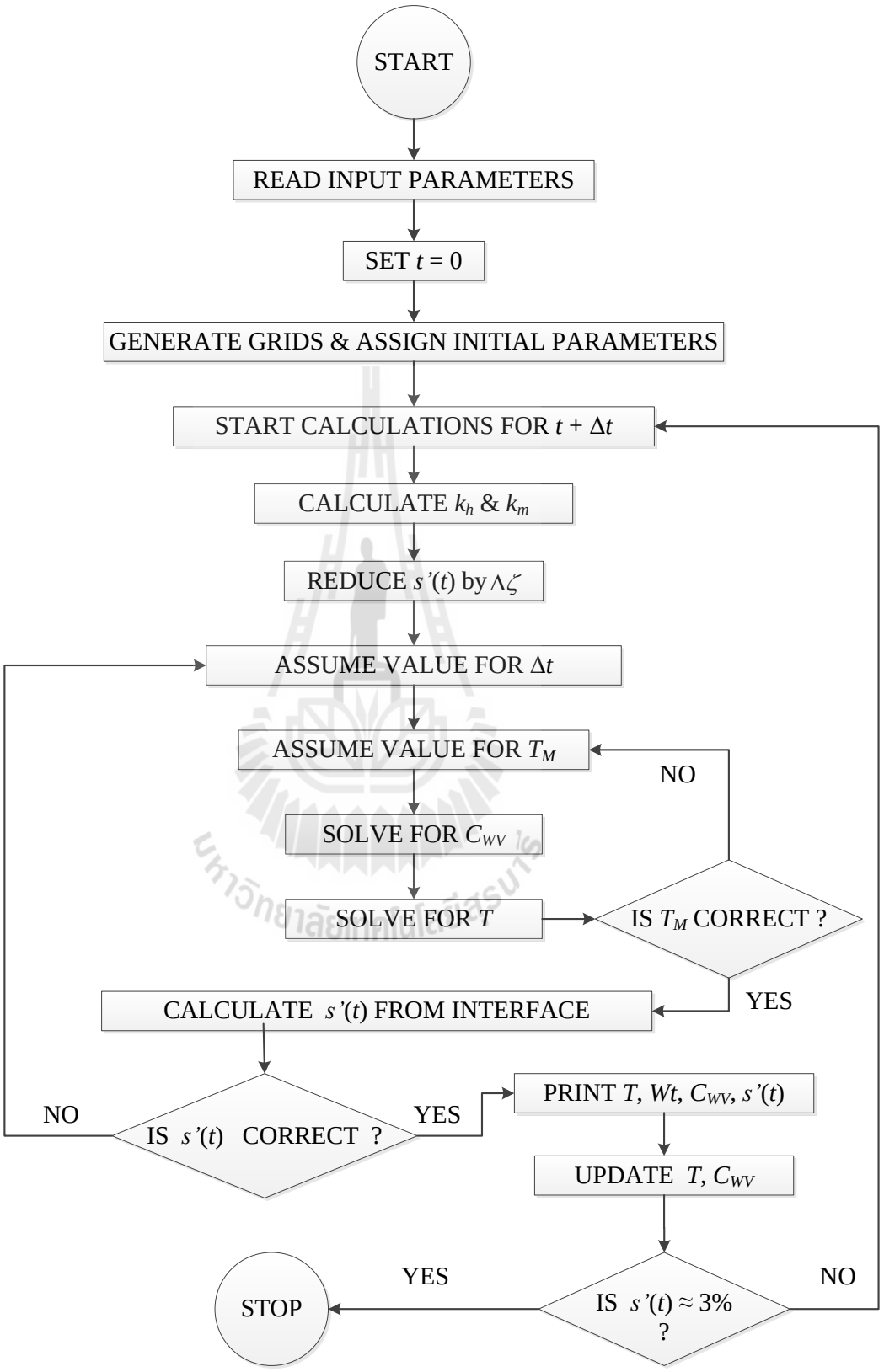

Figure 11: Calculation procedure for slurry drying in the falling rate period.

Table 4: Summary of coefficients of system of linear algebraic equations (124) for temperature in the falling rate period.

Node	Coefficients A, B, C, D
1	$A = 1, B = 1, C = 0, D = 0$
$2 \leq i \leq M-1$	$A = 1 + \frac{2\Delta t}{\beta_1'(\Delta\zeta)^2}, \quad B = \frac{\Delta t}{\beta_1'(\Delta\zeta)^2} + \frac{\Delta t}{\beta_1'\zeta\,(\Delta\zeta)}$ $C = \frac{\Delta t}{\beta_1'(\Delta\zeta)^2} - \frac{\Delta t}{\beta_1'\zeta\,(\Delta\zeta)}, \quad D = \varphi_i^*$
M	$A = -\frac{\beta_4'}{\Delta\zeta} - \frac{\beta_5'}{\Delta\zeta}, \quad B = -\frac{\beta_4'}{\Delta\zeta}$ $C = -\frac{\beta_5'}{\Delta\zeta}, \quad D = -\frac{\lambda_l\,(s' - s'^*)}{\Delta t}$
$M+1 \leq i \leq N-1$	$A = 1 + \frac{2\Delta t}{\beta_2'(\Delta\zeta)^2}, \quad B = \frac{\Delta t}{\beta_2'(\Delta\zeta)^2} + \frac{\Delta t}{\beta_2'\zeta\,(\Delta\zeta)}$ $C = \frac{\Delta t}{\beta_2'(\Delta\zeta)^2} - \frac{\Delta t}{\beta_2'\zeta\,(\Delta\zeta)}, \quad D = \varphi_i^*$
N	$A = 1 + \frac{\Delta\zeta R_{\text{in}} k_h}{k_{cr}}, \quad B = 0$ $C = 1, \quad D = \frac{(\Delta\zeta)\,R_{\text{in}} k_h}{k_{cr}}$

Table 5: Summary of coefficients of system of linear algebraic equations (124) for vapor concentration in the falling rate period.

Node	Coefficients A, B, C, D
$1 \leq i \leq M-1$	$A = 1, B = 0, C = 0, D = 0$
M	$A = 1, \quad B = 0\ , \quad C = 0, \quad D = \dfrac{P^{vap}\left(\varphi_M\right)}{R_{gas}\varphi_M}$
$M+1 \leq i \leq N-1$	$A = 1 + \dfrac{2\Delta t}{\beta_6'(\Delta\zeta)^2}, \quad B = \dfrac{\Delta t}{\beta_6'(\Delta\zeta)^2} + \dfrac{\Delta t}{\beta_6'\zeta\left(\Delta\zeta\right)}$ $C = \dfrac{\Delta t}{\beta_6'(\Delta\zeta)^2} - \dfrac{\Delta t}{\beta_6'\zeta\left(\Delta\zeta\right)}, \quad D = C_i^*$
N	$A = 1 + \dfrac{\Delta\zeta R_{\text{in}} k_m}{D_{cr}}, \quad B = 0$ $C = 1, \quad D = \dfrac{\left(\Delta\zeta\right) R_{\text{in}} k_m}{D_{cr}}$

4.3 Simulation of slurry drying in spray dryer

In this part, the spray drying chamber is divided into small control volumes along the axial distance. The control volume is small enough to assume the temperature, humidity and velocity of drying medium to be constant. The drying model of a slurry droplet developed in the first section will be used for calculation of heat and mass transfer between the drying medium and the droplets.

The droplet moisture content and the average temperature are calculated using the moisture and temperature distributions in the radial direction of the droplet by Eqs. (182) to (186).

- Constant rate period

$$W_t = \frac{4}{3}\pi \left[\rho_l \left(R_{out}^3 - R_{in}^3\right) + \rho_l \varepsilon R_{in}^3 + \rho_s \left(1-\varepsilon\right) R_{in}^3\right] \tag{181}$$

$$X_{sl,d}^{h+\Delta h} = 1 - \frac{4\pi R_{in}^3 \rho_s \left(1-\varepsilon\right)}{3W_t} \tag{182}$$

$$T_{\mathrm{av}}^{h+\Delta h} = \frac{3}{R_{out}^3}\int_0^{R_{out}} r^2 T\left(r\right) dr \tag{183}$$

- Falling rate period

$$W_t = \frac{4}{3}\pi \left[\rho_l \varepsilon s^3 + \rho_s \left(1-\varepsilon\right) R_{in}^3\right] \tag{184}$$

where s is wet core radius

$$X_{sl,d}^{h+\Delta h} = 1 - \frac{4\pi R_{in}^3 \rho_s \left(1-\varepsilon\right)}{3W_t} \tag{185}$$

$$T_{\mathrm{av}}^{h+\Delta h} = \frac{3}{R_{in}^3}\int_0^{R_{in}} r^2 T\left(r\right) dr \tag{186}$$

The heat and mass balances for the drying medium, Eqs. (99) and (102) can be modified as

$$\frac{dY}{dh} = \frac{\left(Y_0 - Y\right)}{w_{gas}} \cdot \frac{dw_{gas}}{dh} - \frac{w_{sl}}{w_{gas}} \cdot \frac{X_{sl,d}^{h+\Delta h} - X_{sl,d}^{h}}{\Delta h} \tag{187}$$

$$\frac{dT_{gas}}{dh} = \frac{1}{w_{gas} Cp_H} \Bigg[(i_{g0} - i_{gas}) \cdot \frac{dw_{gas}}{dh} - w_{gas} \cdot (Cp_{lv} T_{gas} + \lambda_l) \cdot \frac{dY}{dh} - w_{sl} \cdot \left(X^h_{sl,d} Cp_l + (1 - X_{sl,d}) Cp_s \right) \cdot \frac{T^{h+\Delta h}_{\text{av}} - T^h_{\text{av}}}{\Delta h} - w_{sl} \cdot (Cp_l - Cp_s) \cdot T^h_{\text{av}} \cdot \frac{X^{h+\Delta h}_{sl,d} - X^h_{sl,d}}{\Delta h} \Bigg] \tag{188}$$

The calculation procedure is illustrated in Fig. 12.

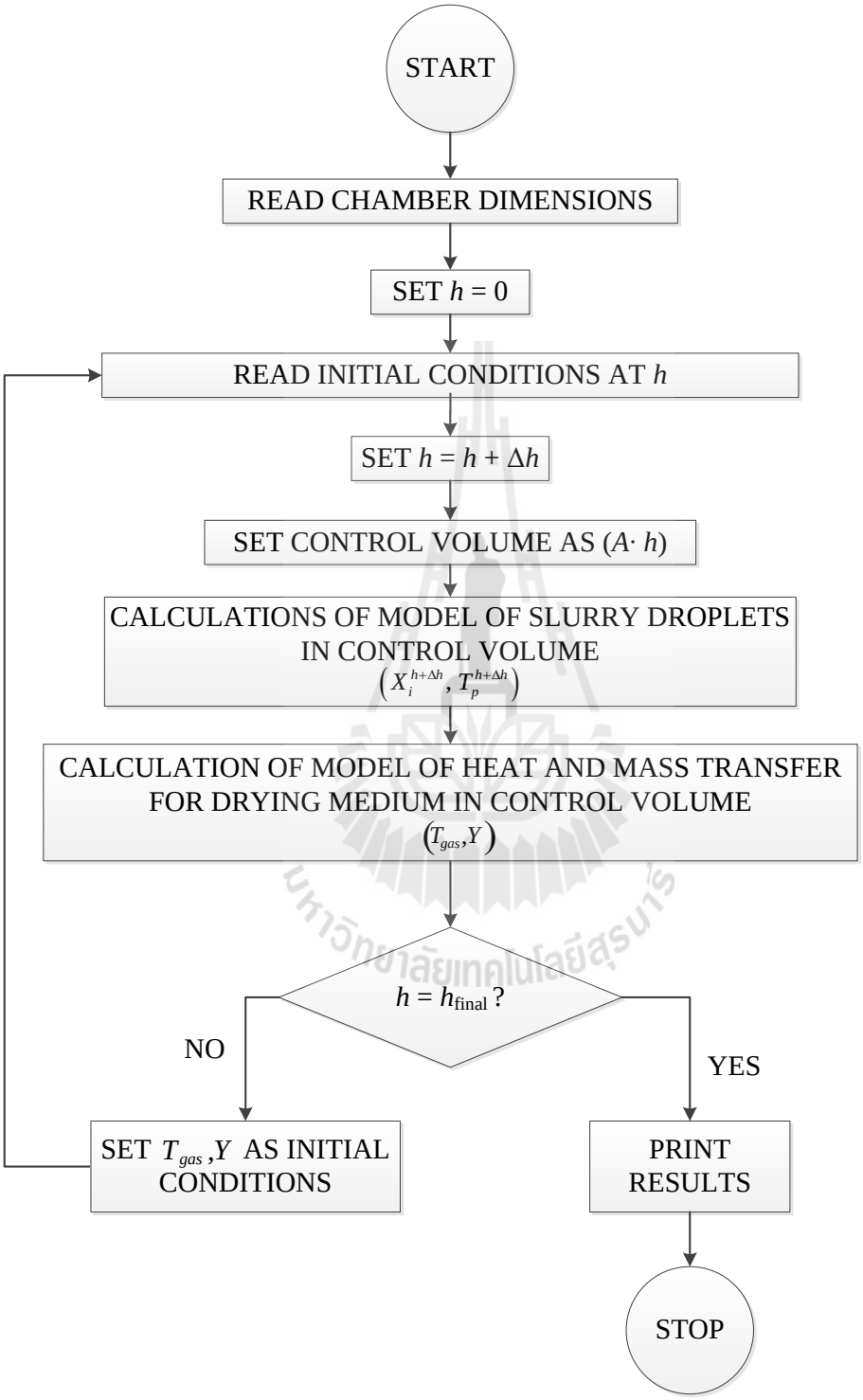

Figure 12: Calculation procedure for spray drying chamber

5 Results and Discussion

5.1 Analysis of drying kinetics of a slurry droplet

5.1.1 Validation of mathematical models

The validity of the present models was confirmed by comparison of calculated results with experimental data for drying of colloidal silica at 101°C with primary particles of 16 nm in diameter (Nesic et al. 1991). The variations of the droplet weight and average temperature were simulated separately for two drying periods and then combined in an one curve in Fig. 13.

The calculated results are in a good agreement with experimental data confirming the applicability of developed models.

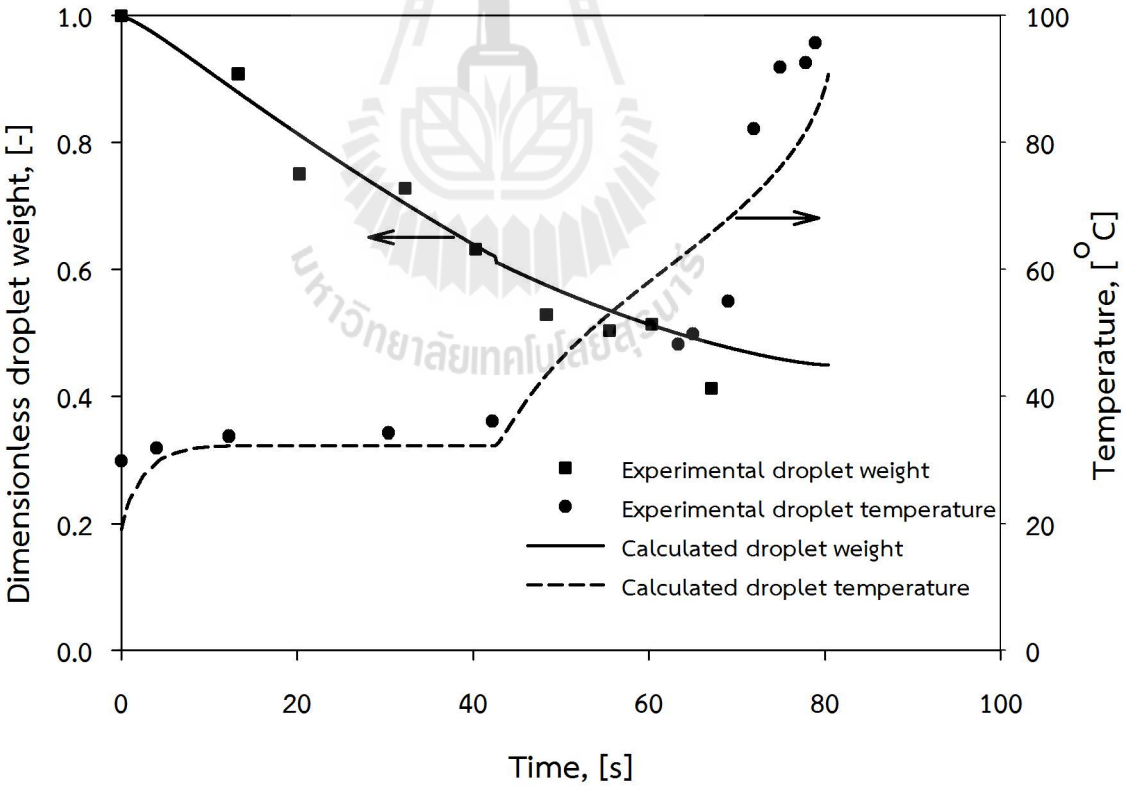

Figure 13: Comparison of model calculation and experimental data for drying of colloidal silica.

5.1.2 Heat and mass transfer during falling rate period

The effects of heat and mass transfer resistances inside the agglomerate were studied by varying the porosity of agglomerated product from 0.3 to 0.5, and the heat and mass transfer resistances outside agglomerated particle by changing the air flow rate from 1.0 to 2.0 m/s and the air temperature from 101 to 200 °C. The crust layer formed by nanoparticles is assumed to be of constant porosity equal to the porosity of dried product agglomerate. The drying time was measured from the beginning of the falling rate period.

Figure 14 illustrates the movement of the air-liquid interface, where the evaporation is taking place, with drying time. The rate of interface movement is constant during the constant drying rate period as this interface coincides with the outer droplet surface. During the falling rate period, the interface located inside the agglomerate moves inward with increasing speed as the small amount of water is left in the shrinking wet core, even the drying rate is significantly lower in comparison with one in the constant rate period by virtue of heat and mass transfer resistances in the crust region of agglomerate.

Figure 15 displays the temperature profiles in the agglomerate for various flow rates of drying air at drying times corresponding to dry crusts of uniform thicknesses of 0.00025 and 0.0005 m. The surface temperature increases at high flow rate due to the enhancement of convective heat transfer from the bulk air to the agglomerate surface. The temperature distributions in the agglomerate show a similar trend because the internal heat transfer resistances are constant for dry crust layers of the same thickness. The temperature of the wet core also increases following the rise of dry crust temperature.

At the same air flow rate, the difference in temperature between the agglomerate surface and the wet core rises with drying time as the growing crust layer causes the additional resistance to the heat transfer inside the agglomerate.

The concentration of water vapor in the crust layer of agglomerate slightly increases

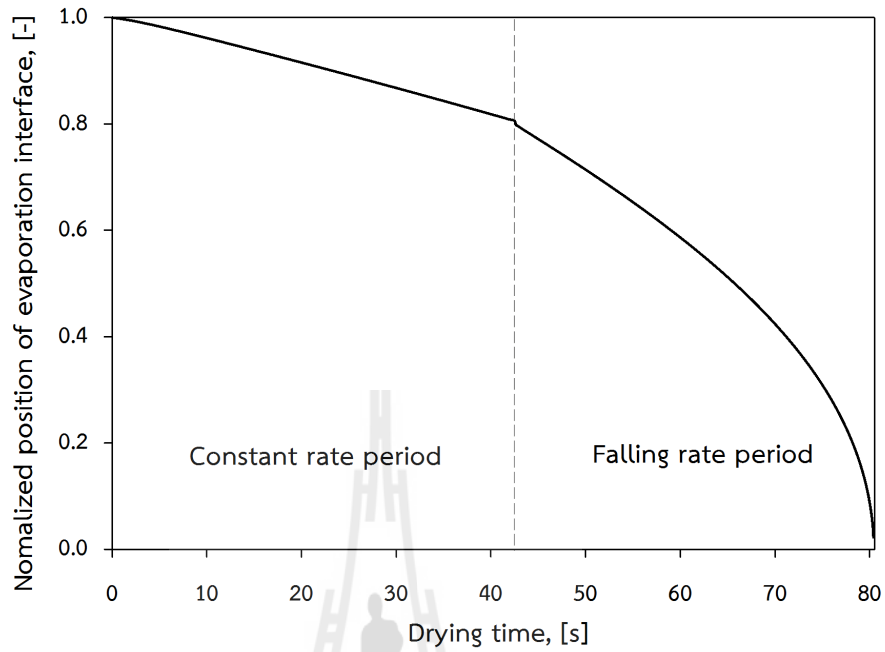

Figure 14: The movement of the evaporation interface with drying time.

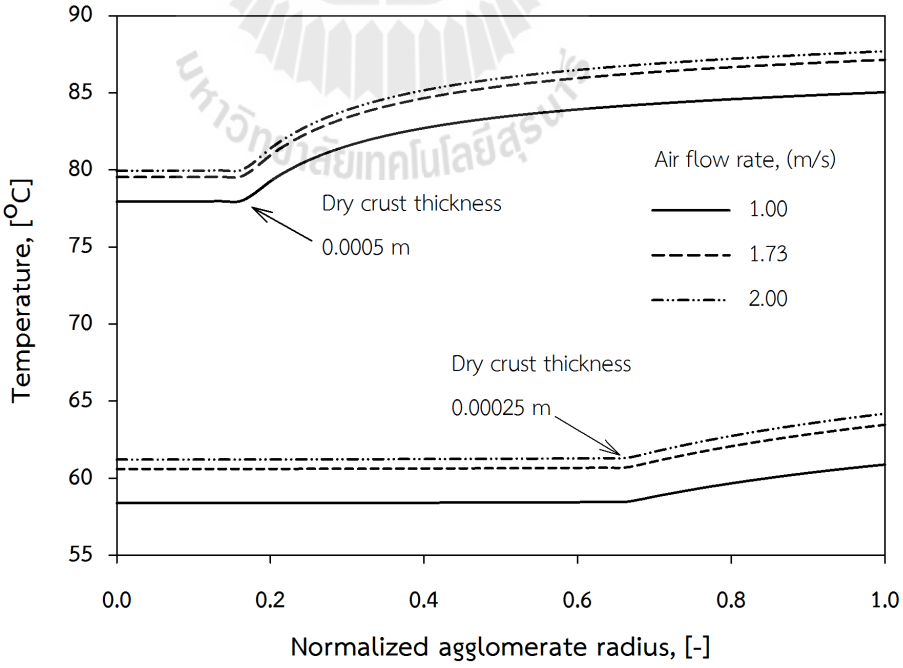

Figure 15: Temperature profiles inside the agglomerate at different air flow rates.

at high air flow rate for the same thickness of dry crust as the larger amount of heat supplied from the surface results in the acceleration of the drying rate at the evaporation interface, as shown in Fig. 16. However, no difference is observed in the concentration of water vapor at the agglomerate surface. The reduction in vapor concentration in this region at high air flow rate can be explained by enhancements of the rate of mass transfer from agglomerate surface to the bulk air as well as the rate of mass transfer in the crust layer close to the agglomerate surface due to the large value of diffusivity of water vapor at high temperature.

Figure 16 also illustrates that the large amount of water vapor is accumulated close to the evaporation interface of thick crust layer due to the enlarging mass transfer resistance.The comparison of water vapor concentration profiles at the same air flow rate reveals that the vapor concentration at specified position in the dry crust is low in the agglomerate dried for long time corresponding to the thick crust layer owing to the enhancement of vapor diffusivity at high temperature.

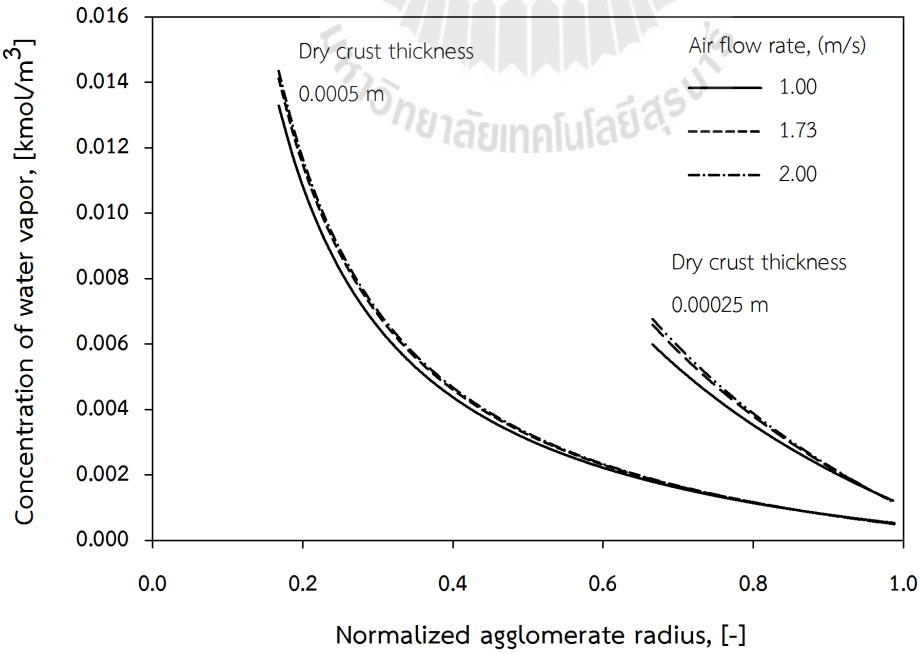

Figure 16: Concentration of water vapor inside the agglomerate at different air flow rates.

Figure 17 confirms that the drying of agglomerated nanoparticles in the falling rate period occurs more quickly at high air flow rate as a result of the intensification of convective heat transfer from the bulk air to the agglomerate surface and mass transfer in the opposite direction.

Figure 18 shows the variation of dimensionless droplet weight with respect to drying time for various drying air temperatures. The result confirms that the droplet weight reduces more rapidly at higher air temperature because of the higher drying rate at those conditions. Thus, the greater flow rate and temperature of the drying air result in the acceleration of external heat and mass transfer which in turn entails enhancement of mass and heat transfer inside the agglomerate.

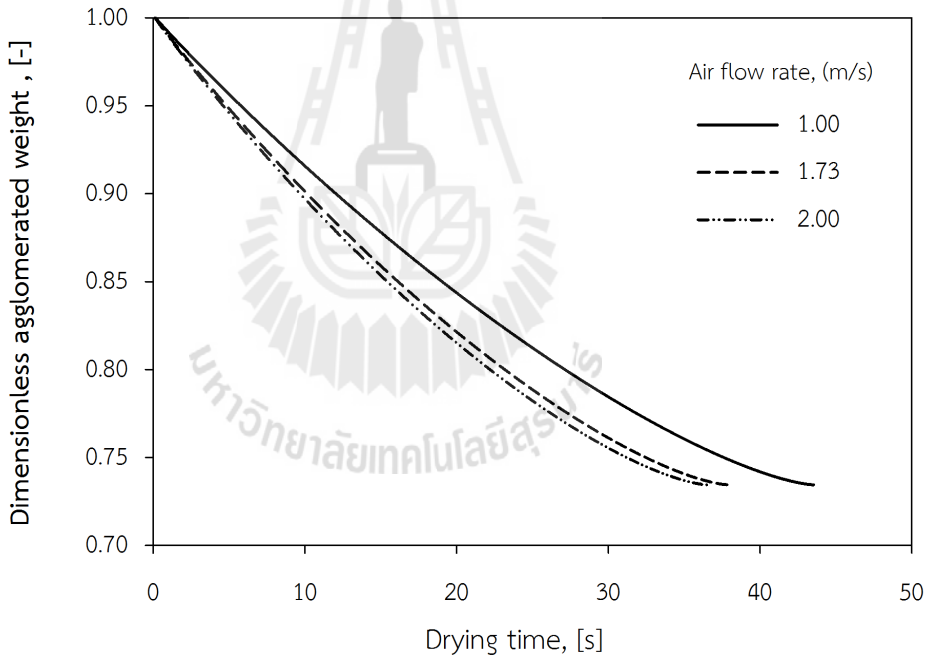

Figure 17: Dimensionless weight of the agglomerate dried at various air flow rates.

In this study, the agglomerated particles of different porosities are obtained by spray drying of the slurry of constant concentration. Hence, the amount of solid in the droplet is kept constant. Thus, the loose agglomerates are of larger sizes than the ones of lower porosities. The rate of external heat and mass transfer is high in the case of the tight agglomerate of small size. The heat transfer in the crust layer of this

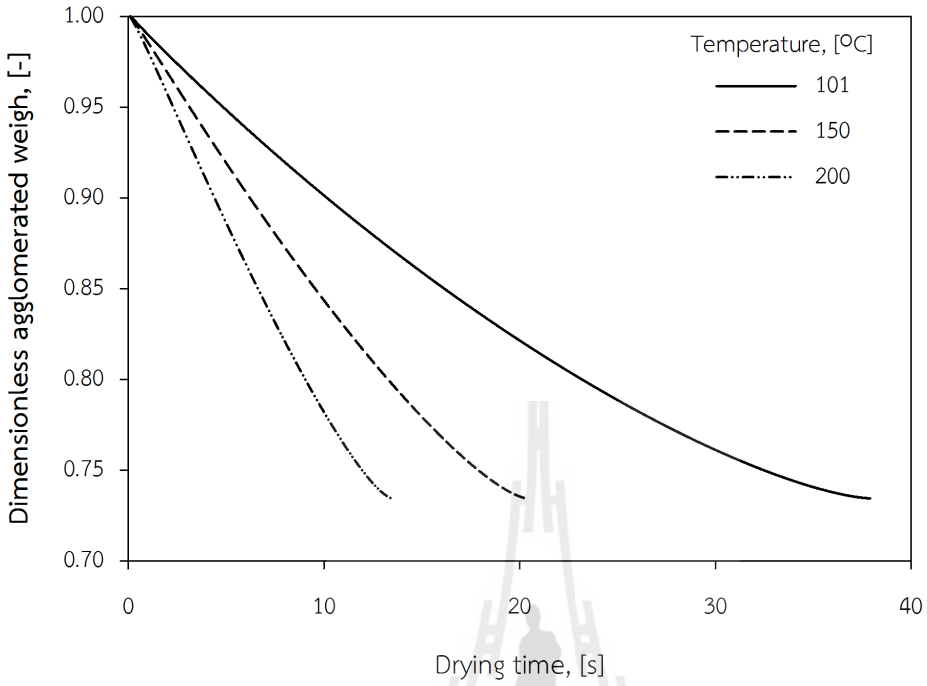

Figure 18: Dimensionless weight of the agglomerate dried at various air temperatures.

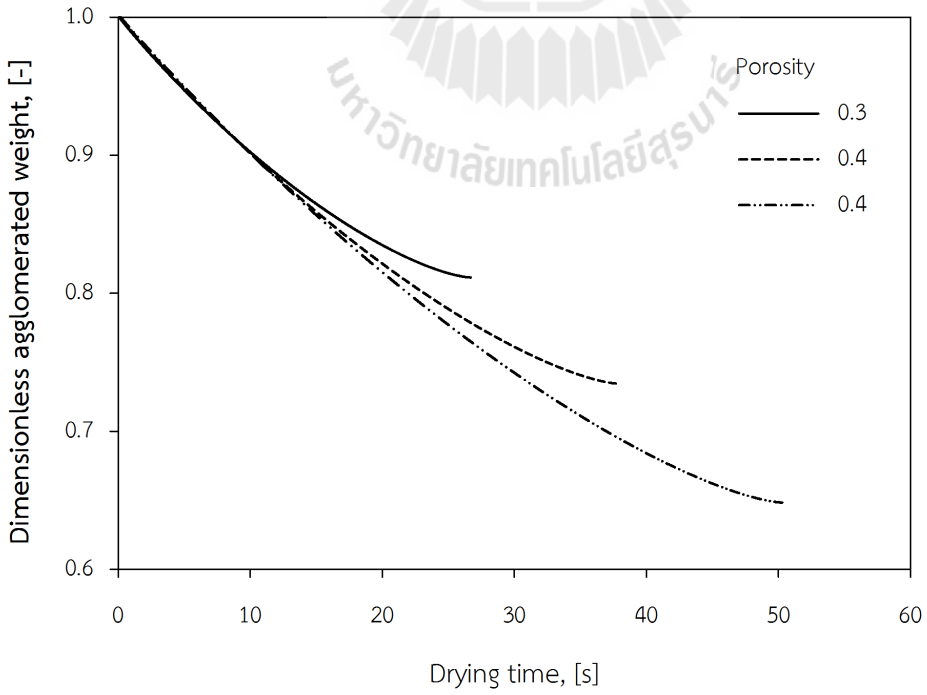

Figure 19: Dimensionless weight of the agglomerate of various porosities.

agglomerate is also high due to the high value of solid heat conductivity. However, the rate of internal mass transfer is balanced by the larger value of the effective diffusivity in loose agglomerate by Eq. (112) and the larger value of water vapour diffusivity at high temperature for tight agglomerates by Eq. (113). As a result, the drying time of the agglomerate of lower porosity is shorter in the falling rate period in comparison with loose agglomerate, as indicated in Fig. 19.

5.1.3 Effect of process parameters

Table 6 summarizes the standard value of process and agglomerate structural parameters used in the present analysis.

Table 6: Standard value of process and agglomerate structural parameters

Parameter	Value
Air temperature	200°C
Air flow rate	1 m/s
Slurry concentration	30 %
Initial droplet temperature	30°C
Agglomerate diameter	50 μm
Agglomerate porosity	0.5

- **Effect of Drying Air Temperature**

To study the effect of air temperature on drying kinetics of the slurry droplet, the air temperature was varied from 110 to 350°C while other operating parameters were set at standard conditions.

The drying time decreases, but the average and surface droplet temperatures increase at high air temperature, as illustrated in Fig. 20. The drying rate rises with air temperature due to increase of convective heat transfer and decrease of latent heat of vaporization. The rate of heat transfer from drying air to the droplet surface enhances at higher temperature, as illustrated in Fig. 21 by the higher heat transfer coefficient,

resulting in the increase of the surface and average temperatures.

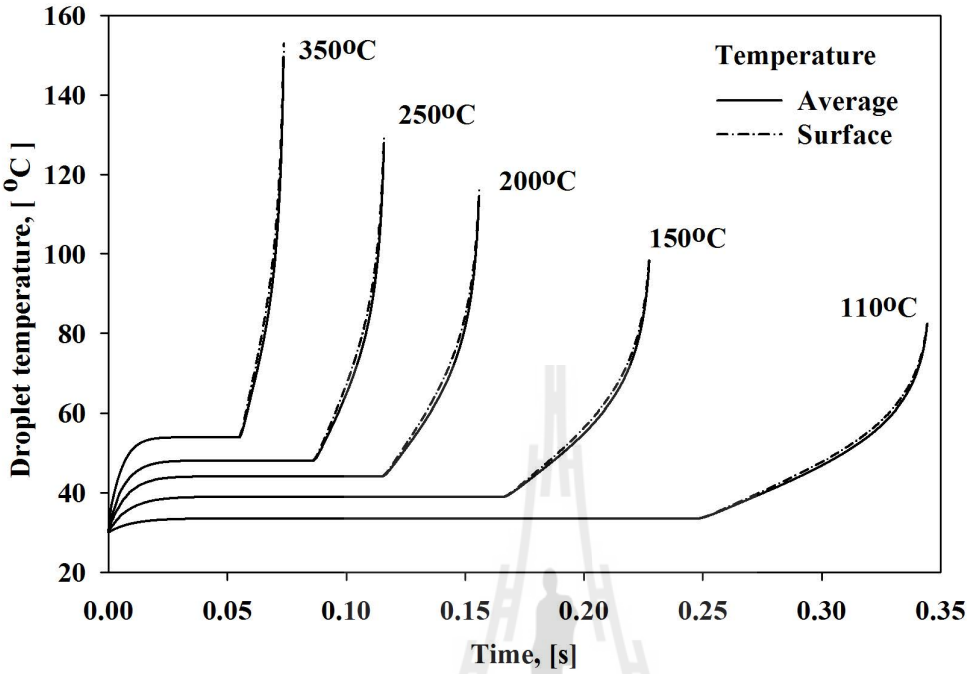

Figure 20: Average and surface temperatures of the droplet dried at various air temperatures

The surface and average droplet temperatures are identical to each other at the beginning and at the end of falling rate period for all air temperatures. However, the surface and average temperatures differ slightly in the middle of the period, as illustrated in Fig. 20. The falling rate period starts with formation of dry spots on the droplet surface while the most part of it is still covered with liquid. Therefore, the surface and average temperatures are similar at the beginning of falling rate period.

The pressure inside the droplet increases with respect to drying time as liquid vapor concentrate close to the evaporation surface at the outer boundary of wet core (Mezhericher et al. 2008), as shown in Fig. 22. This is the result of mass transfer resistance to vapor diffusion in the porous structure of solid crust. Therefore, the wet core becomes significantly hotter for longer drying time, as demonstrated in Fig. 23.

The increase of heat transfer resistance with drying time is illustrated in Fig. 23 by considering the rise of temperature difference between the droplet surface and the

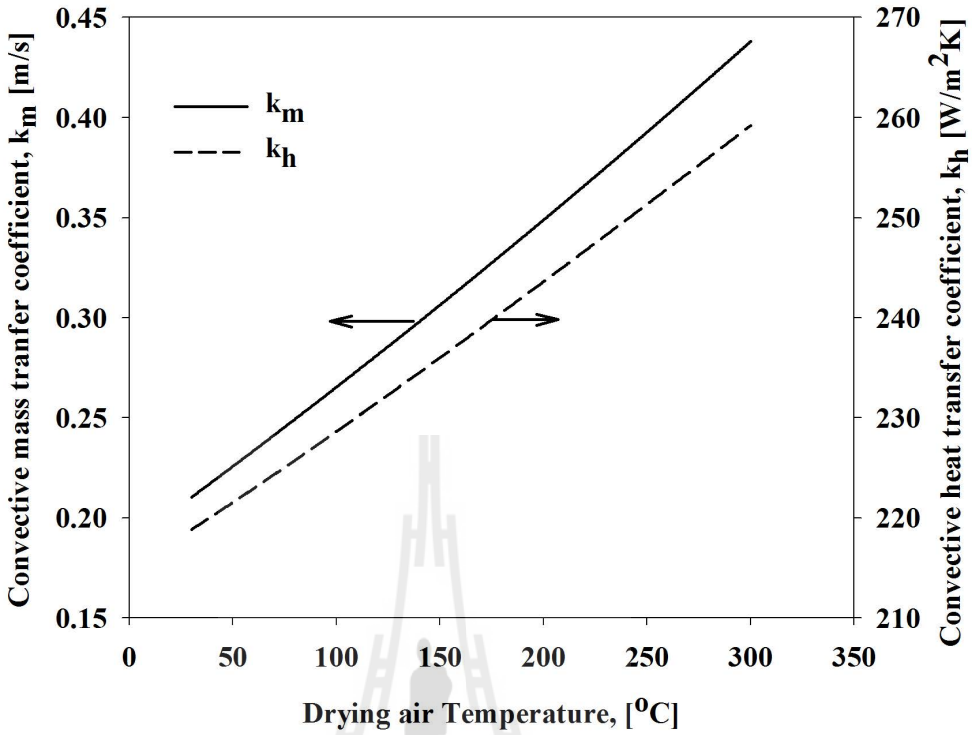

Figure 21: Variation of convective heat and mass transfer coefficients with drying air temperature

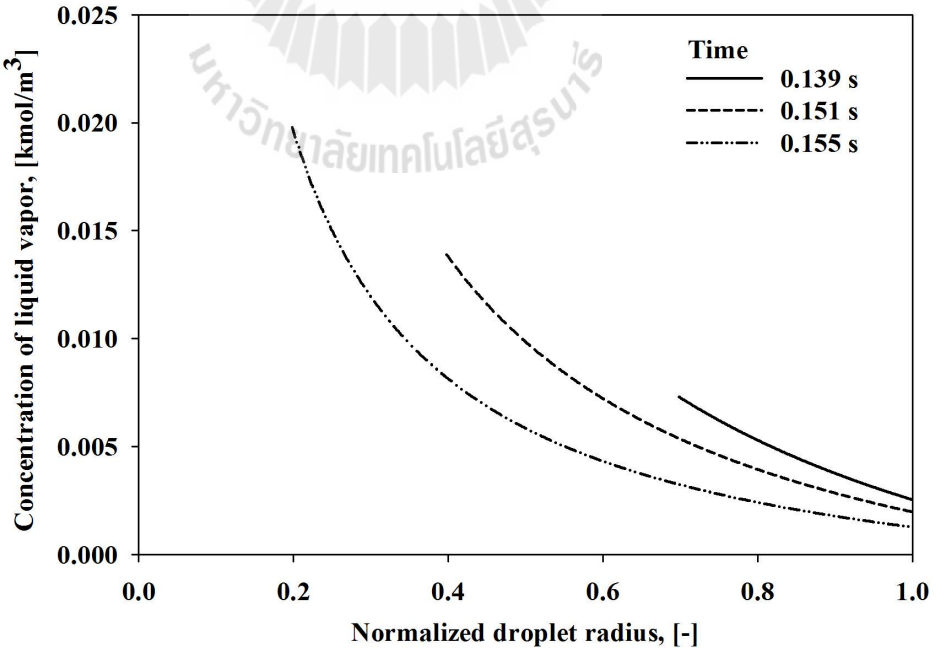

Figure 22: Vapor concentration profiles inside the droplet in falling rate period at air temperature of 200°C.

evaporation interface. In addition, the temperature profile with convex curvature is observed in the dry crust region of the droplet due to exchange of heat between liquid vapor which diffuses through pore space and the dry crust.

The surface and wet core temperatures rise according to time, yet the size of wet core diminishes, as illustrated in Fig. 23 by comparing the corresponding flat regions. As a result, the difference between surface and average temperatures increases slightly up to the point, which corresponds to the maximum temperature difference. Then the temperature difference decreases until it became negligible at the end of drying.

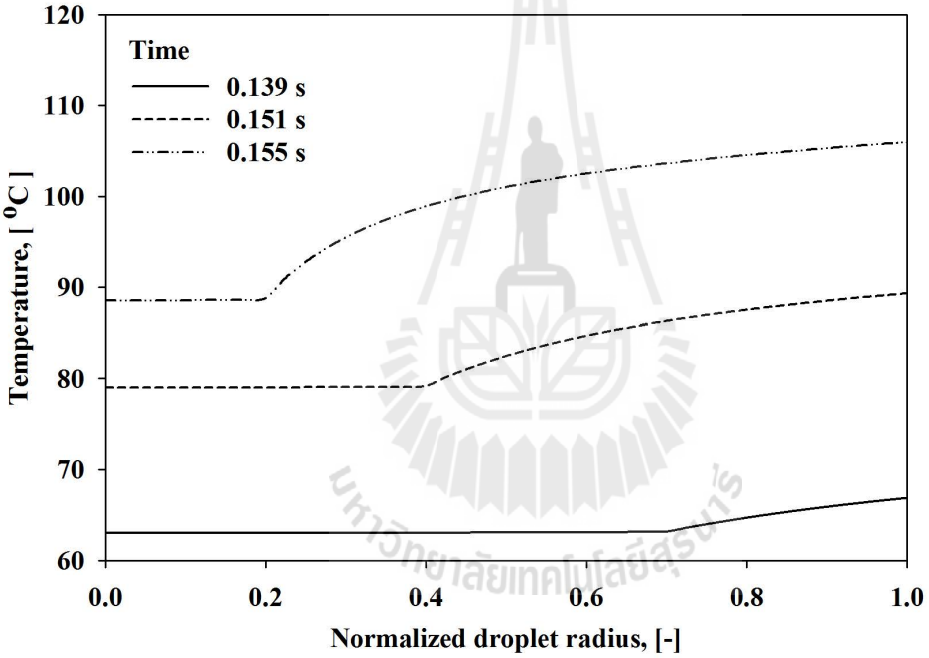

Figure 23: Temperature profiles inside the droplet in falling rate period at air temperature of 200°C.

The mass transfer resistance inside the droplet declines as diffusion of liquid vapor increases at higher drying air temperature. The rate of mass transfer from surface to drying air intensifies with decrease in air humidity. Therefore, the drying rate in the falling rate period increases at higher air temperature as the result of enhanced mass and heat transfer inside the droplet.

Figure 24 shows the variation of dimensionless droplet weight with respect to time

for various air temperatures. The result confirms that the droplet weight reduces more rapidly at higher air temperature because of the higher drying rate at those conditions.

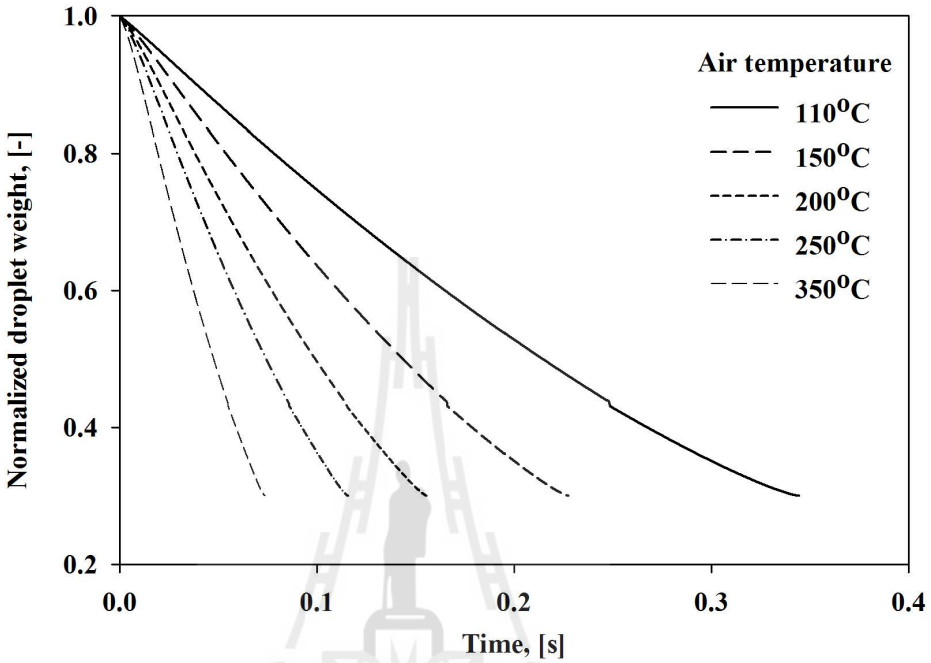

Figure 24: Dimensionless weight of the droplet dried at various air temperatures.

- **Effect of Drying Air Flow Rate**

To study the effect of air flow rate on drying kinetics of the slurry droplet, the air flow rate was varied from 0.1 to 2 m/s while other operating parameters were set at standard conditions.

Figure 25 indicates the average and surface temperatures of the droplet for various air flow rates. The drying time decreases at higher air flow rate as the boundary layer around the droplet gets thinner. As the result, the external mass and heat transfer resistances decline. Therefore, the rates of heat transfer from drying air to the droplet and mass transfer in opposite direction increase, as shown Fig. 26. This yields to the enhancement of drying rate in the constant rate period.

The rates of mass and heat transfer in the droplet increase as the concentration and temperature gradients rise in the falling rate period resulting in higher drying rate.

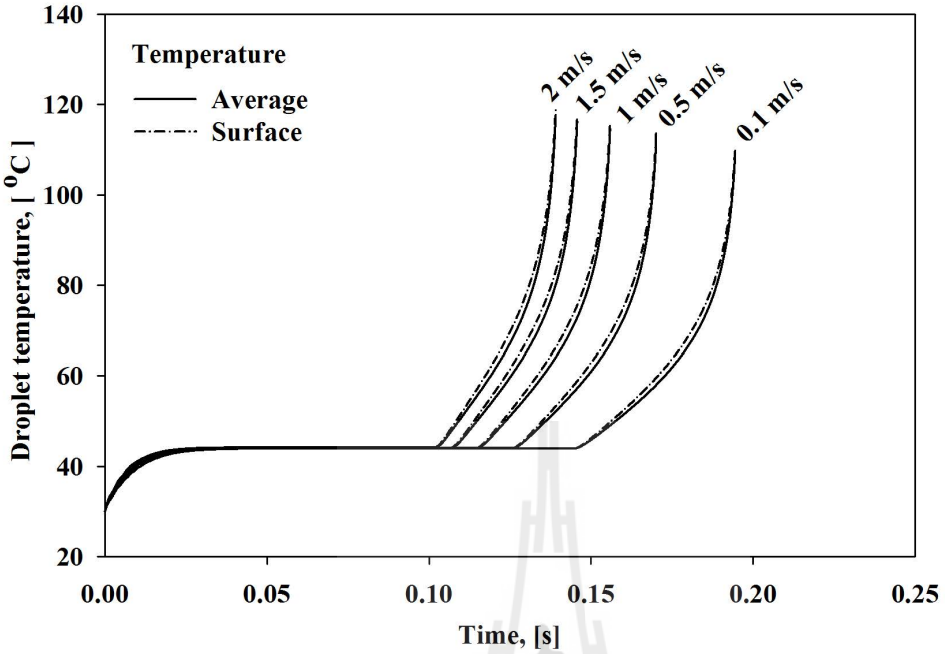

Figure 25: Average and surface temperatures of the droplet dried at various air flow rates.

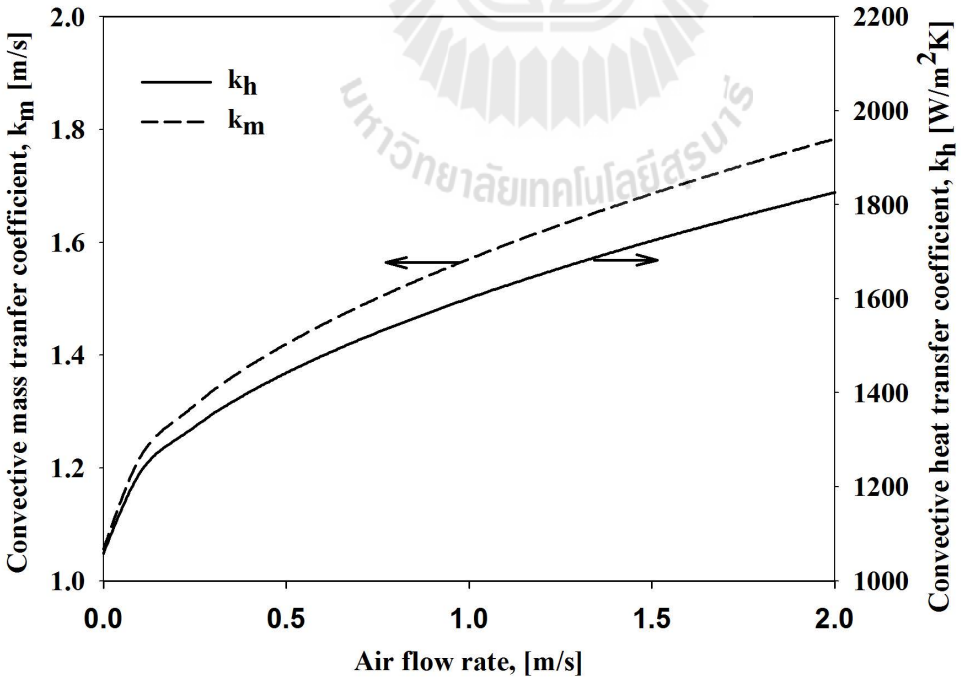

Figure 26: Variation of convective heat and mass transfer coefficients with air flow rate.

- **Effect of Slurry Concentration**

To study the effect of slurry concentration on drying kinetics of the slurry droplet, the slurry concentration was varied from 25 to 35% while other operating parameters were set at standard conditions.

In the present study, the slurry concentration was varied from 25% to 35% w/w. As the porosity and the particle diameter were both fixed, the mass of solid in the slurry was also fixed. The increase of slurry concentration corresponds to the decrease of the amount of liquid in the slurry, yielding to the reduction of free liquid section in the constant rate period. The heat and mass transfer intensify due to the decline in the slurry droplet size.

As a result, the drying rate of concentrated slurry is high in the constant rate period, as exemplified in Fig. 27 by variations of average and surface droplet temperatures with drying time.

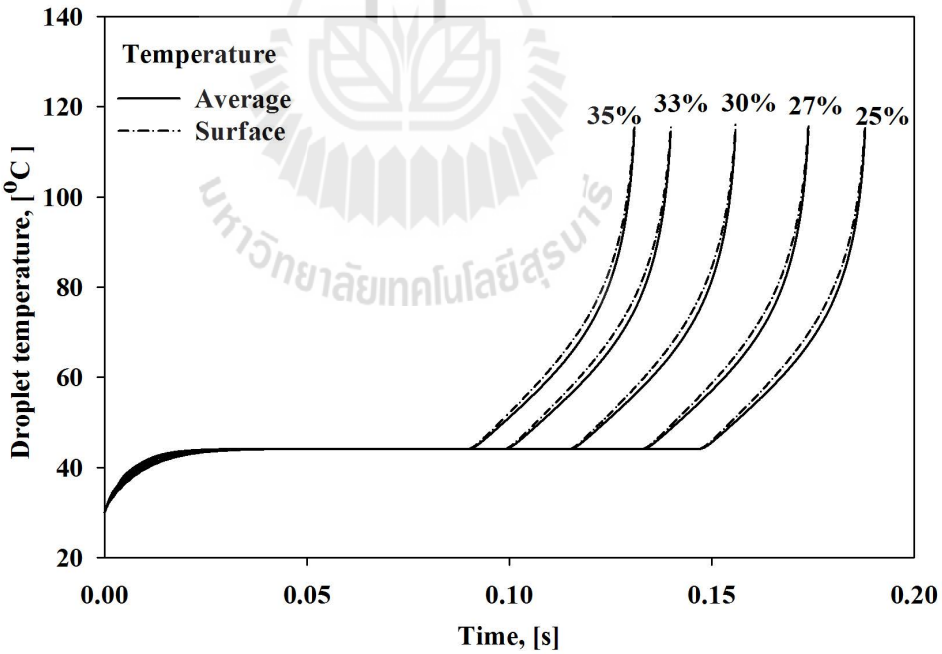

Figure 27: Average and surface temperatures of the droplet dried at various slurry concentration.

The drying rate in the falling rate period does not change with slurry concentration. The droplet size remains constant after evaporation of free liquid on the droplet sur-

face, leading to the constant external and internal heat and mass transfer resistances.

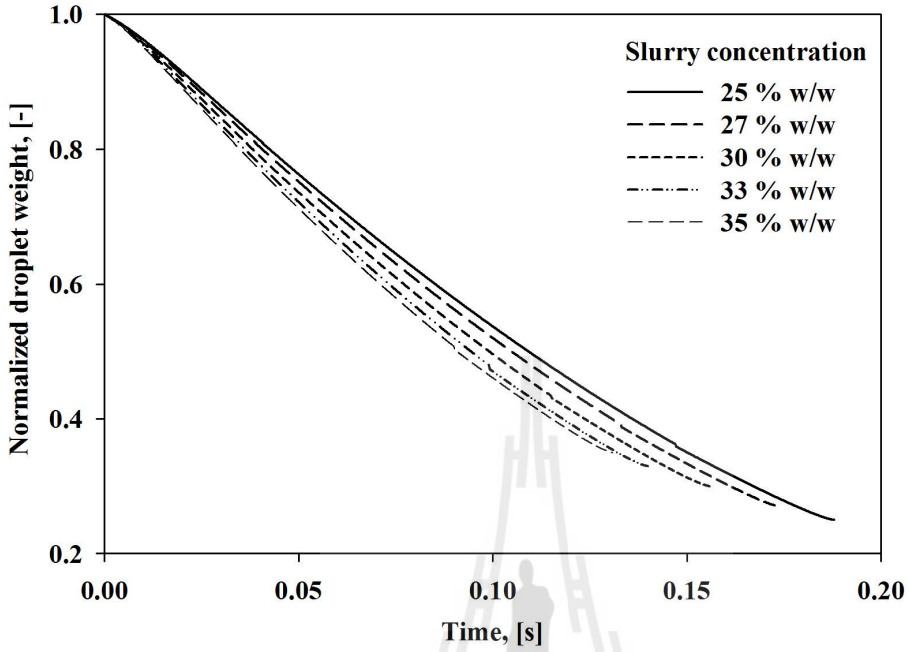

Figure 28: Dimensionless weight of the droplet dried at various slurry concentrations.

Figure 28 shows the variation of dimensionless droplet weight with respect to time. The droplet weight declines rapidly at higher slurry concentration. In addition, the normalized final weights of particles are not the same due to the difference in the initial weight of slurry droplets.

- **Effect of Initial Droplet Temperature**

The variations of droplet average and surface temperatures with time are illustrated in Fig. 29 for various initial droplet temperatures. The drying time in the constant rate period declines slightly at high initial droplet temperature due to the evaporation rate enhancement, as a result of high thermal conductivity and low density of liquid. However, the drying rate in the falling rate period does not change with initial droplet temperature as the droplet size, porosity, air temperature and air flow rate are constant in this period.

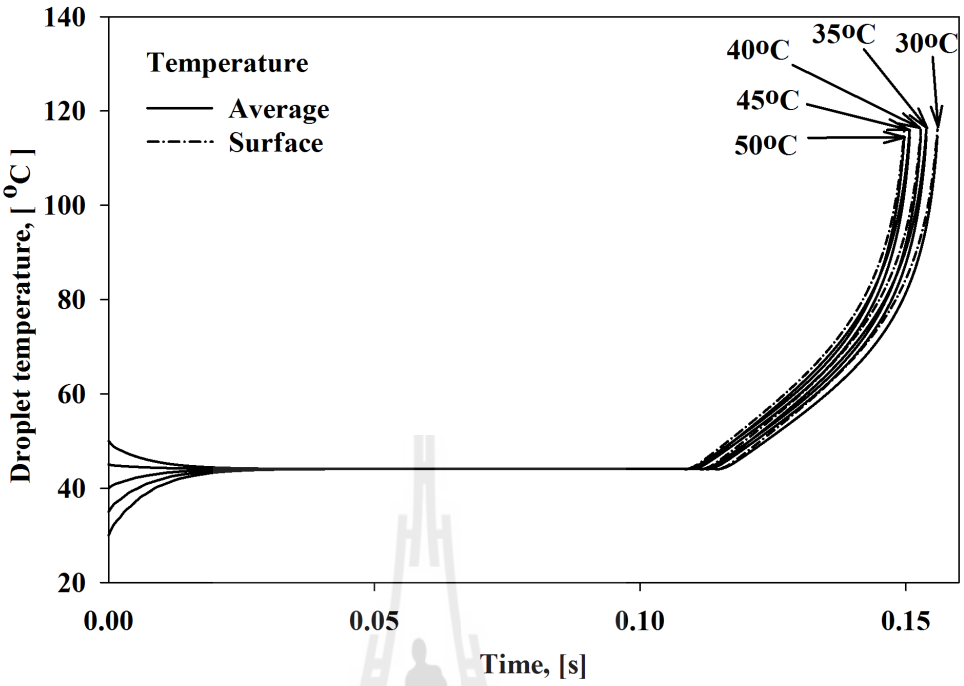

Figure 29: Average and surface temperatures of the droplet dried at various initial droplet temperatures.

5.1.4 Effect of agglomerate structural parameters

- **Effect of Particle Size**

To study the effect of particle diameter on drying kinetics of the slurry droplet, the particle diameter was varied from 10 to 100 μm corresponding to the initial droplet diameter of 15 to 147 μm.

The increase of particle diameter implies the swelling of slurry droplet since the slurry concentration is kept constant. Therefore, the convective heat and mass transfer coefficients decrease, as illustrated in Fig. 30.

Figure 31 indicates the average and surface temperatures of the droplet for different particle diameters. The drying times in the constant and falling rate periods increases for larger particles due to decline in heat supply to the droplet and mass transfer from the droplet to the drying air. Therefore, the large particles are dried more slowly than the small ones.

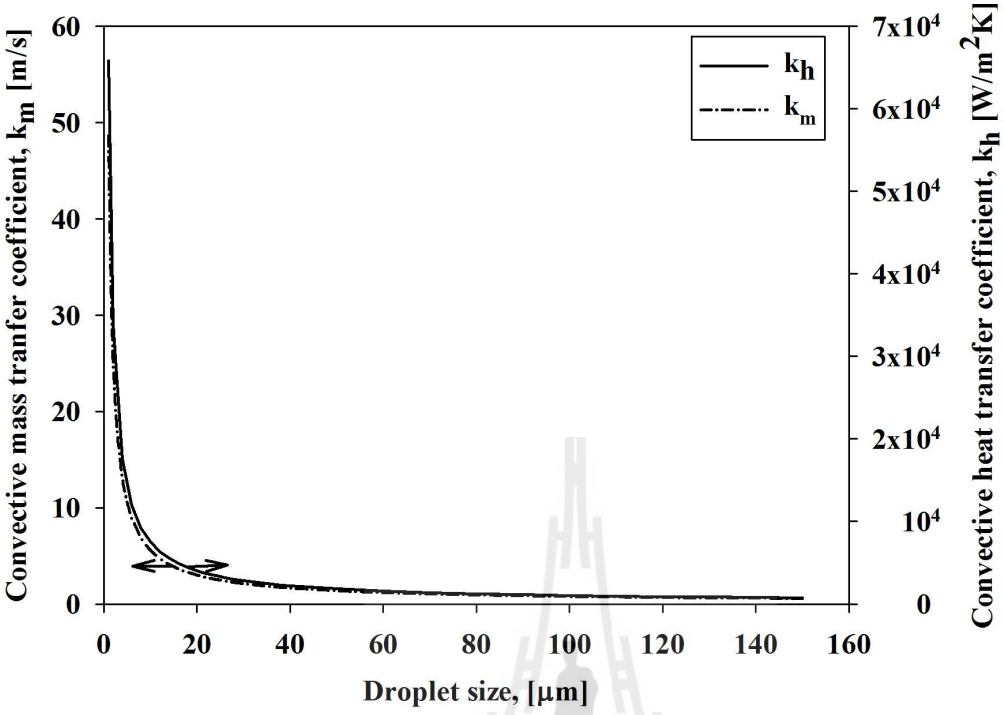

Figure 30: Variation of convective heat and mass transfer coefficients with droplet size.

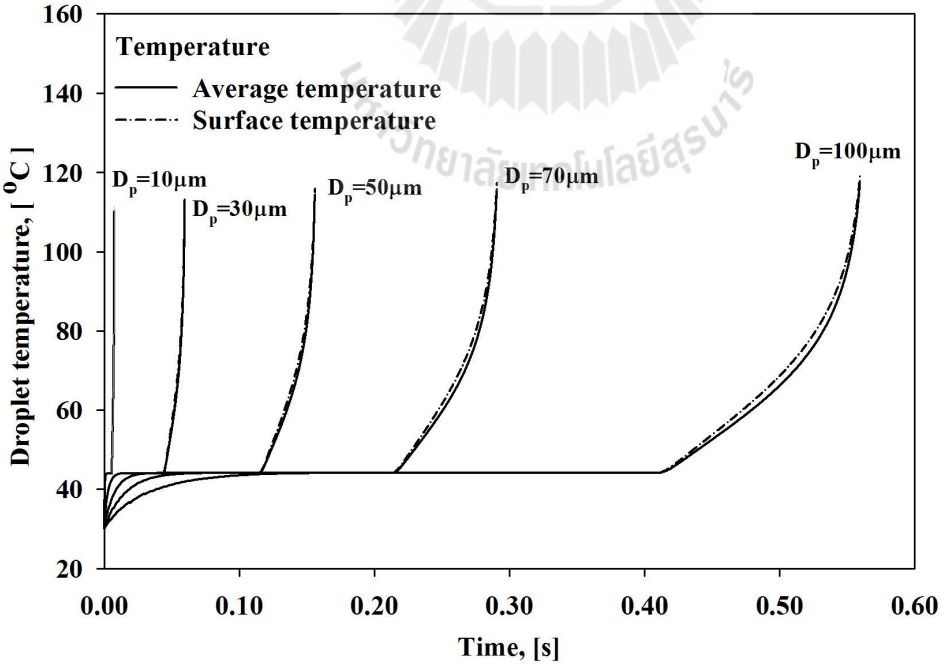

Figure 31: Average and surface temperatures of the droplet for particle of various diameters.

- **Effect of Porous Structure of Crust Layer**

The crust layers of different porosities, 0.40, 045 and 0.50, were used to study the effect of layer porous structure on the drying kinetics of slurry droplet.

The effective heat conductivity of crust layer is estimated using Woodside and Messmer (1961) model. A model Eq. (189) was derived by combining contributions of the series and parallel distributions of solid and fluid phases in the porous structure relative to the direction of heat flow (Tavman,1996).

$$k_{cr} = \frac{a \cdot k_s \cdot k_f}{k_s \cdot (1-d) + d \cdot k_f} + c \cdot k_f, \tag{189}$$

where $c = \varepsilon - 0.03$, $a = 1 - c$ and $d = (1 - \varepsilon)/a$. Here, k_f and k_s are the heat conductivities of fluid and solid phases, respectively.

Using Archie's (1942) empirical equation, the effective diffusivity is evaluated as

$$D_{cr} = D_{wv} \cdot \varepsilon^m, \tag{190}$$

where the exponent m varied between 1.8 and 2.0. The value of m was set at 1.9 in our simulation.

The diffusivity of water vapor in air, D_{wv}, is a function of temperature (Dalmaz et al., 2007)

$$D_{wv} = 0.220 \times 10^{-4} (T/273.15)^{1.75} \tag{191}$$

The decrease of droplet weight with drying time is illustrated in Fig. 32 for droplets of various porosities. The weight is normalized by the droplet weight at the beginning of the falling rate period and the starting point of the drying time calculation also defaults to the beginning of this period. The size and final moisture content are chosen to be the same for droplets of various porosities as they are usually specified by the process requirements.

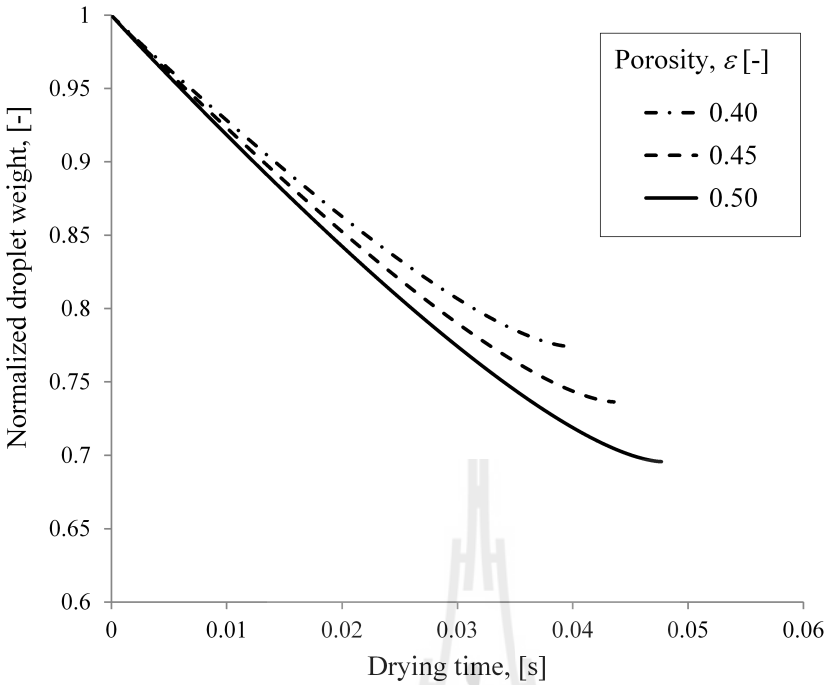

Figure 32: Variation of droplet weight with drying time.

The loose droplet of high porosity contains large amount of water at the beginning of the falling rate period when water fills all spaces in the droplet not occupied by solid. At the same time, the amount of water in the loose droplet is low at the end of drying to satisfy the final moisture content. As a result, the longer time is required for drying the loose droplet in comparison with the dense one as the larger amount of water to be evaporated from the loose droplet during the falling rate period.

The drying rate decreases with the progress of drying owing to the decline in the rates of heat transfer from the droplet outer surface to the evaporation interface and the mass transfer of water vapor in opposite direction as a result of the growing crust layer, as shown in Fig. 33.

The thicker crust layer is formed in the dense droplet than in the loose one for the same drying time. This can be attributed to the enhanced rate of heat transfer by conduction in the crust layer as confirmed by the higher value of effective heat conductivity by Eq. (189), as illustrated in Fig. 34.

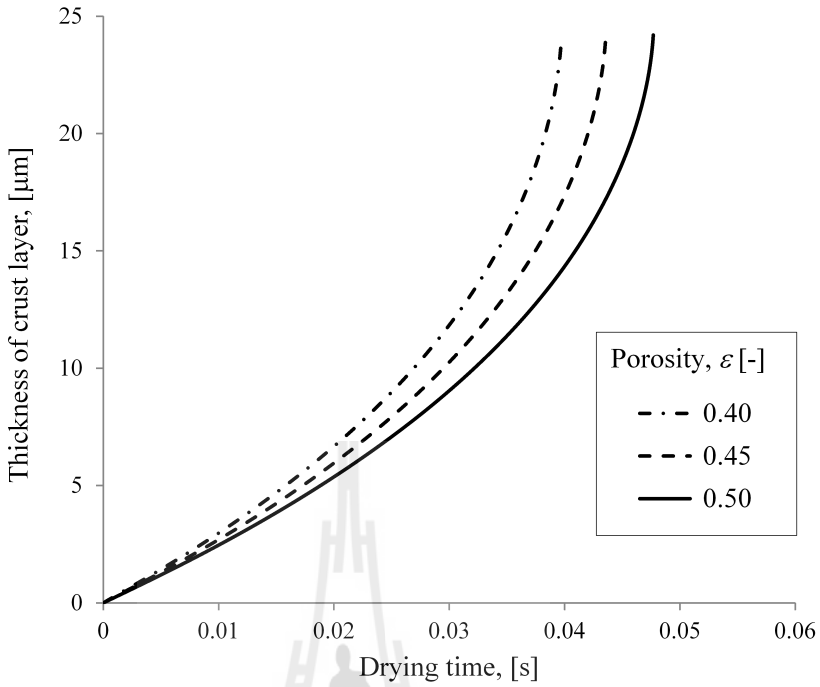

Figure 33: Thickness of crust layer as function of drying time.

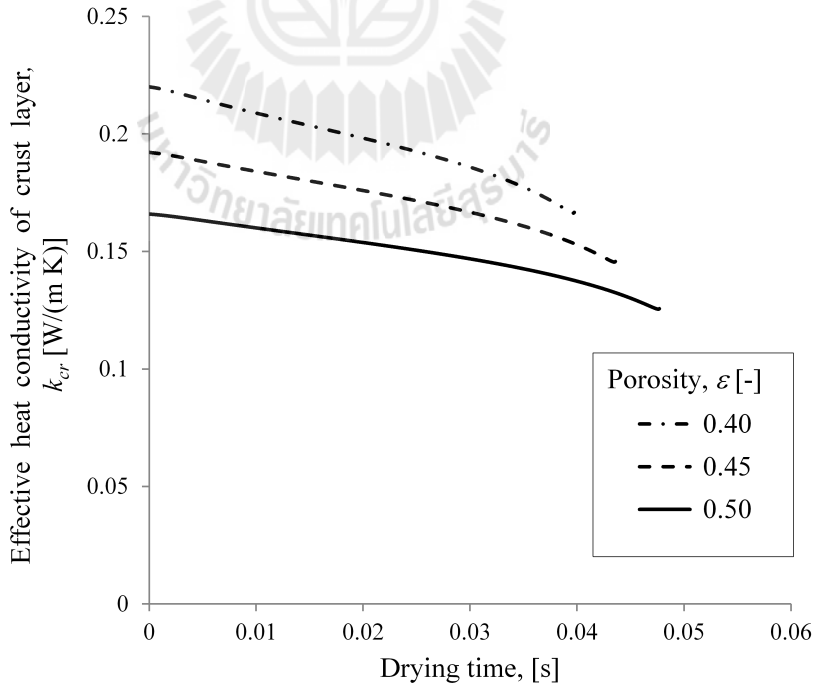

Figure 34: Variation of effective conductivity of crust layers of various porosities with drying time.

The increase of droplet average temperature with drying time is shown in Fig. 35. The average temperature of dense droplet is higher than that of loose one due to the greater effective heat conductivity of thicker crust layer which can be ascribed to the larger amount of solid phase of high conductivity.

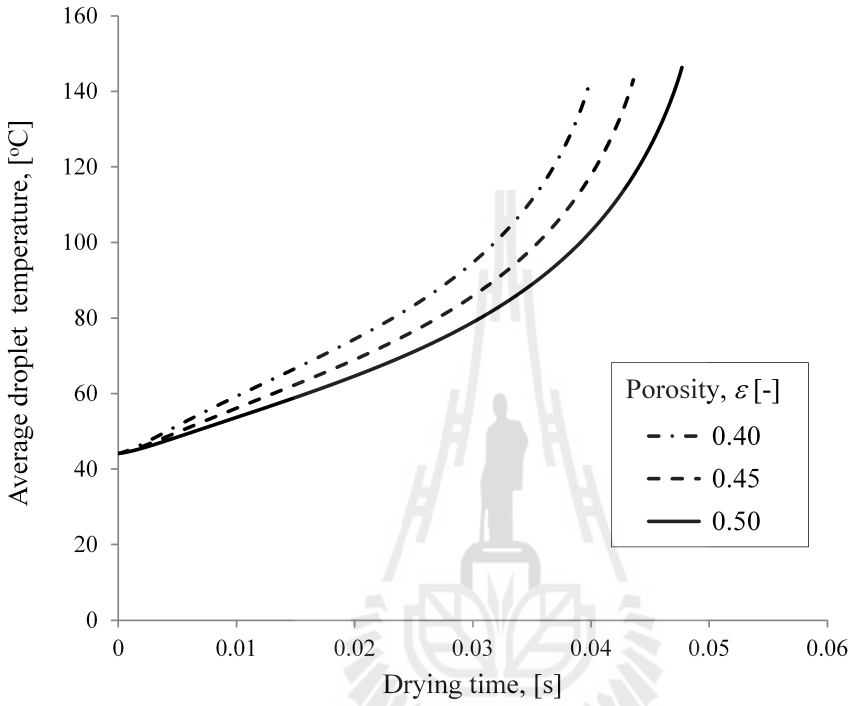

Figure 35: Variation of droplet average temperature with drying time.

The temperature distributions in the radial direction of droplets of various porosities are illustrated in Fig. 36. These profiles are evaluated at different drying times corresponding to the same position of evaporation interface. The temperature of core region only slightly increases in the radial inward direction. However, there is a significant temperature gradient in the crust region due to the heat transfer resistance of porous layer. The heat supply to the core-crust interface of high porosity droplet is limited by the low effective heat conductivity of crust layer resulting in the low temperature at the evaporation interface.

The distributions of water vapor concentration in the radial direction of crust layer are illustrated in Fig. 37 for droplets of various porosities. The vapor concentration is

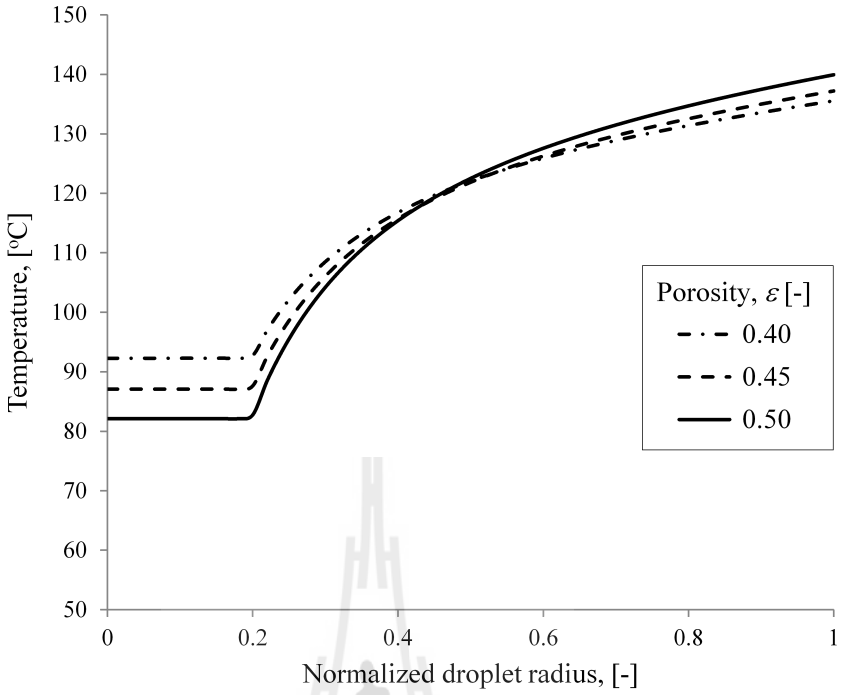

Figure 36: Temperature distribution in the droplet.

lower in the crust region of the loose droplet in comparison with the dense one as less vapor produces at the evaporation interface of loose droplet due to the low interface temperature. The generated water vapor quickly diffuses to the outer droplet surface through the large pore spaces of the high porosity droplet. This is confirmed by the enhanced value of effective diffusivity in Fig. 38, in spite of the slightly lower coefficient of molecular diffusion at low temperature by Eq. (191). The effective diffusivity of water vapor in the porous space of crust layer increases with drying time as the temperature rises in the layer by Eq. (190), as illustrated in Figs. 35 and 38.

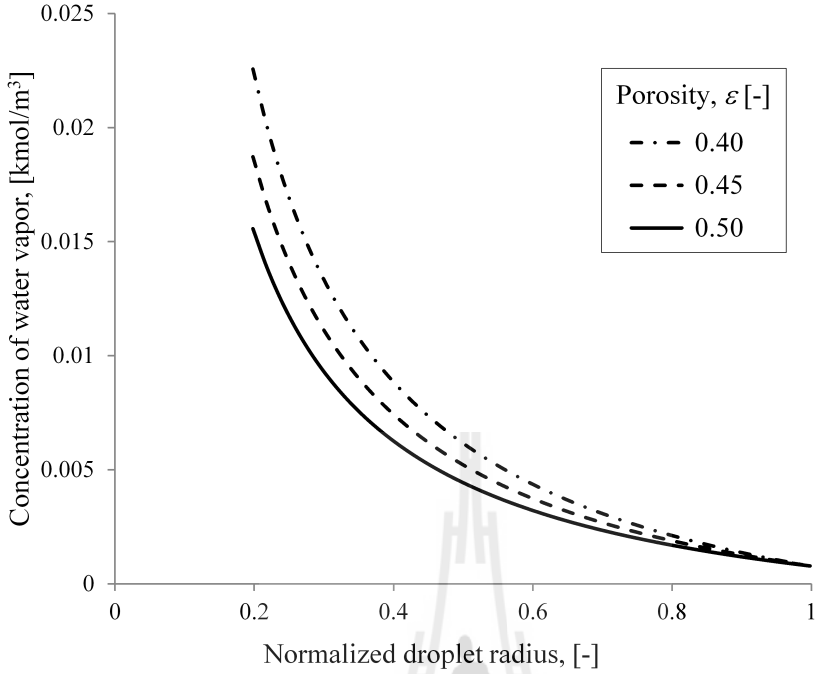

Figure 37: Distribution of concentration of water vapor in the crust layer.

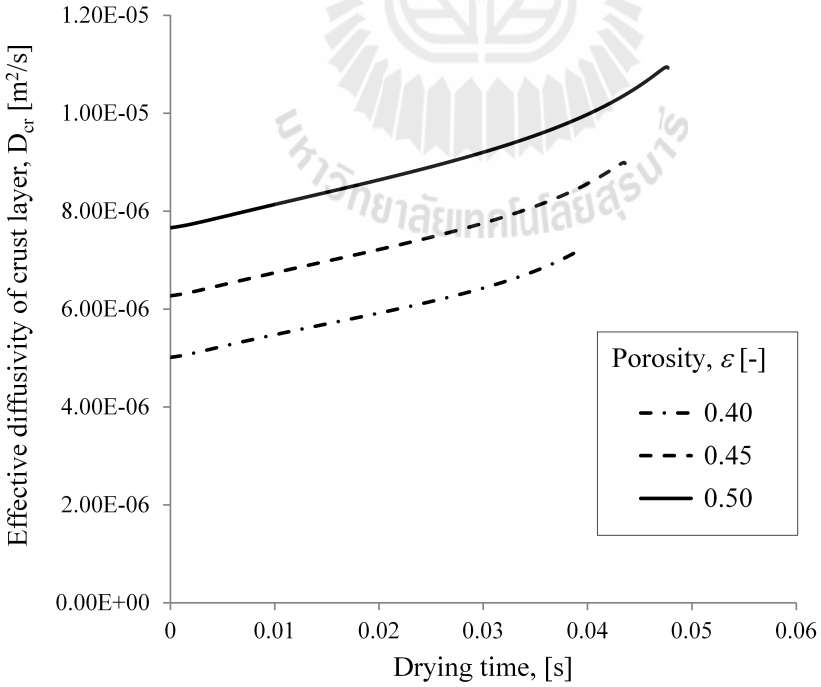

Figure 38: Variation of effective diffusivity of crust layers of various porosities with drying time.

5.2 Analysis of slurry drying in industrial spray dryer

5.2.1 Simulation setup

In the present study, computer simulation was conducted on the drying behavior of a slurry droplets containing fine particles in an industrial-scale spray dryer with a chamber consisting of an upper cylindrical and a lower conical sections, as shown in Fig. 39. The chamber diameter is 2.215 m, the height of the cylindrical section is 2.005 m and the total height of the dryer is 3.730 m.

The dryer is equipped with a centrifugal pressure nozzle with an orifice of diameter of 0.000711 m. The droplets of uniform size are assumed to form a cone with a half angle of 38° during spraying (Kieviet, 1997). Drying gas supplied from the top of the dryer concurrently with the slurry feed is distributed uniformly in the radial direction of the dryer.

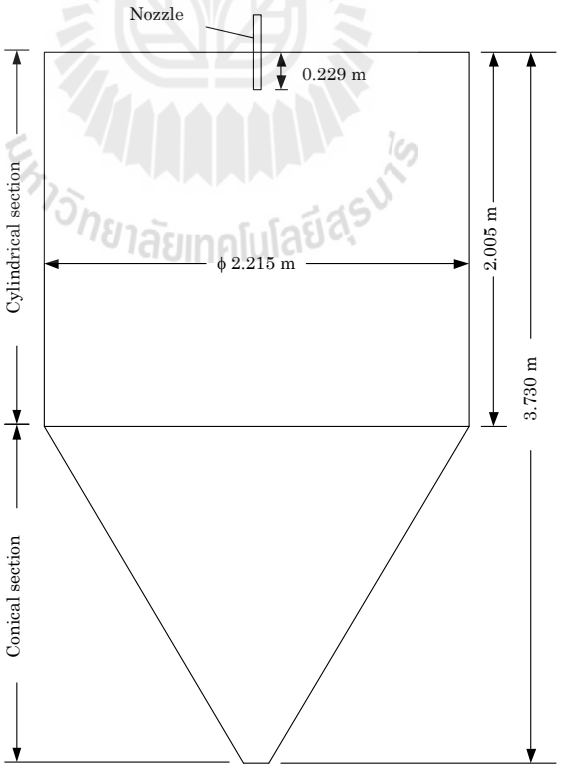

Figure 39: Illustration of spray dryer geometry.

A summary of operational conditions is given in Table 7.

Table 7: A summary of operational parameters.

Parameter	Value
Air mass flow rate	3.7 kg/s
Air temperature	110 °C
Air humidity	0.001 kg/kg
Slurry feed rate	0.08915 kg/s
Slurry concentration	30 wt%
Slurry temperature	30 °C

5.2.2 Drying mechanism of slurry droplets in spray dryer

Figure 40 illustrates the trajectories of droplets of various initial sizes in the spray dryer calculated at the same drying conditions. The axial distance is measured from the point of injection of spray in the chamber at the nozzle tip. The larger droplets travel longer distances in the axial and radial directions than the smaller ones as the drying of large droplets up to the specified final moisture content takes time due to the great amount of water to be evaporated as well as the low rate of heat and mass transfer between the drying gas and droplets.

Our simulation also confirm that the droplets as large as 110 μm in diameter can be dried in the present spray dryer without contact of moist droplets with the side wall and subsequent buildup of deposit on the wall in the upper part of the chamber close to the nozzle or on the wall of the conical section at the dryer bottom.

Figure 41 shows the variation of the average droplet temperature with (a) drying time and (b) axial distance from the nozzle. The symbols (a), (b), (c), (d) and (e) are used to illustrate the relationship between the drying time and the drying distance of droplets in the spray dryer. The duration of the initial heating-up period of droplets is very short, as the droplets are quickly heated up from the inlet temperature up

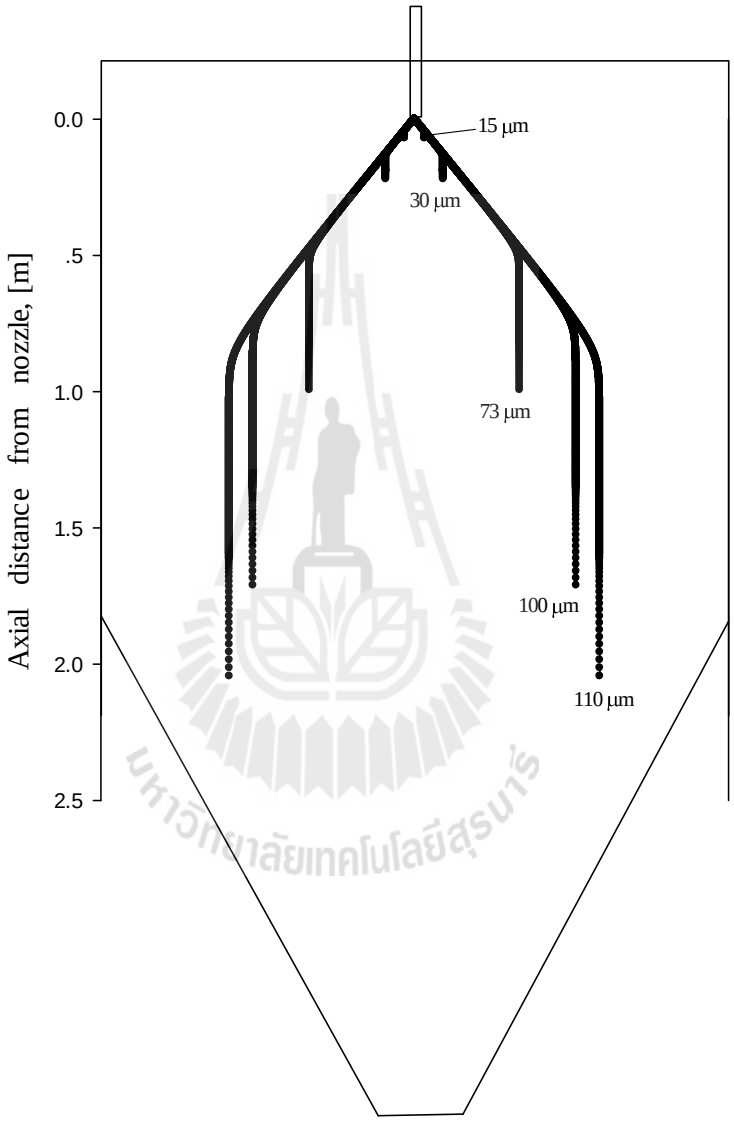

Figure 40: Trajectories of droplets of various initial sizes in the spray dryer.

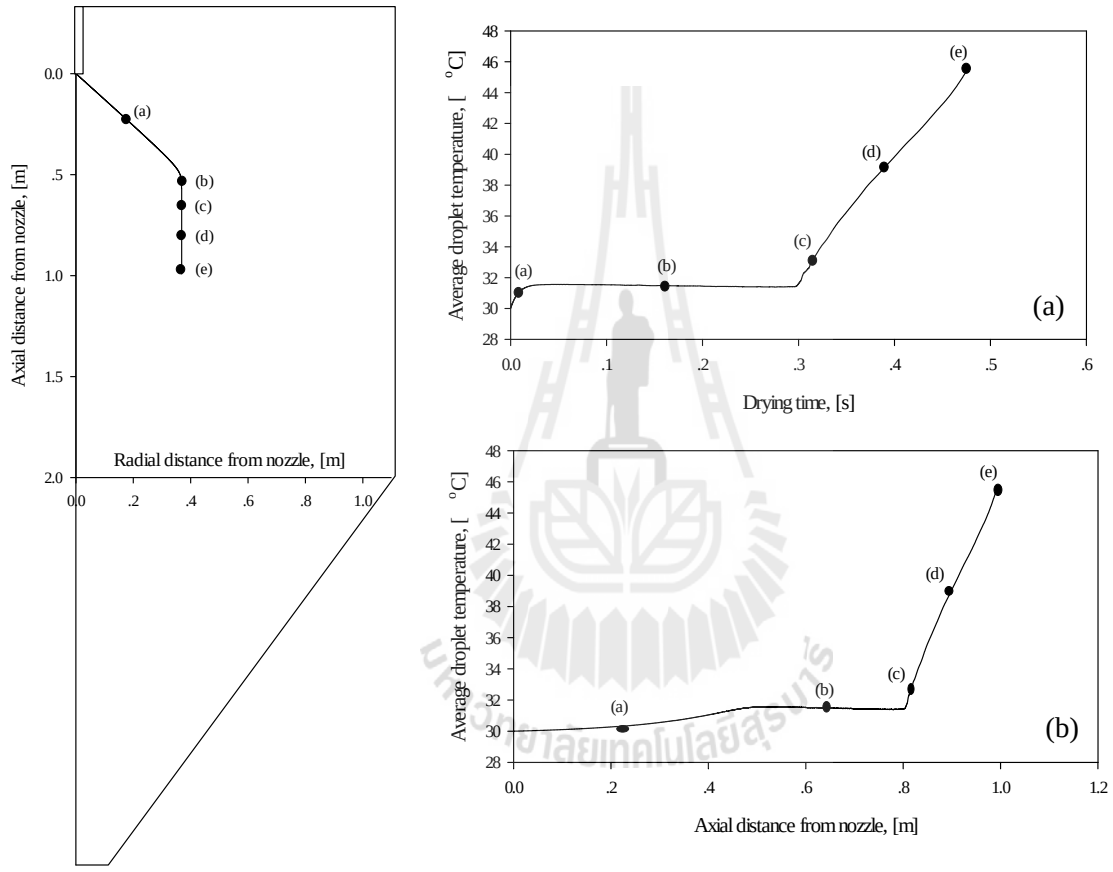

Figure 41: The variation of the average droplet temperature with (a) drying time and (b) axial distance.

to the wet bulb temperature. However, droplets will travel long distances during the initial period owing to their high injection velocity from the nozzle, as illustrated in Fig. 42.

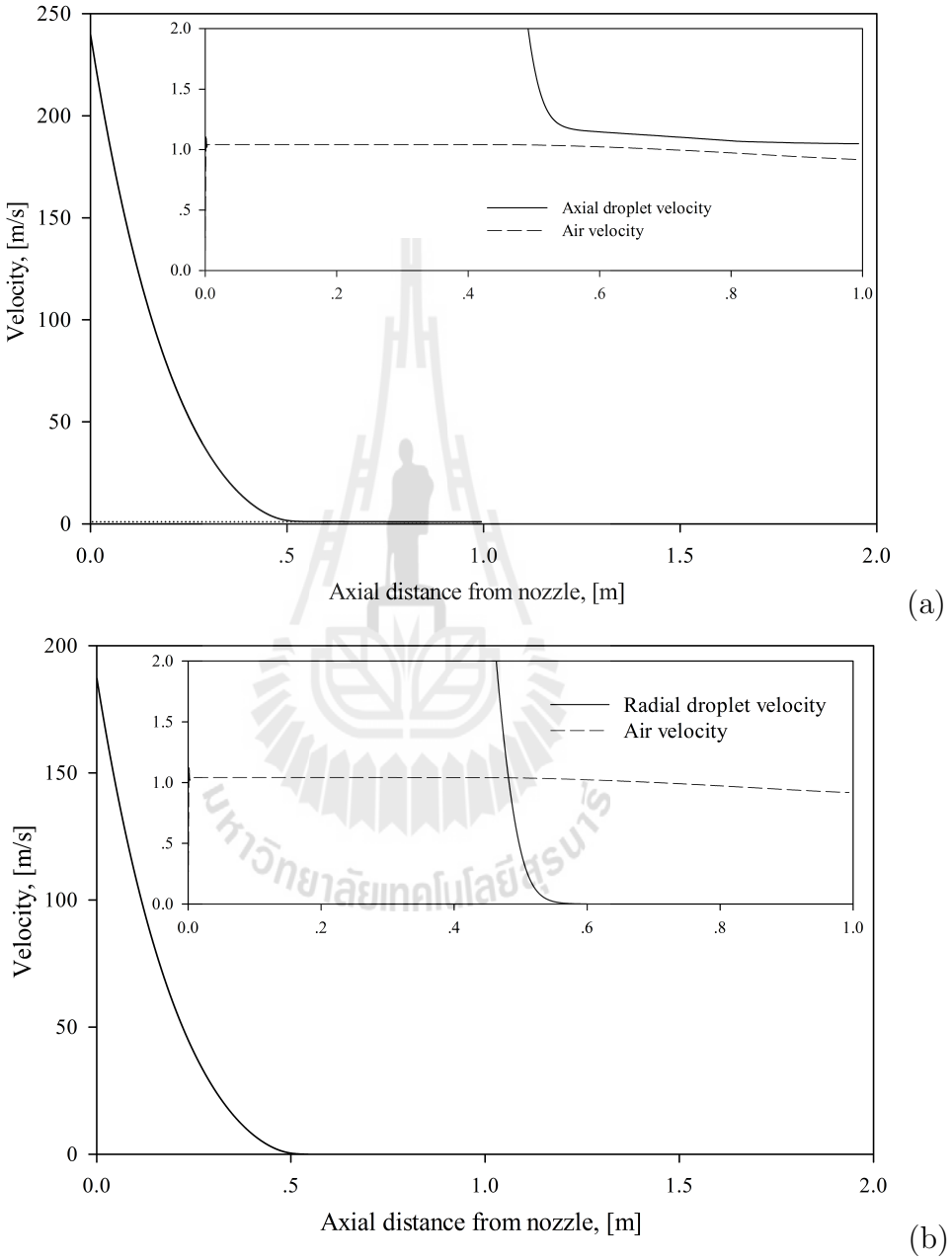

Figure 42: Velocity profiles of droplets: (a) axial and (b) radial.

After the droplet reaches its maximum radial distance, the droplet radial velocity falls to zero and the axial velocity drops to air velocity to follow the balance of forces

acting on the droplet.

As the temperature, humidity and velocity of drying air surrounding droplets alter with drying time, the drying behavior of the droplet in the dryer differ from one at constant drying conditions, even the drying mechanisms are similar.

Figure 43(a) shows the average temperature and moisture content of droplets in the cylindrical section of the spray dryer. The temperature of droplets increases rapidly up to the wet bulb temperature after they leave the nozzle due to the efficient heat transfer from the drying air. However, droplets travel around 0.5 m from the nozzle tip along the chamber height during the initial heating-up period as the initial droplet velocities are high both in the axial and radial directions, as illustrated in Fig. 43(a) and (b). Only a small amount of water is evaporated from the droplet surface in this period, as confirmed in Fig. 43(a) by the minor decline of droplet moisture content. As a result, the temperature of drying air slightly decreases and humidity increases, as shown in Fig. 43(b).

During the constant rate period, all heat supplied to the droplets by drying air is consumed on water evaporation in the droplets. The air temperature quickly declines and humidity rises in this period. The droplets travel a short distance along the chamber height because the droplet velocity is very low in comparison with the one in the heating-up period. The droplet velocity is quite close to the air velocity and the droplets have more time for heat and mass exchange with drying air.

After the constant rate period ends, the evaporation will take place inside the droplet and the drying mechanism switches to the falling rate period. The evaporation rate declines in this period, as supported by the drop in the rate of change of droplet moisture content in Fig. 43(a), since the heat and mass transfer between the evaporation interface and the drying air is hindered by the growing dry crust layer. A certain amount of heat accumulates in the crust resulting in a reduction of the heat supply to the evaporation interface. This leads to the rise of the average droplet temperature with drying time. The accumulation of water vapor in the dry crust

causes the pressure build-up in the droplet owing to the slow mass transfer through the small pores of thick dry crust.

Figure 44 illustrates the profiles of temperature and concentration of water vapor in the radial direction of the droplet at various drying times corresponding to the different drying mechanisms. The temperature profiles are nearly flat in the droplet during the initial heating-up and constant drying rate periods as there is no significant resistance to the heat transfer in the wet core containing solid particles dispersed in liquid.

In the heating-up period, the droplet temperature increases with time uniformly throughout the droplet until it reaches the wet bulb temperature. However, the droplet temperature does not change in the constant rate period as all supplied heat is consumed for evaporation of liquid at the outer droplet surface.

In the falling rate period, the temperature profile inside the droplet can be separated into two parts corresponding to the dry crust and wet core regions, as shown in Figs. 44(c), (d) and (e). The temperature profile is flat in the wet core, but the temperature declines in the radial direction of the dry crust region from the outer droplet surface to the evaporation interface due to the heat transfer resistance in the porous crust layer.

Figures 44(c), (d) and (e) also illustrate the concentration profiles of water vapor in the droplet at the beginning, in the middle and at the end of the falling rate period. The heat and mass transfer resistances in the droplet are augmented with drying time due to the growing thickness of the dry crust layer. As a result, the temperature and concentration differences rise between the outer droplet surface and the evaporation interface.

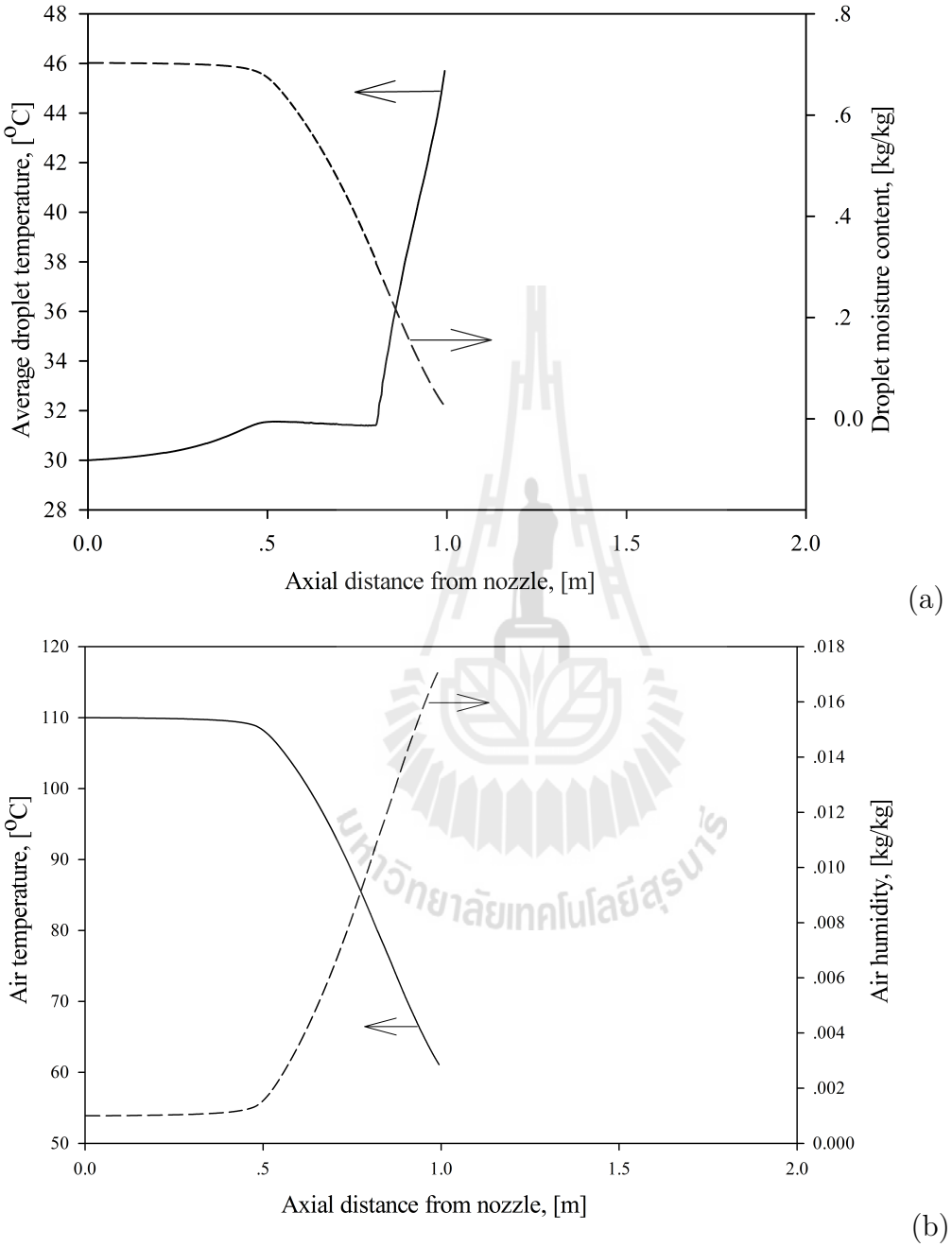

Figure 43: Drying profiles in the cylindrical section of spray dryer: (a) droplet average temperature and moisture content, (b) air temperature and humidity.

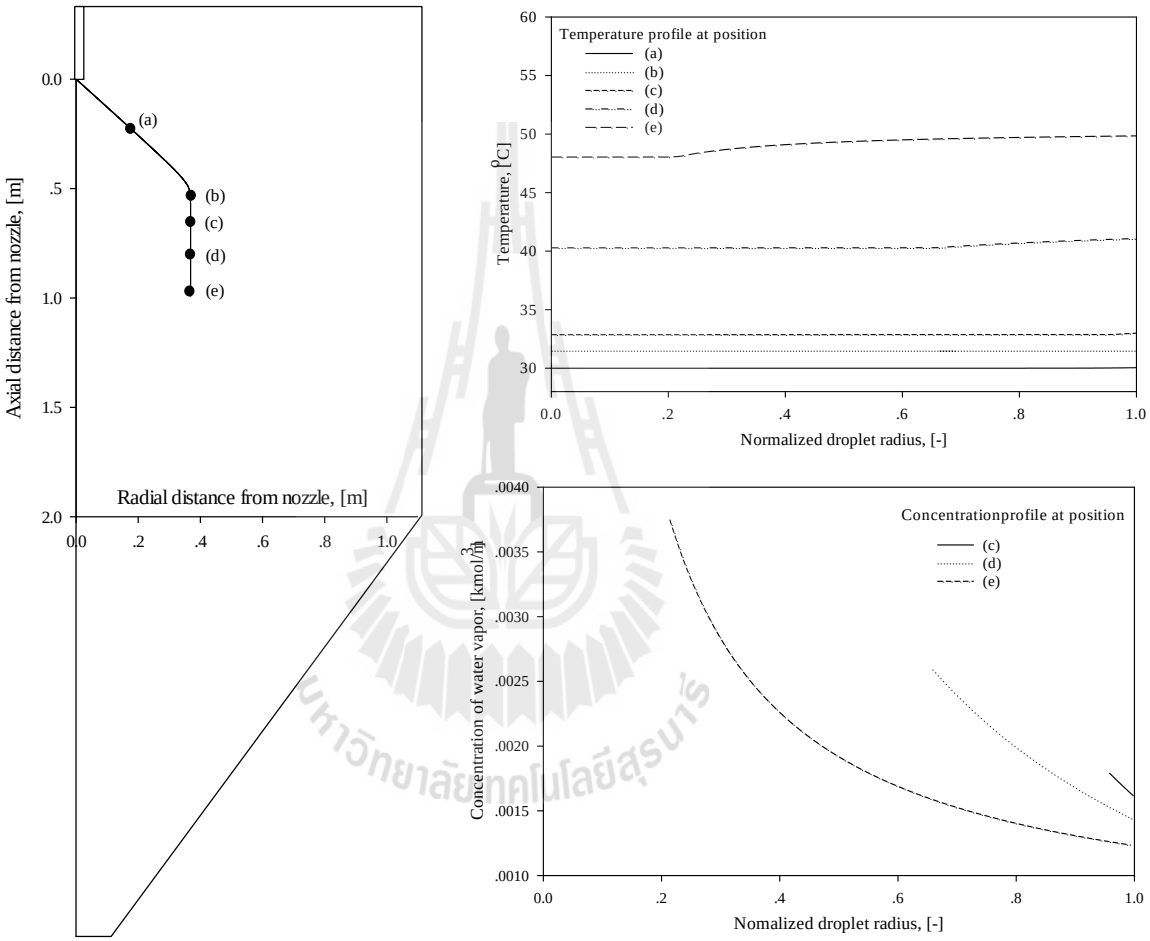

Figure 44: Temperature and concentration profiles in the droplet at various drying times.

5.2.3 Effect of air feed rate

High supply of drying air will increase the air velocity in the spray dryer, as illustrated in Fig. 45. The air velocity slightly decreases along the height of the lower part of cylindrical section of the drying chamber during the falling rate period, since the density of air increases due to the decline of air temperature.

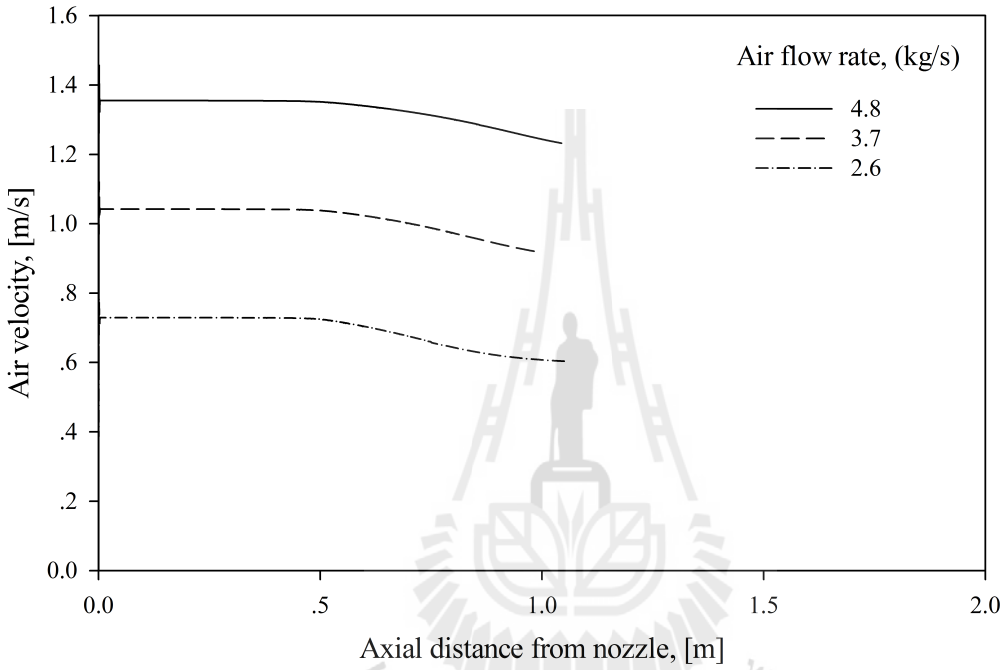

Figure 45: Air velocity profiles in the dryer at various air feed rates.

The axial velocity of droplet increases when air feed rate rises, as observed in Fig. 46 in the constant and falling rate periods, as droplets are more efficiently accelerated by high-velocity air stream.

The profiles of the droplet velocity relative to the air in the axial direction of dryer almost coincide with each other at different air feed rates, as shown in Fig. 47. Therefore, the influence of the air flow rate can be neglected on the thickness of the boundary layer around the droplet representing the resistance to convective heat and mass transfer.

After the heating-up period ends, the decreasing trends of air temperature along the axial distance of the dryer can be divided into two regions, as illustrated in Fig. 48.

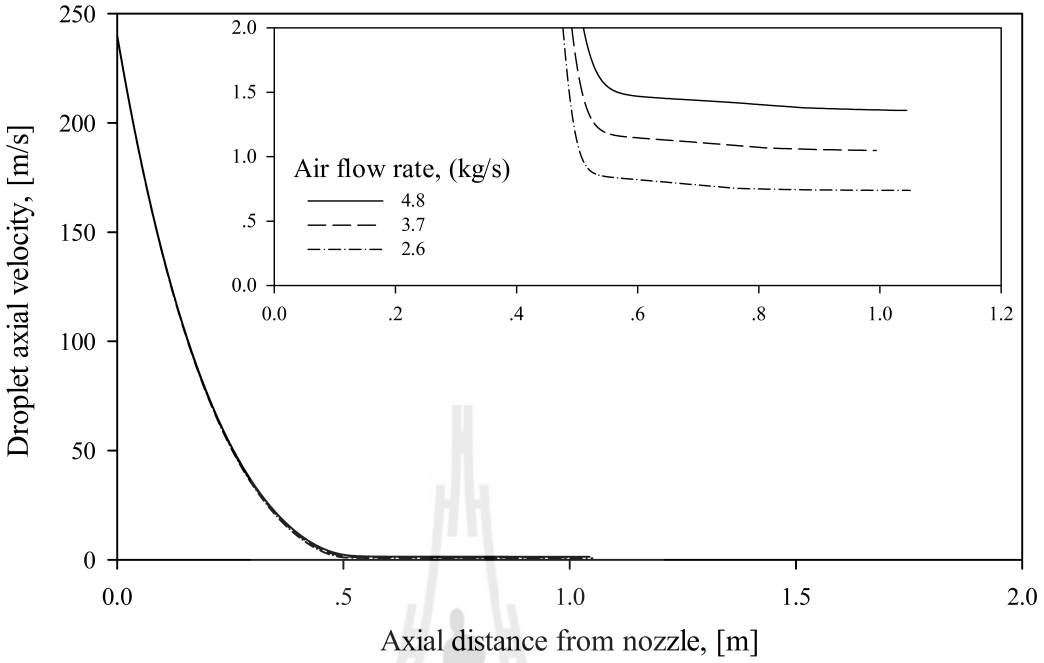

Figure 46: Profiles of axial droplet velocity in the dryer at various air feed rates.

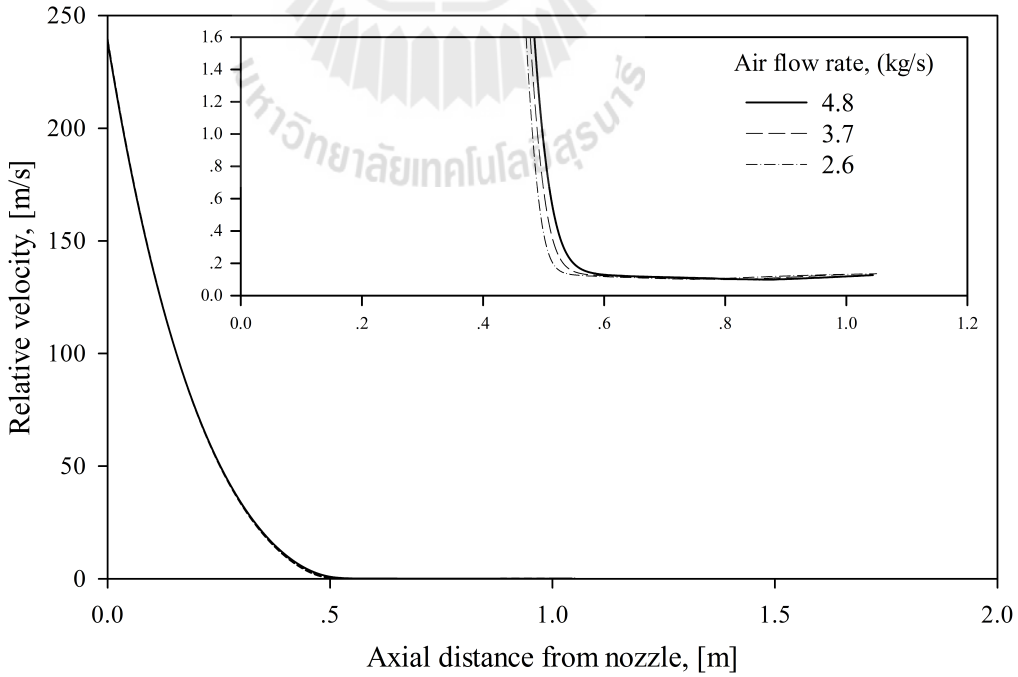

Figure 47: Profiles of relative droplet velocity in the dryer at various air feed rates.

The first region corresponds to the constant rate period. The air temperature declines more rapidly at low air feed rate than at high one due to the small amount of heat inherent in the air. In addition, the droplet drying distance is also shorter at low air feed rate owing to the long time available for heat and mass exchange between air and droplets at low droplet velocity.

The second region covers the falling rate period. Contrary to the trends in the first region, the air temperature more slowly decreases at low air feed rate than at high one, as illustrated in Fig. 48.

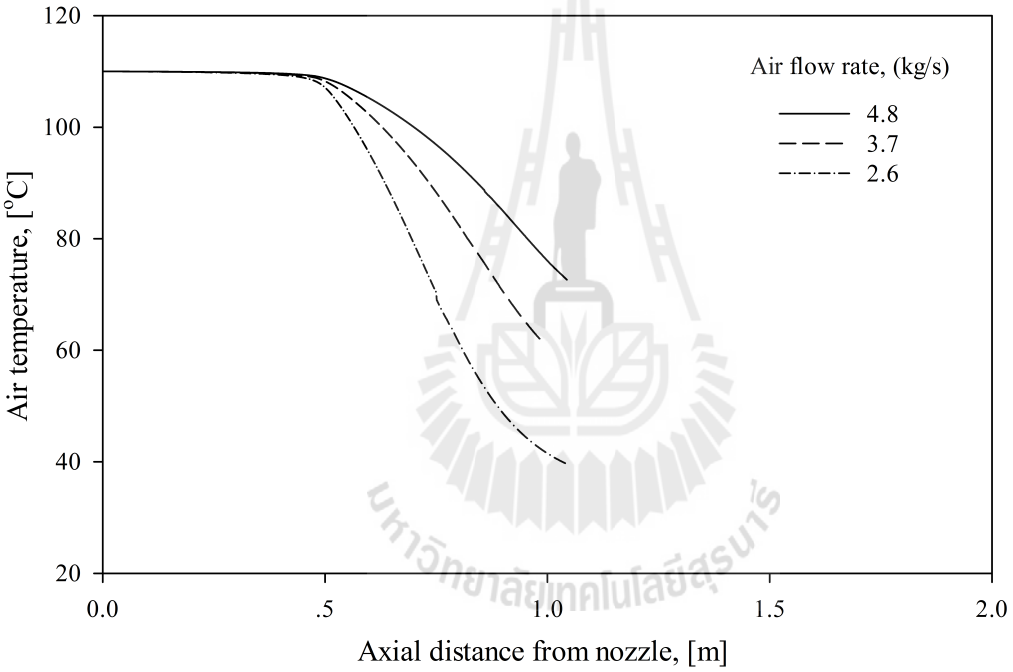

Figure 48: Air temperature profiles in the dryer at various air feed rates.

At low flow rate of feed air, the droplet moisture decreases quickly in the constant rate period, but then slowly declines in the falling rate, as observed in Fig. 49. This confirms that the evaporation rate is high in the constant rate period, but rapidly reduces along the dryer height in the falling rate period.

Figure 50 shows that the average droplet temperatures quickly increases at high air feed rates in the falling rate period. But, at low air feed rate, the droplet temperature slowly rises and then attains an equilibrium value. The rapid changes of droplet

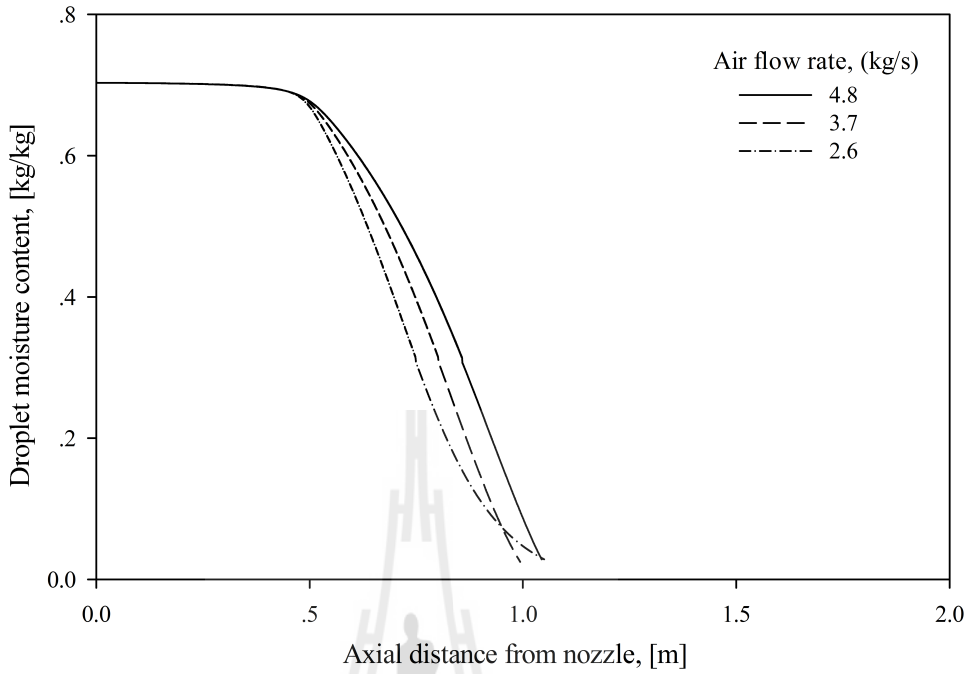

Figure 49: Profiles of droplet moisture content in the dryer at various air feed rates.

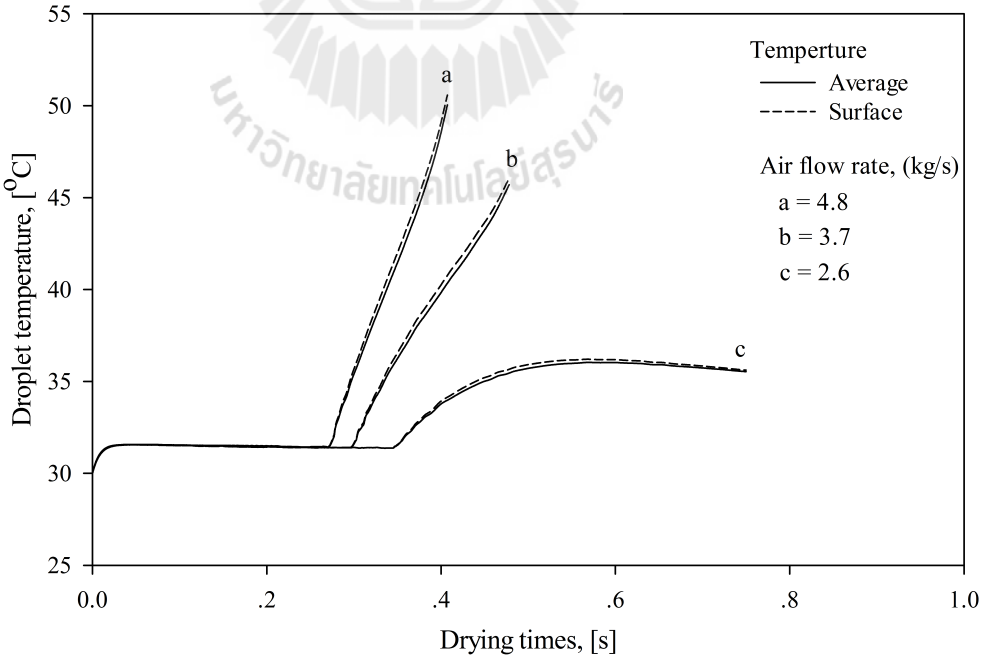

Figure 50: Variations of droplet average temperature with drying time at various air feed rates.

temperature at high air flow rate can be attributed to the enhancement of convective heat and mass transfer as the significant amount of heat is supplied to the dryer resulting in an increase of the air temperature. In the case of low air flow rate, the less amount of heat is delivered to the dryer and the rates of convective heat and mass transfer are declined yielding to the slow rise in the droplet temperature. Since the air temperature is relatively low, the drying process operates close to the equilibrium conditions.

Figure 51 illustrates the temperature profiles inside the droplet at various air feed rates. These data were collected at different drying times corresponding to the same thickness of the dry crust. The surface temperature of droplets and the heat transfer resistance in the dry crust layer grow as the air feed rate rises. The temperature difference between the droplet surface and the evaporation interface grows with air feed rate due to the decline of thermal conductivity of water vapor-air mixture in the dry crust and as a result of accumulation of water vapor inside the dry crust.

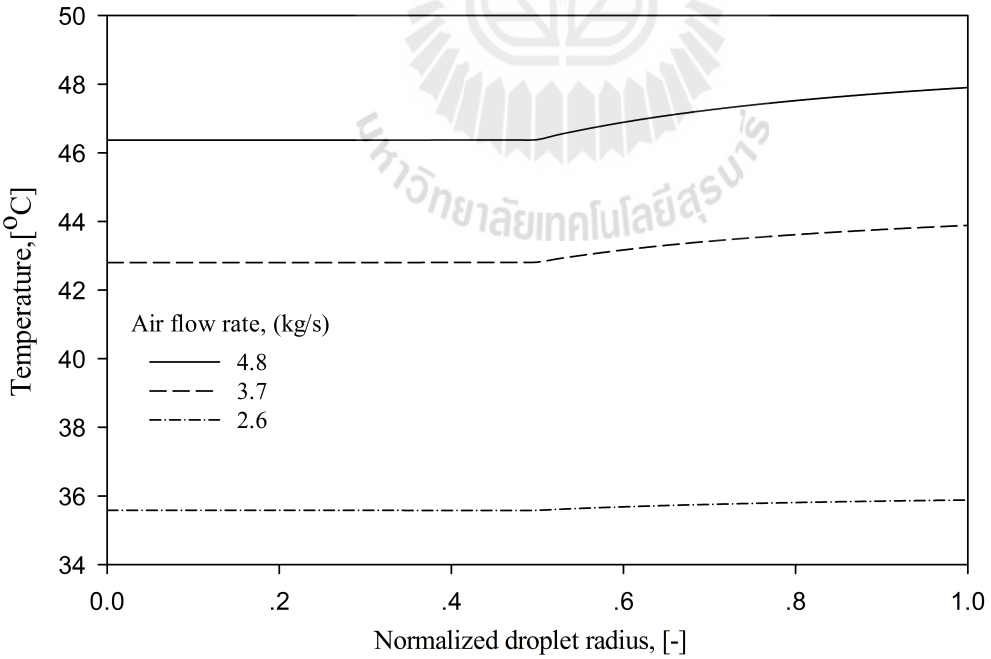

Figure 51: Temperature distributions in the droplet at various air feed rates.

The temperature at the evaporation interface increases with air feed rate as the pressure inside the dry crust builds up due to the high concentration of water vapor at the interface, as observed in Fig. 52. This yields to the high temperature of wet core owing to the low resistance to heat transfer in the core region.

The concentration of water vapor at the surface of droplet decreases at high air feed rate due to an enhancement of the rate of convective mass transfer and decline of air humidity, as shown in Fig. 52. However, a significant crust mass transfer resistance and the high evaporation rate result in the accumulation of water vapor in the crust layer at high air feed rate.

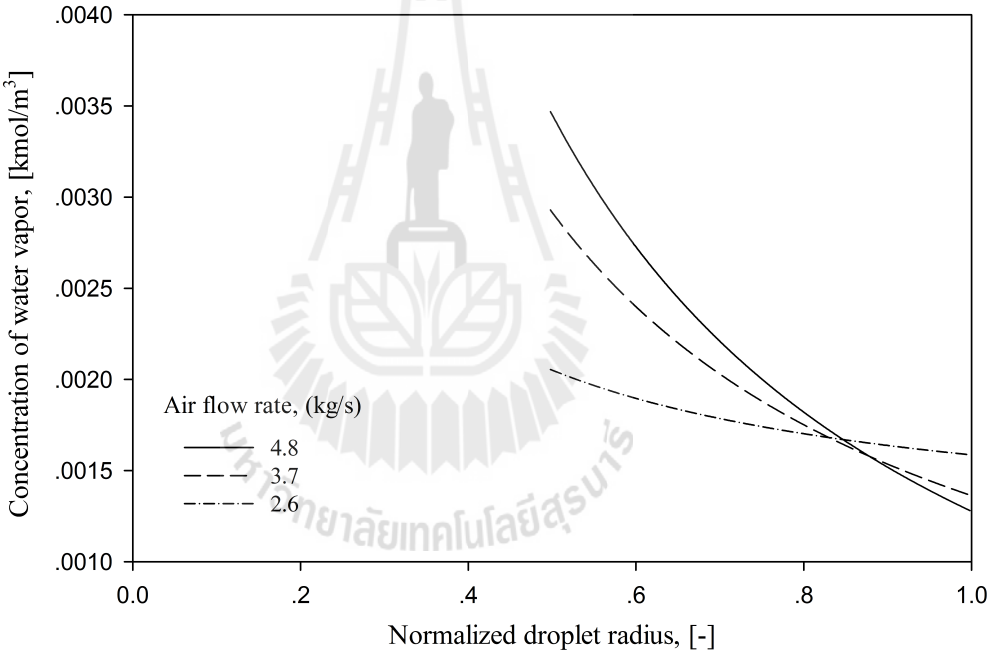

Figure 52: Distributions of water vapor concentration in the droplet at various air feed rates.

The air humidity declines as the air feed rate rises, as shown in Fig. 53, since the large amount of air is available for accommodation of evaporating water vapor in the dryer.

Figure 54 illustrates the profiles of average and surface droplet temperatures along the axial distance of the dryer. At high air feed rate, the droplets get hot in the final stage of drying due to the high rate of convective heat transfer at high air temperature,

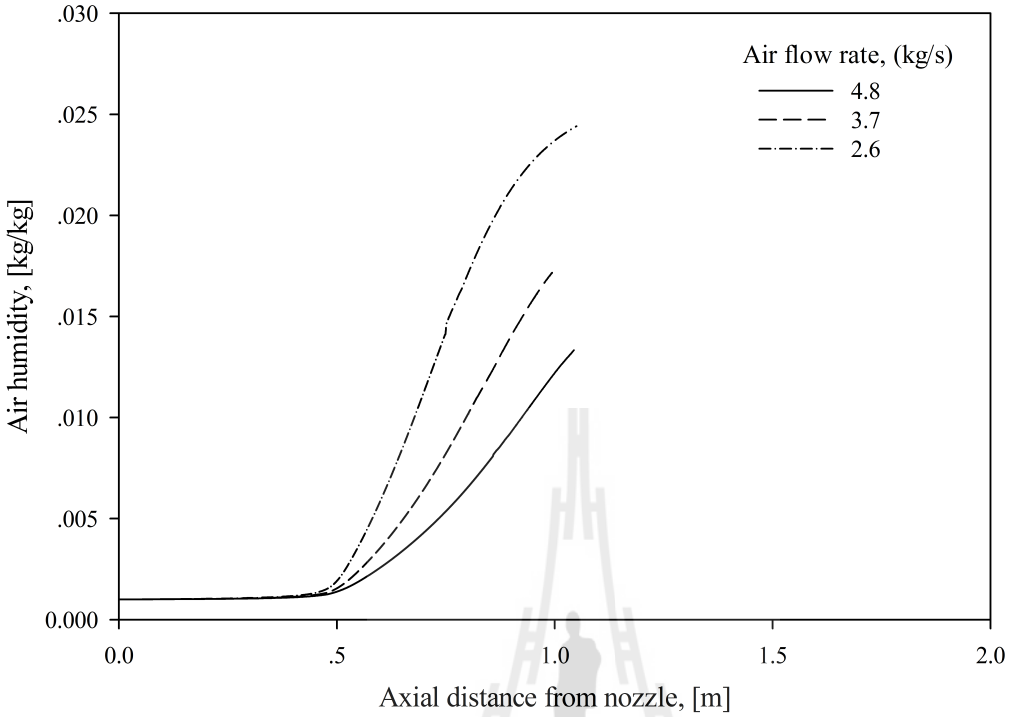

Figure 53: Air humidity profiles in the dryer at various air feed rates.

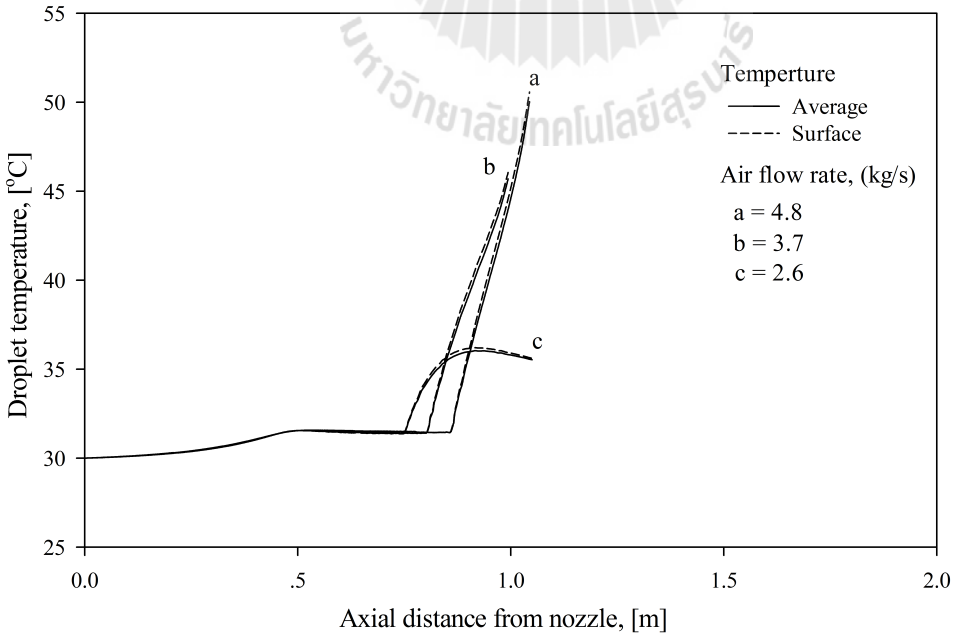

Figure 54: Air temperature profiles in the dryer at various air feed rates.

but the longer drying distance is required to dry droplets to the prescribed final moisture content owing to their high velocity. In the case of low air feed rate, the droplet conditions are closed to the equilibrium one resulting in significant decrease of the drying rate and longer drying distance.

The droplets will cover a longer distance along the dryer height at high air feed rate than that at low one in the constant rate period due to their high velocity, but a shorter distance in the falling rate period owing to an enhancement of convective heat and mass transfer.

5.2.4 Effect of inlet air temperature

The energy required for evaporation of water in the droplets is supplied from the drying air to the droplet surface by convective heat transfer. The temperature of drying air declines along the height of drying chamber, as illustrated in Fig. 55. During the initial heating-up period, the air temperature slightly decreases as only a small amount of energy is consumed for heating droplets from the inlet up to the wet bulb temperatures. However, the drying air temperature rapidly decreases both in the constant and falling rate periods when the large amount of heat is consumed for water evaporation from droplets. Air supplied to the dryer at high temperature cools down in a short distance along the dryer height due to the enhanced rate of convective heat transfer.

An increase of the inlet air temperature from 101°C to 150°C results in rapid growth of air humidity due to an enhancement of the rate of convective mass transfer of water vapor from the droplet surface to the drying air, as shown in Fig. 56. In the present calculations, the humidity of outlet air is constant regardless of inlet air temperature as an equal amount of water to be evaporated during drying of droplets up to the fixed residual moisture content.

The velocity of air at high inlet air temperature is slightly higher than that at low one, as illustrated in Fig. 57, due to the decline of air density as the temperature rises.

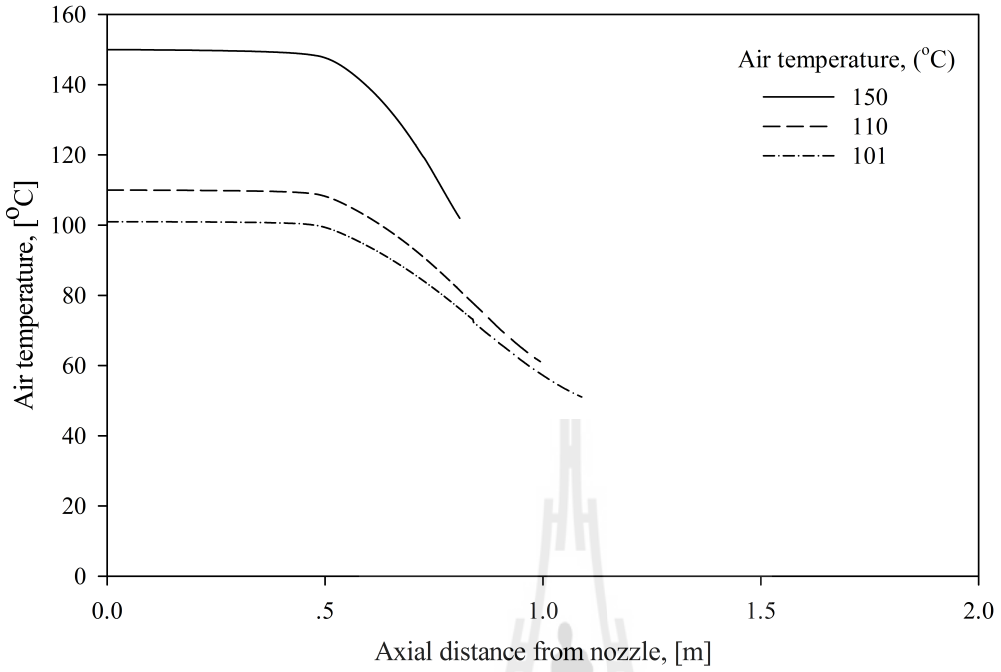

Figure 55: Air temperature profiles in the dryer at various inlet air temperatures.

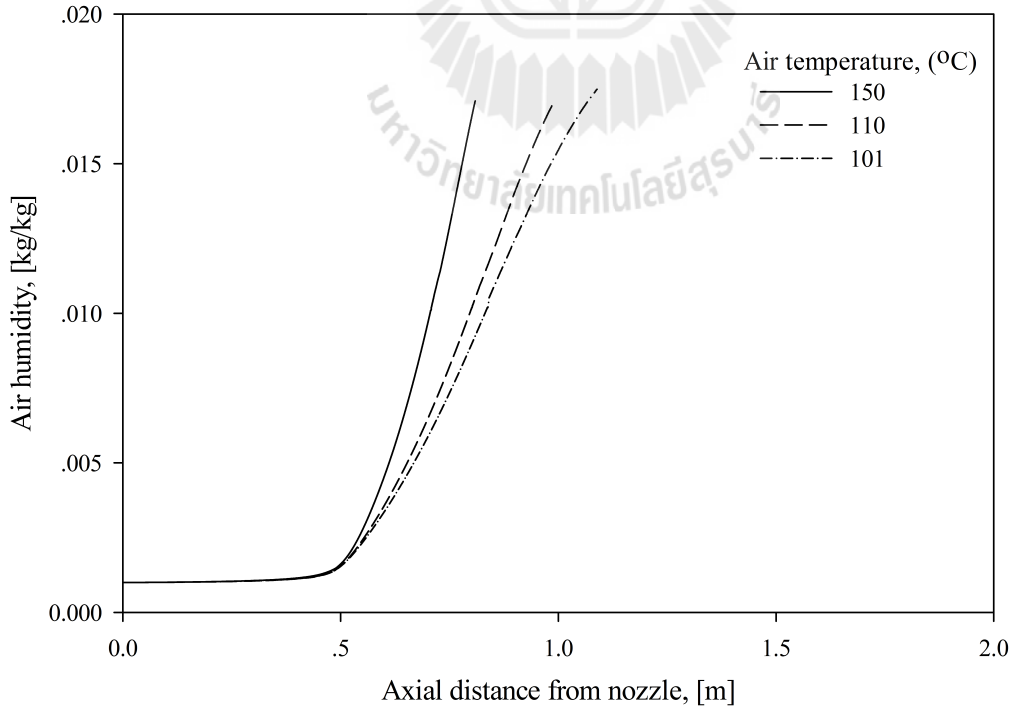

Figure 56: Air humidity profiles in the dryer at various inlet air temperatures.

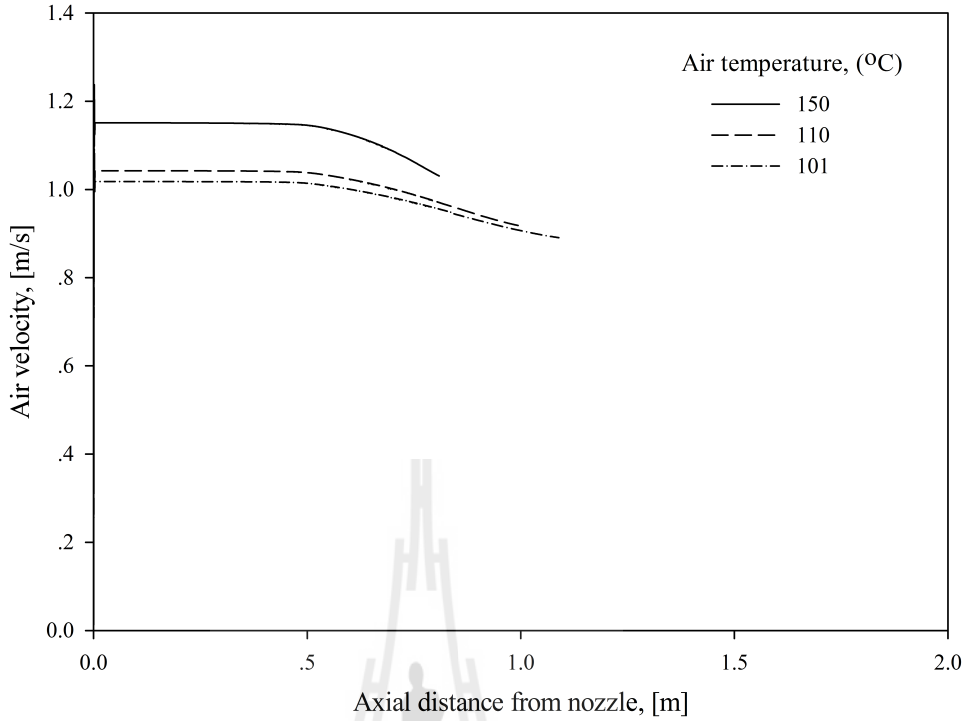

Figure 57: Air velocity profiles in the dryer at various inlet air temperatures.

The profiles of axial and radial droplet velocities are almost identical to each other for drying air of different inlet temperatures, as indicated in Fig. 58, since the initial droplet size as well as the initial droplet velocities both in the radial and axial directions are fixed to prescribed values. However, the axial droplet velocity is somewhat higher at high inlet air temperature to follow the air velocity profile. As a result, profiles of droplet velocity relative to air are similar to each other for drying air supplied to the chamber at different temperatures, as confirmed in Fig. 59.

The shorter time is required to dry droplets using air at high inlet temperature than that at low one. The average and surface droplet temperatures rapidly increases with drying time in the case of hot inlet air due to the enhancement of rate of convective heat and mass transfer, as illustrated in Fig. 60. The product temperature also increases at high inlet air temperature because of the high amount of energy available in the outlet air.

The droplet axial and radial velocities do not differ significantly with inlet air

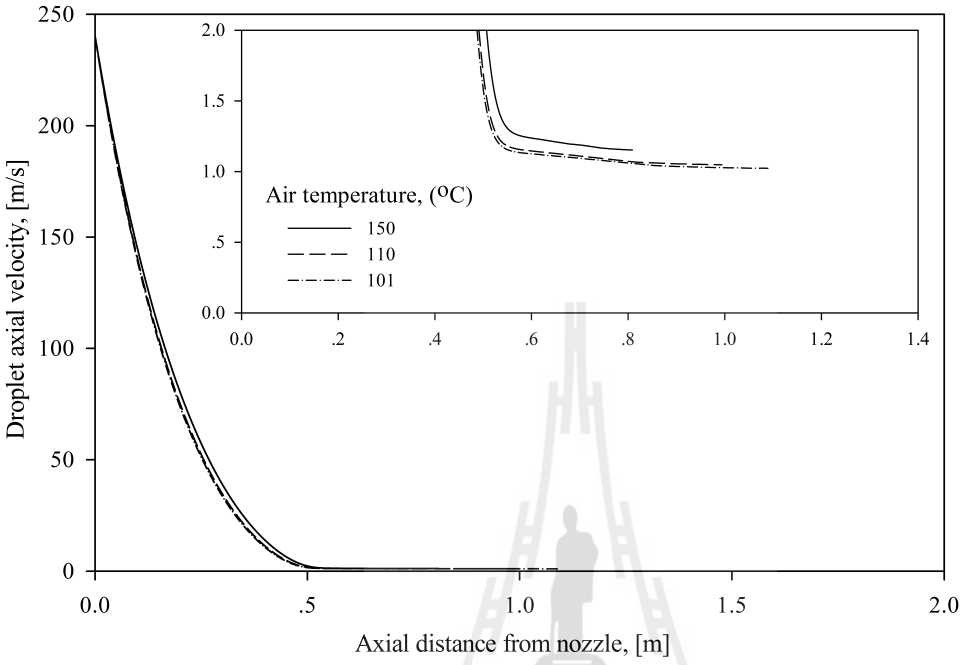

(a)

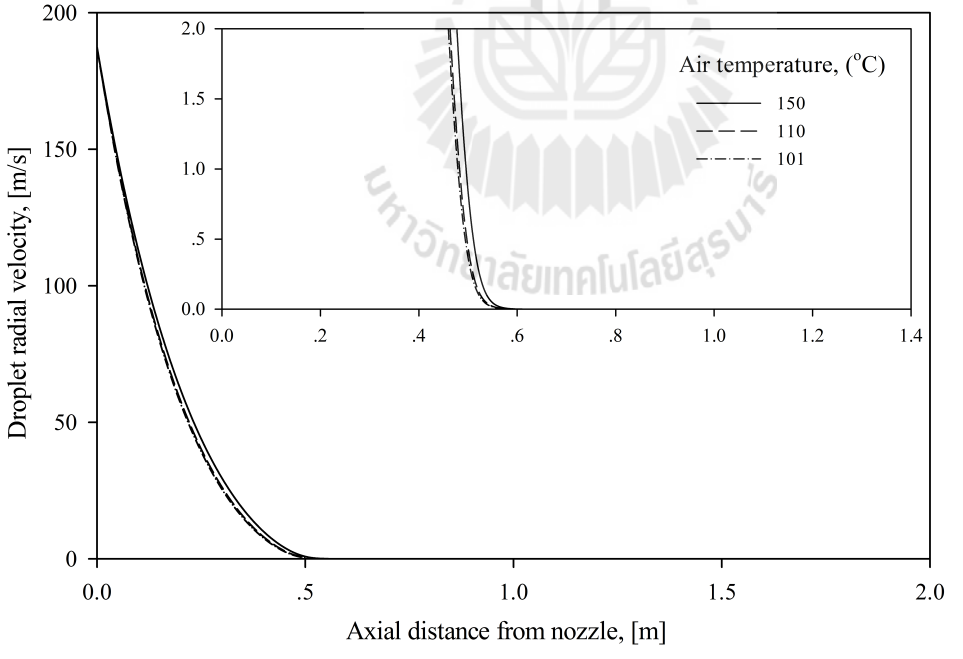

(b)

Figure 58: Velocity profiles of droplets in the dryer at various inlet air temperatures: (a) axial and (b) radial.

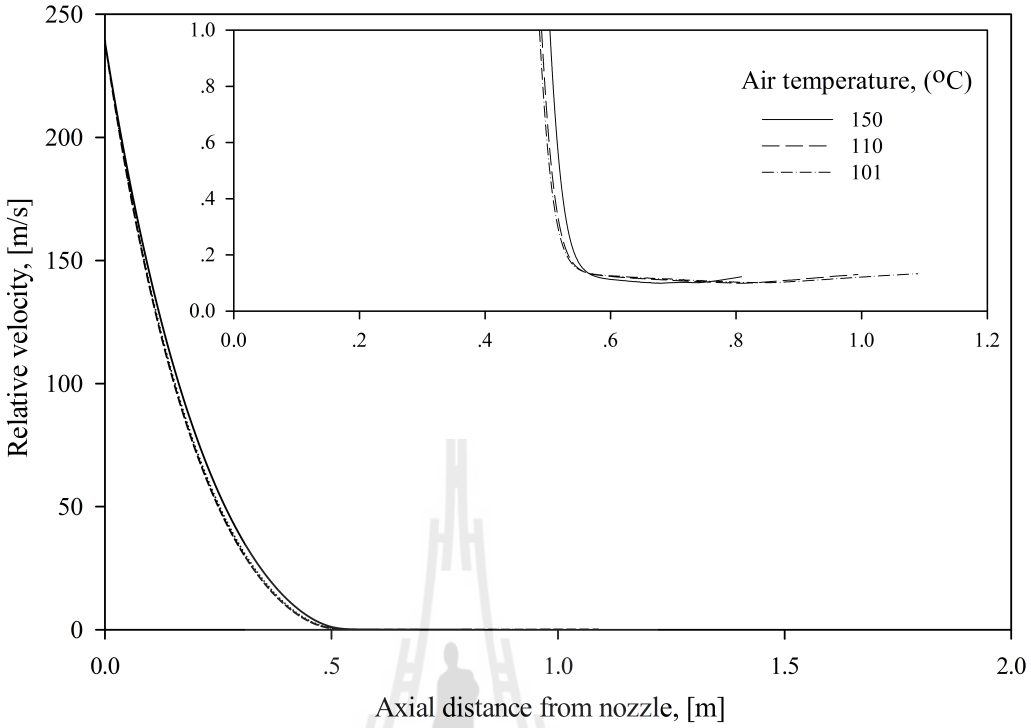

Figure 59: Profiles of relative droplet velocity in the dryer at various inlet air temperatures.

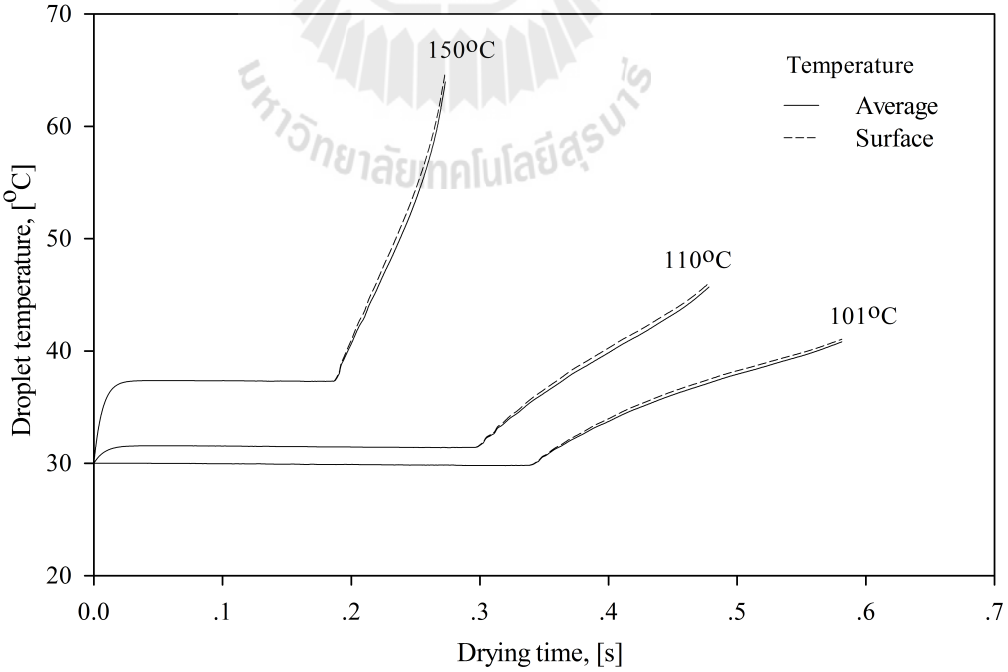

Figure 60: Variation of droplet average and surface temperatures with time at various inlet air temperatures.

temperature. Therefore, the short drying distance of droplets in Fig. 60 indicates that the drying rate increase at high inlet air temperature. The droplets travel relatively long distances in the initial heating-up period, as observed in Fig. 61, due to their high velocities both in the axial and radial directions. In the constant and falling rate periods, the droplet drying distances along the dryer height are shorter at high inlet air temperature than those at low one due to the enhanced rate of convective heat transfer.

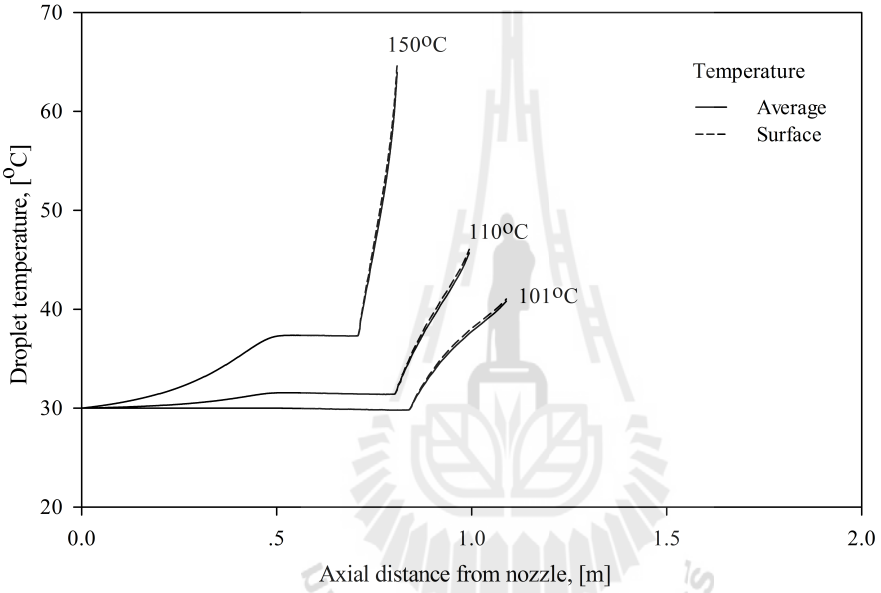

Figure 61: Profiles of droplet average and surface temperatures at various inlet air temperatures.

The moisture content and weight of droplets decrease rapidly along the axial distance of the dryer at high air inlet temperature, as displayed in Figs. 62 and 63. These data also confirm that the drying rate increases as the air temperature rises.

Figure 64 illustrates the profiles of temperature and vapor concentration in the droplet for the same thickness of the dry crust layer. The effect of inlet air temperature on mechanism of heat transfer in the droplet is similar to one of air flow rate. The droplet surface, evaporation interface and wet core temperatures increase as the inlet air temperature rises, as indicated in Fig. 9, due to the enhancement of the convective heat transfer coefficient.

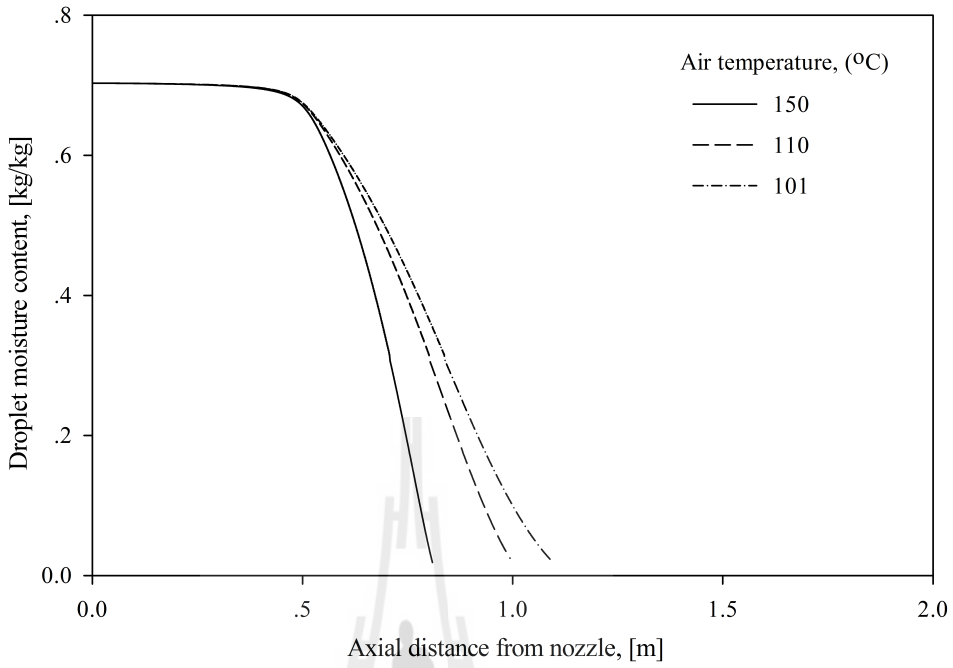

Figure 62: Profiles of droplet moisture content in the dryer at various inlet air temperatures.

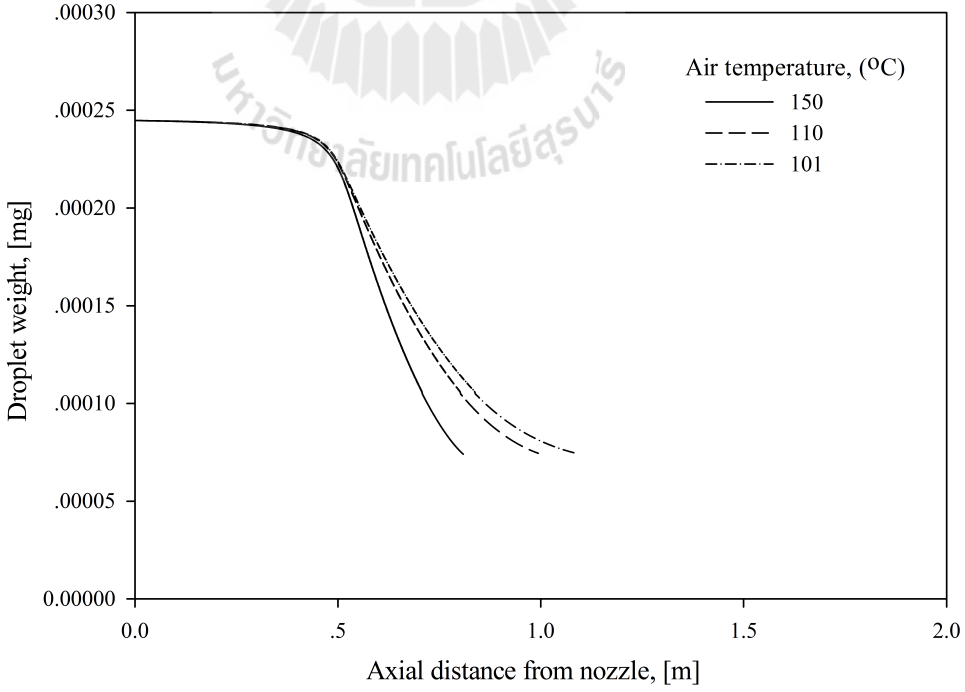

Figure 63: Profiles of droplet weight in the dryer at various inlet air temperatures.

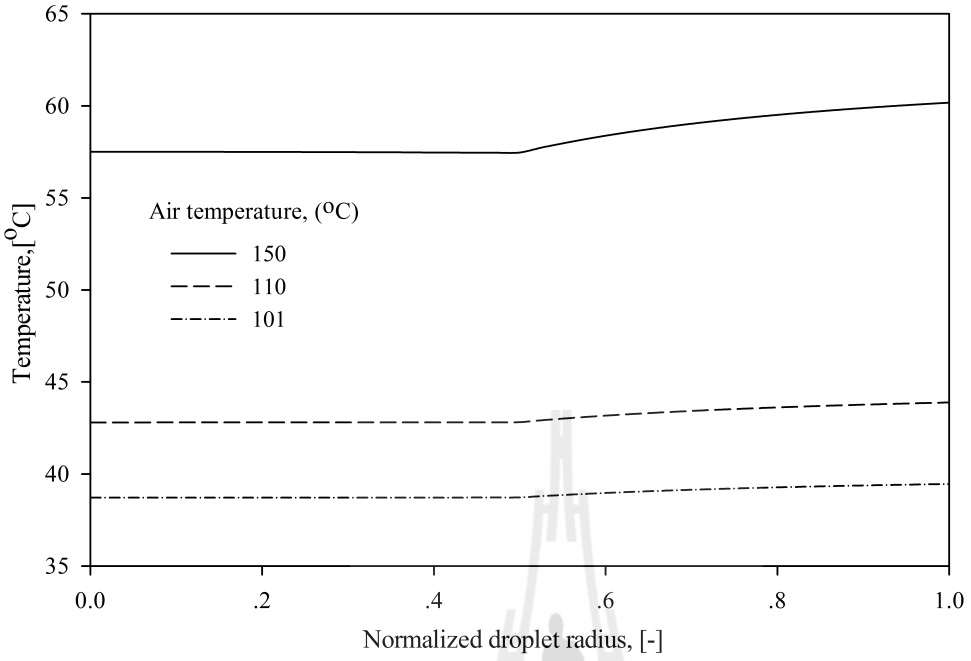

Figure 64: Temperature distributions in the droplet at various inlet air temperatures.

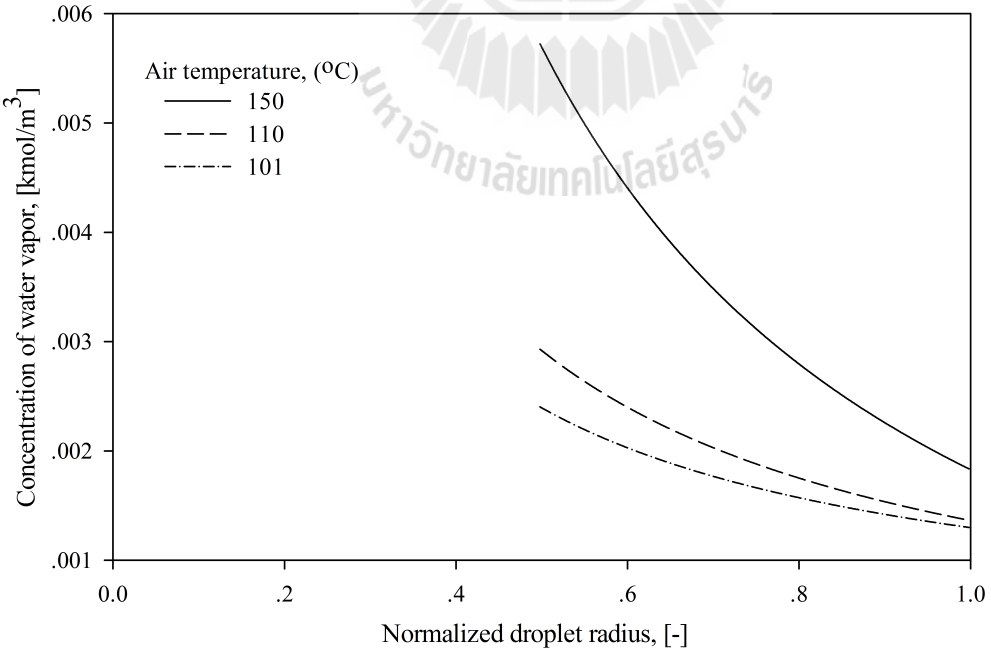

Figure 65: Distributions of water vapor concentration in the droplet at various inlet air temperatures.

The influence of inlet air temperature on the mechanism of mass transfer inside the droplet is also similar to one of the air flow rate. The accumulation of water vapor in the droplet is observed in Fig. 65 at high inlet air temperature as the large amount of heat is supplied to the evaporation interface and the rate of mass transfer in the droplet is limited owing to the mass transfer resistance in the dry crust layer.

5.2.5 Influence of slurry concentration

The effect of slurry concentration on the drying behavior of droplets in the dryer is investigated by fixing the size and porosity of product particles at prescribed values. Therefore, the amount of solid materials in a droplet is the same for different concentration slurries. The small droplets are generated by spraying the concentrated slurry due to the low water quantity in a droplet.

The initial moisture content of droplets formed from the concentrated feed is low and it decreases up to the final value in a short distance from the nozzle along the dryer height, as illustrated in Fig. 66, owing to the low amount of water in a droplet and the high rate of convective heat and mass transfer for droplets of small sizes.

Figure 67 confirms that the lightweight droplets are generated by spraying high-concentration slurries. However, the final droplet weights are the same irrespective of the slurry concentration due to the identical solid amount and moisture content of product particles.

The axial and radial velocities of droplets generated from the concentrated slurry are lower than velocities of droplets obtained from the dilute slurry in the initial heating-up period, as indicated in Fig. 68. This is because the small size droplets of low weight are formed from the slurry feed of high concentration.

The axial velocities of droplets slightly differ in the constant rate period due to the difference in their weight, but the velocity profiles are found to coincide with each other in the falling rate period owing to the same size and weight of droplets.

In the present simulation, the total amount of water to be evaporated in the dryer

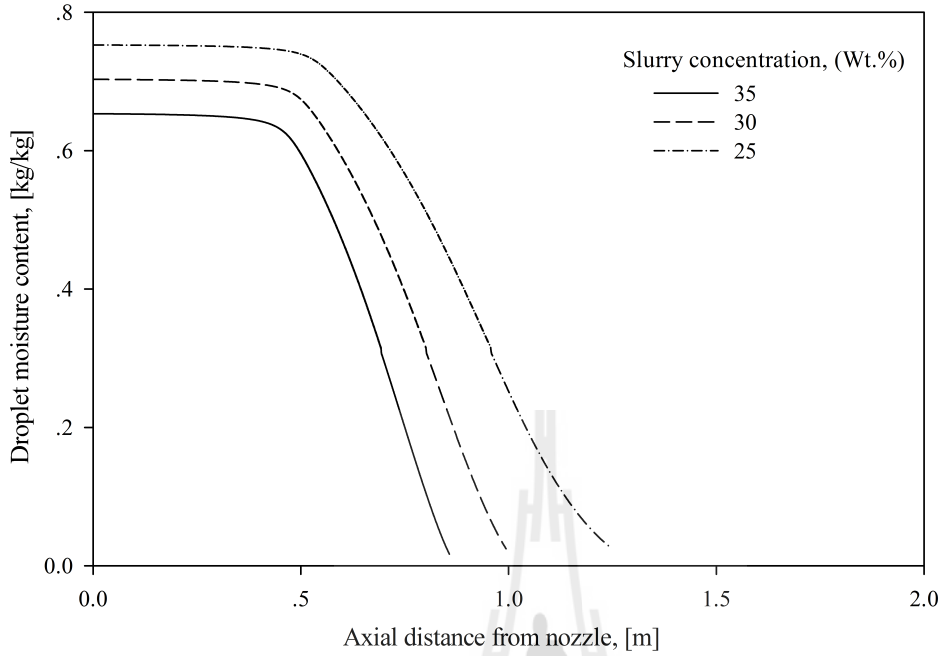

Figure 66: Profiles of droplet moisture content in the dryer at various slurry concentrations.

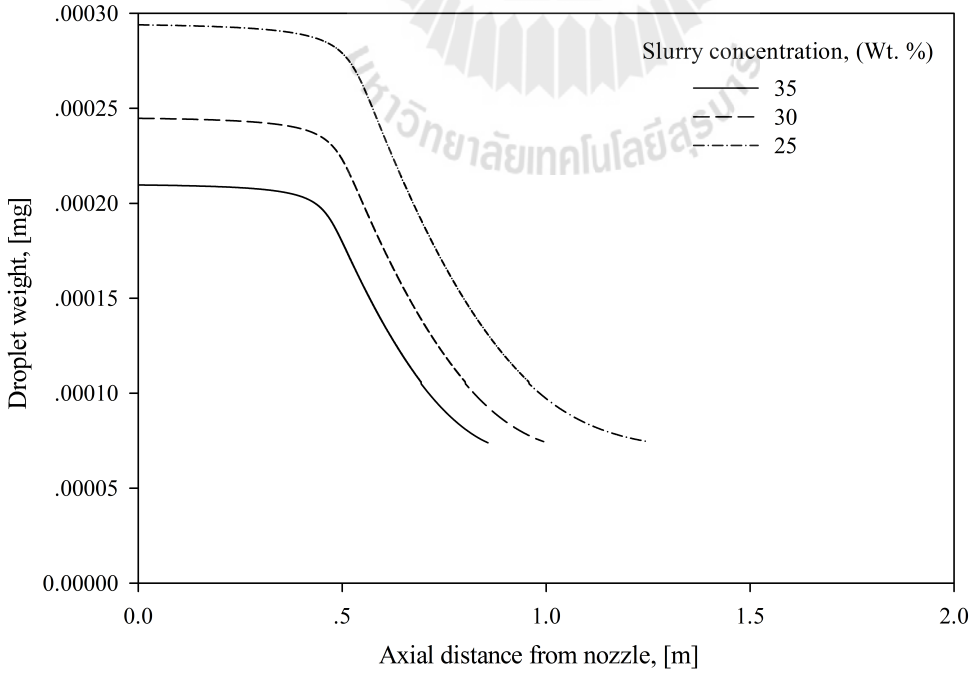

Figure 67: Profiles of droplet weight in the dryer at various slurry concentrations.

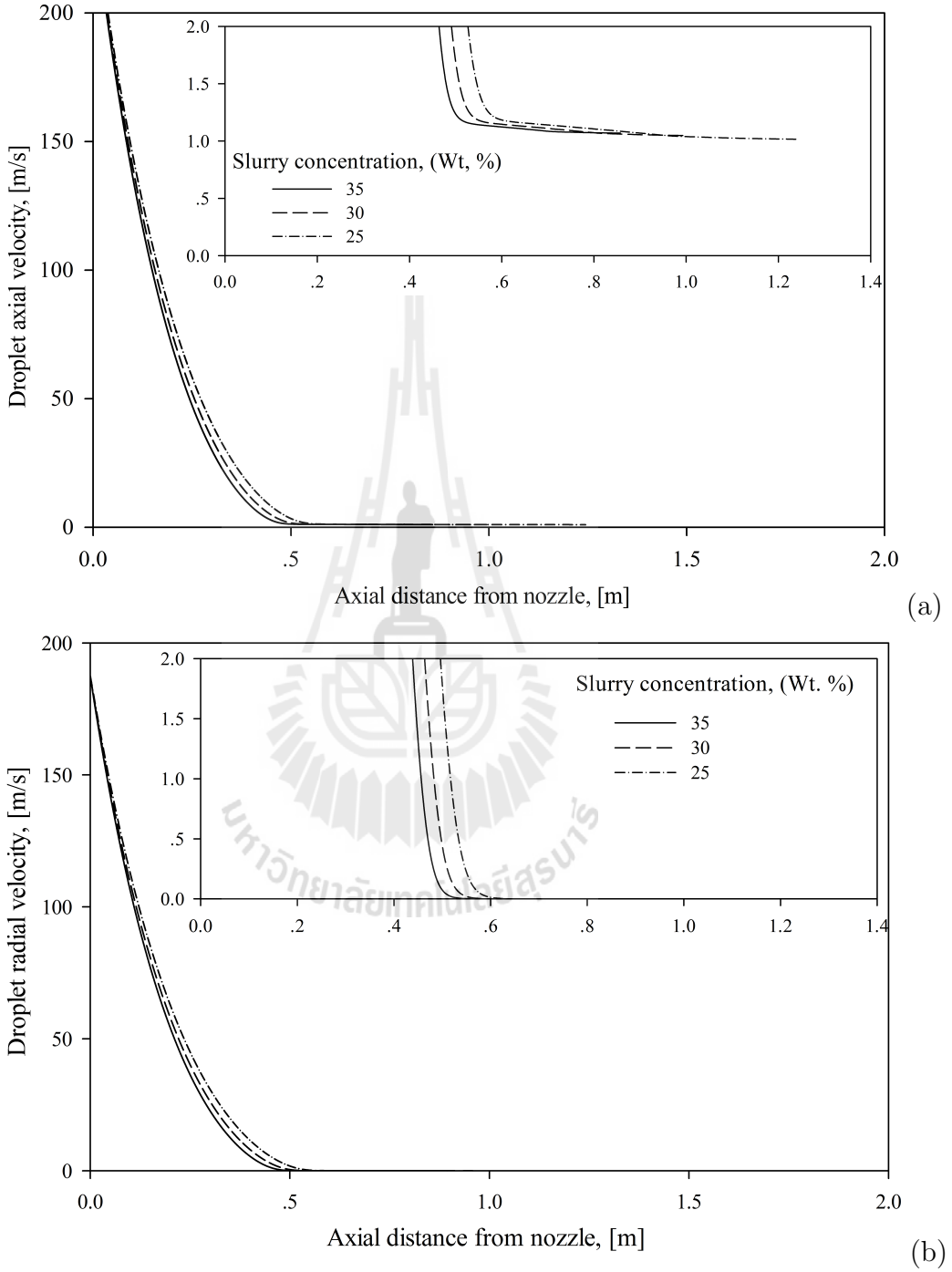

Figure 68: Profiles of droplet velocities in the dryer at various slurry concentrations: (a) axial and (b) radial.

varies with slurry concentration because the production rate and the moisture content of product particles are kept constant.

In the case of concentrated slurry, the air temperature quickly decreases and humidity increases along the axial distance of the dryer, as illustrated in Figs. 69 and 70. The outlet air temperature is high and humidity is low, due to the low energy consumption on evaporation of small quantity of water to reach the target moisture content.

The air velocity in the dryer is slightly lower during drying of concentrated slurry feed than dilute one, as illustrated in Fig. 71, due to the enhancement of air density at low temperature. The profiles of relative droplet velocity in the axial direction of the dryer are close to each other for slurries of various concentrations, as shown in Fig. 72.

The drying time of droplets generated from the concentrated slurry feed is short and they travel short distances along the dryer height to reach the final temperature, as shown in Figs. 73 and 74. The average droplet temperature is higher in the final stage of drying of concentrated feed than that of dilute one due to the high outlet air temperature.

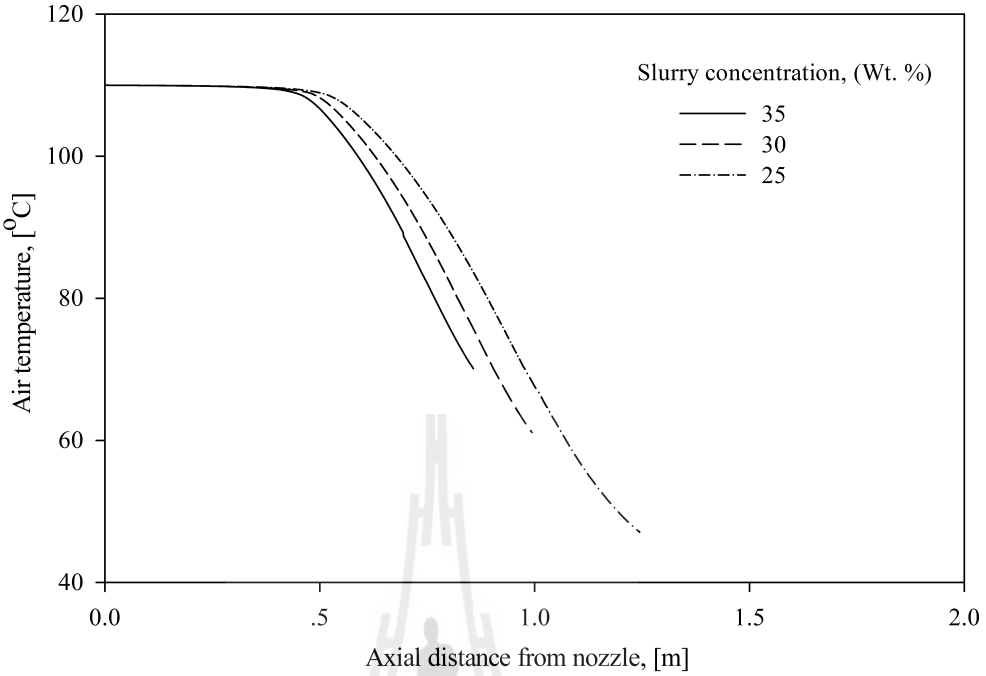

Figure 69: Air temperature profiles in the dryer at various slurry concentrations.

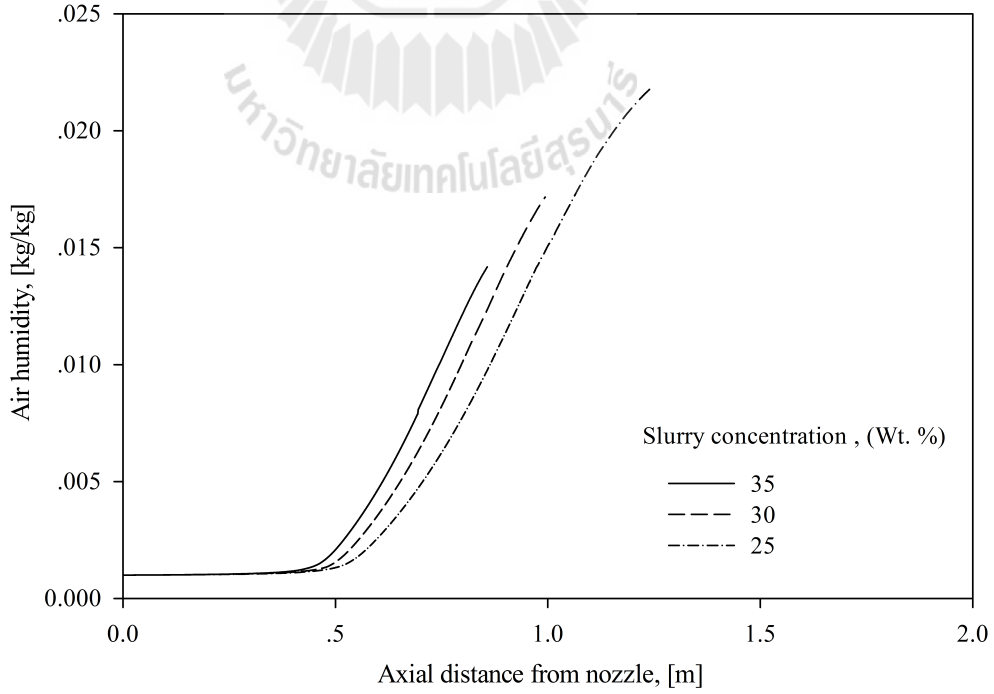

Figure 70: Air humidity profiles in the dryer at various slurry concentrations.

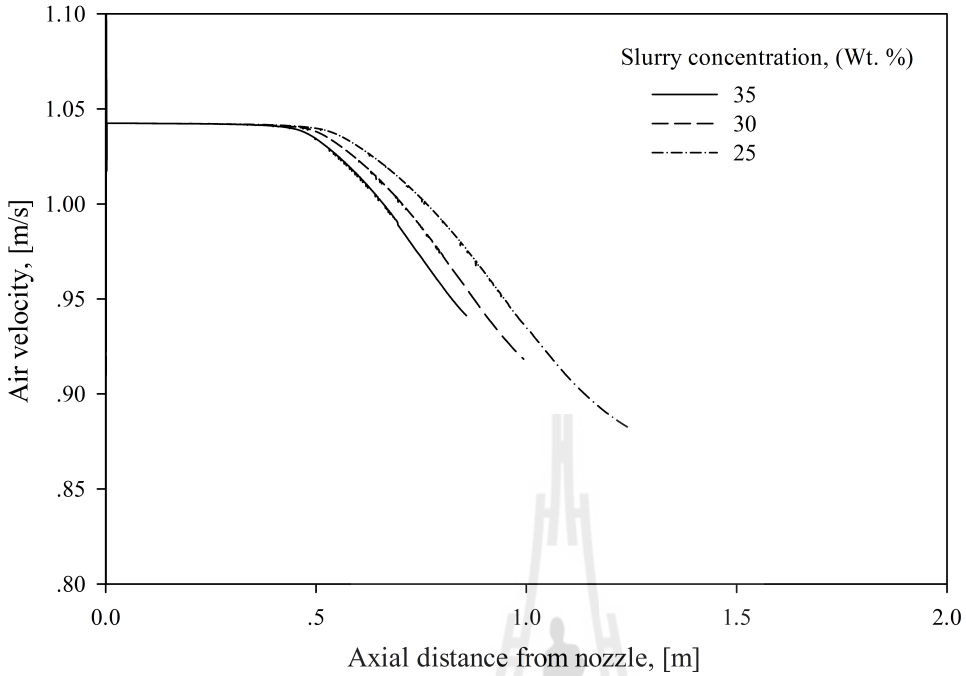

Figure 71: Air velocity profiles in the dryer at various slurry concentrations.

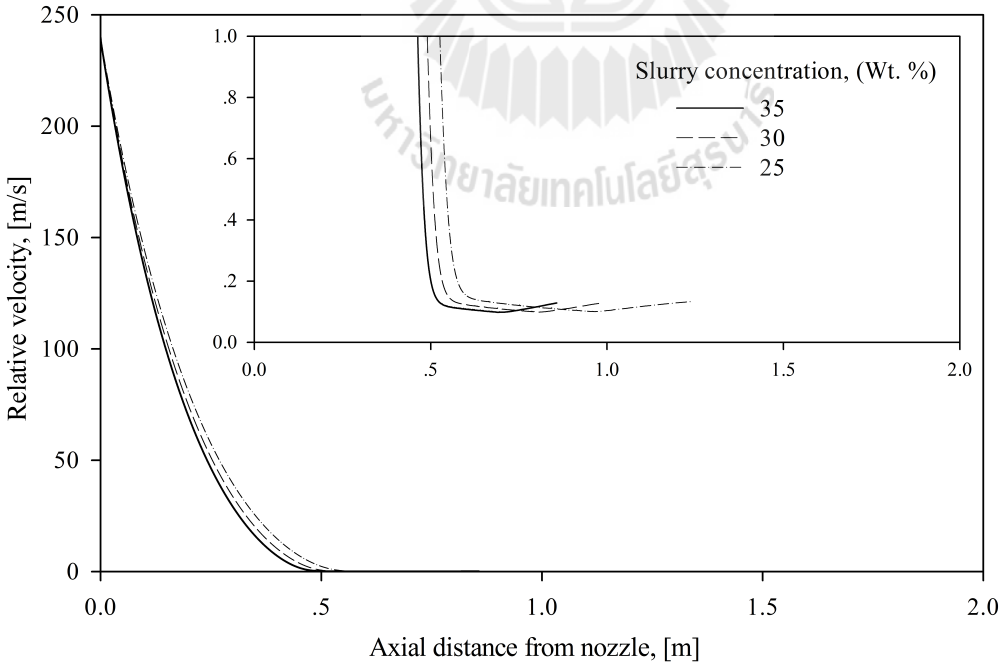

Figure 72: Profiles of droplet relative velocity in the dryer at various slurry concentrations.

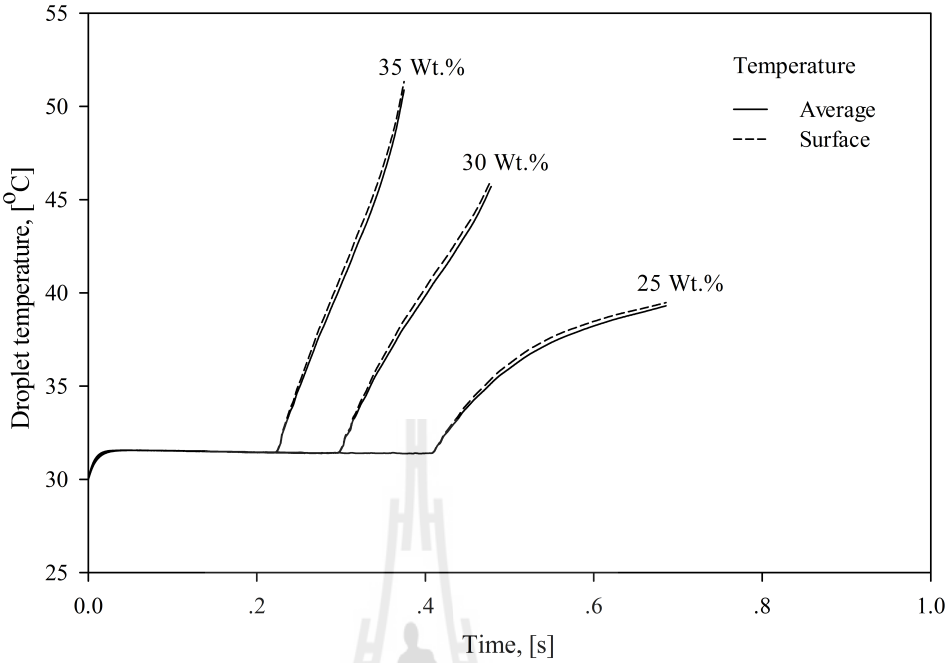

Figure 73: Variations of droplet temperature with drying time at various slurry concentrations.

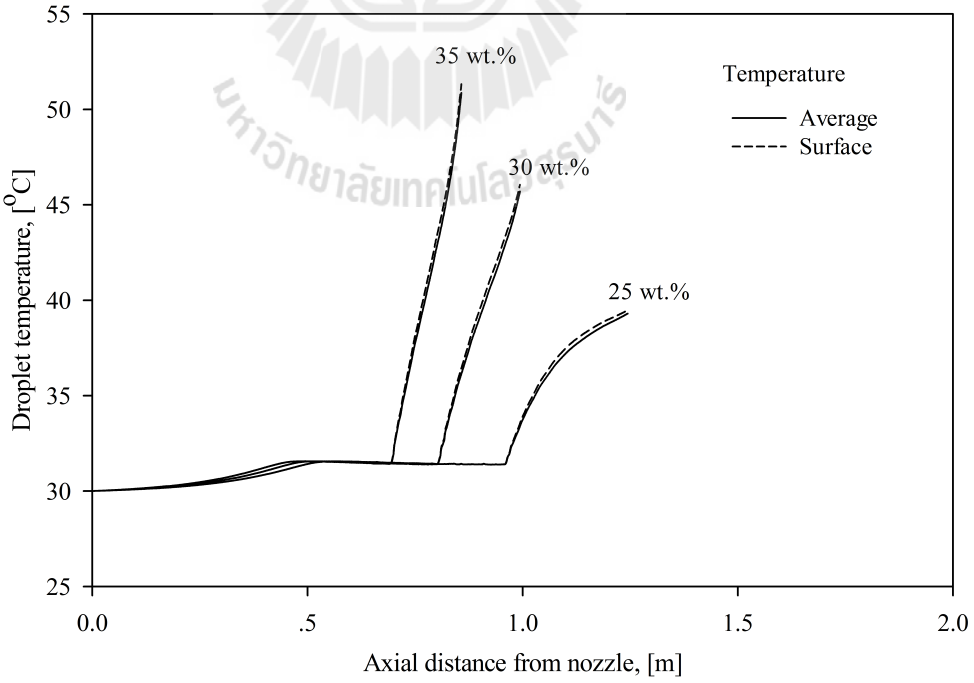

Figure 74: Profiles of average droplet temperatures in the dryer at various slurry concentrations.

5.2.6 Influence of initial droplet size

The variation of the droplet weight along the axial distance of the dryer is illustrated in Fig. 75 for droplets of various initial sizes generated from the slurry of constant solid concentration. The larger the initial droplet, the greater the amount of water to be evaporated from the droplet to reach the same final moisture content of dried particles. The droplet weight only slightly decreases in the initial heating-up period and then quickly drops during the constant rate period as the large amount of water evaporates from the droplet surface to air. The rate of change of droplet weight decreases during the falling rate period when the evaporation interface moves into the droplet and the heat and mass transfer resistances in the crust layer restrict the drying rate.

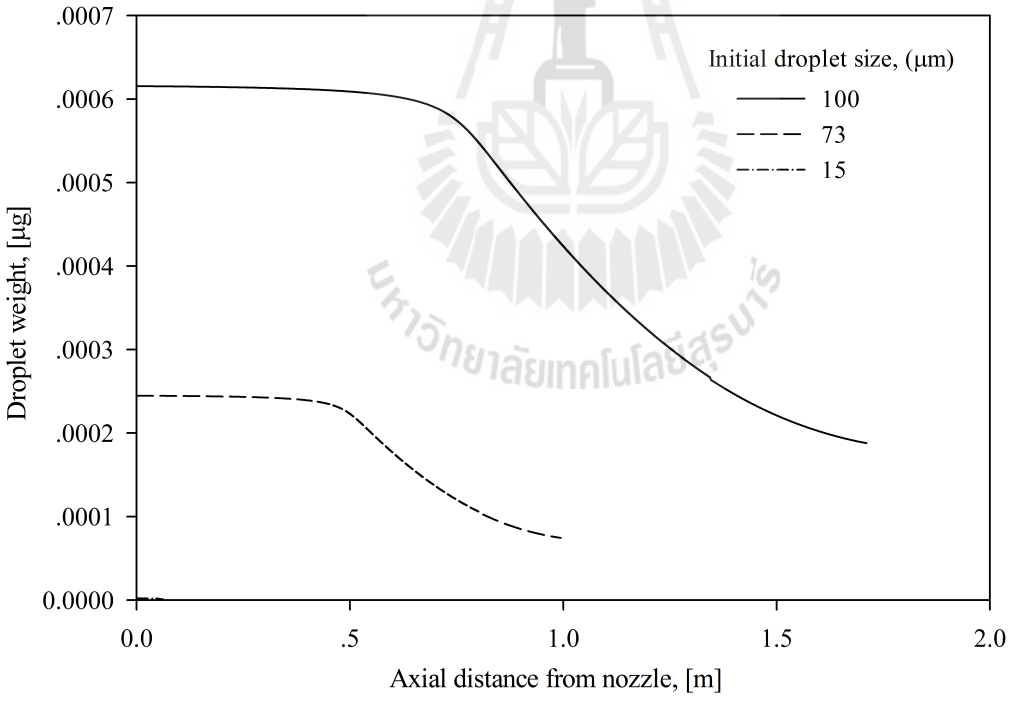

Figure 75: Profiles of droplet weight in the dryer for droplets of various initial sizes.

The initial moisture content is identical for droplets of various sizes formed from the slurry feed of uniform concentration, as illustrated in Fig. 76. However, the larger size droplets travel the longer distance along the dryer height than the smaller

ones to reach the same final moisture content due to the larger amount of water to be evaporated, higher droplet velocity and lower rate of convective mass and heat transfer.

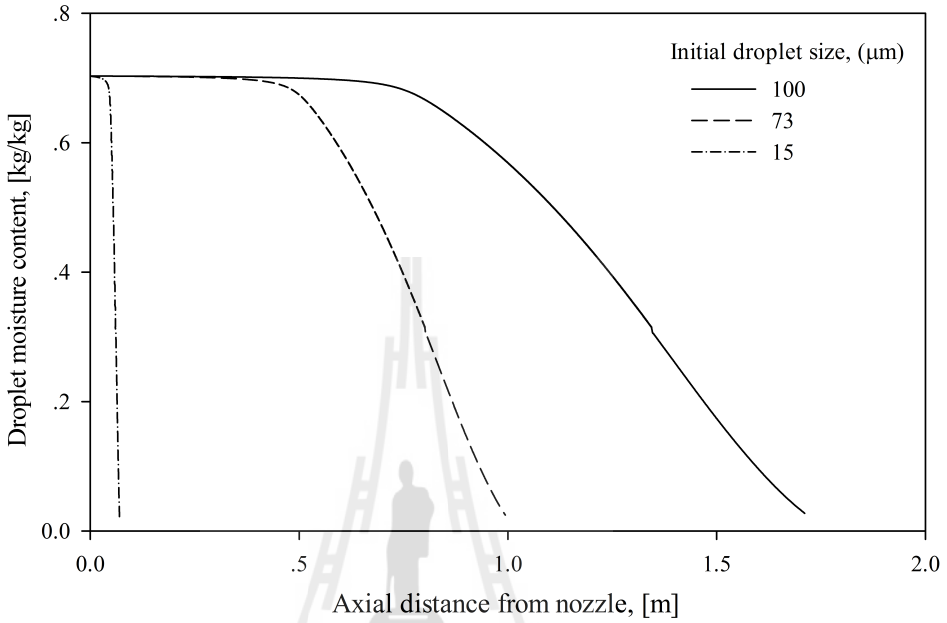

Figure 76: Profiles of droplet moisture content in the dryer for droplets of various initial sizes.

The distributions of droplet axial and radial velocities along the axial distance of the dryer are shown in Fig. 77 for droplets of various initial sizes. Both axial and radial droplet velocities rise with droplet size.

The temperature and humidity profiles of drying air are illustrated in Figs. 78 and 79. The air temperature quickly decreases and humidity rises during drying of droplets of small sizes due to their large specific surface area available for heat exchange with drying air resulting in the high rate of convective heat transfer. The outlet air temperature and humidity do not depend on the initial droplet size, but they are determined by the overall energy and mass balances in the dryer.

The air velocity quickly decreases in axial direction of dryer during drying of droplets of small initial sizes, as illustrated in Fig. 80, since a decline of the air temperature yields to a rise of the air density.

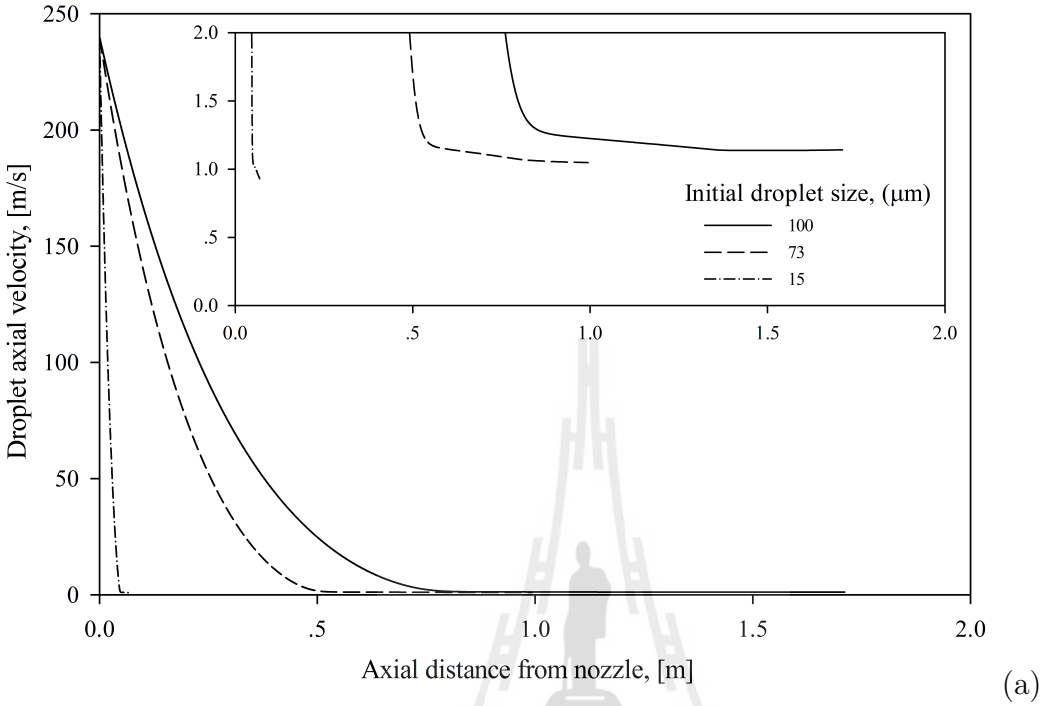

(a)

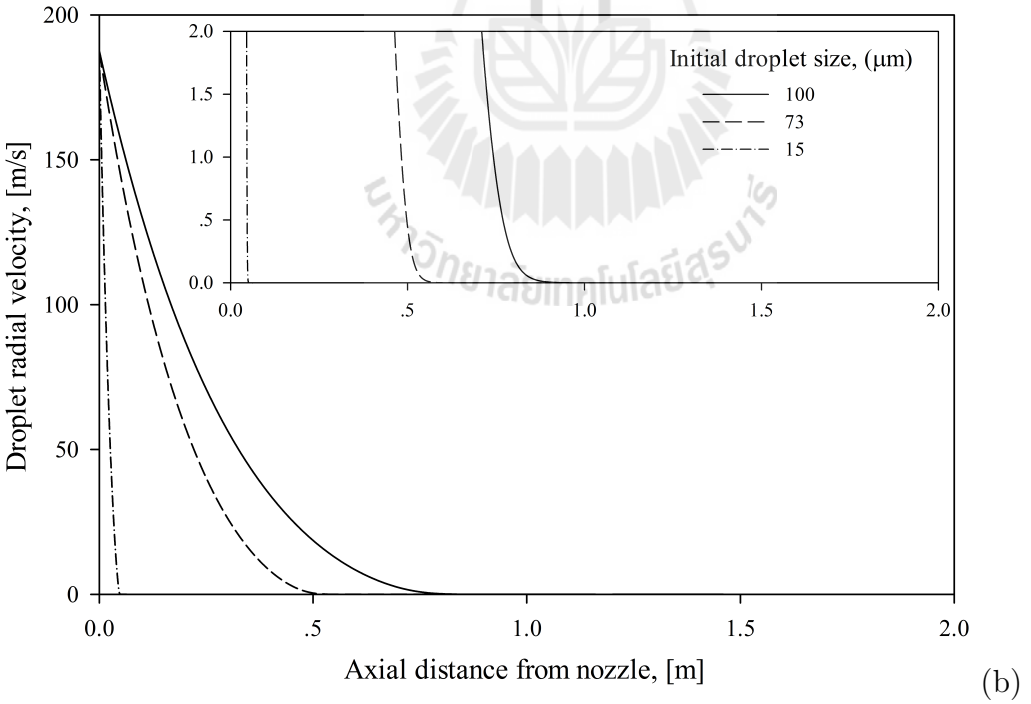

(b)

Figure 77: Profiles of droplet velocities in the dryer for droplets of various initial sizes: (a) axial and (b) radial.

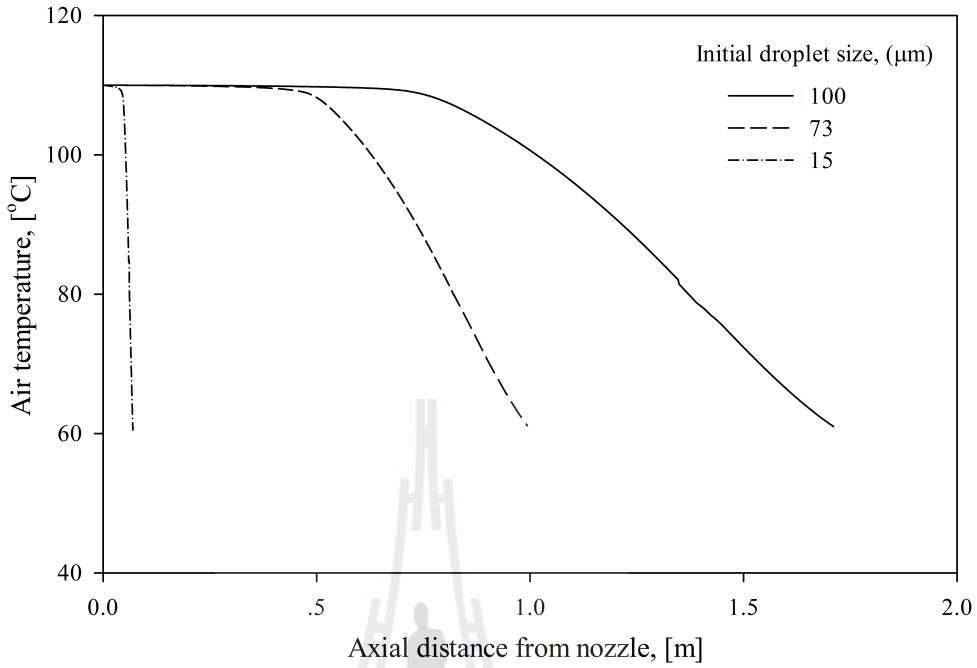

Figure 78: Air temperature profiles in the dryer for droplets of various initial sizes.

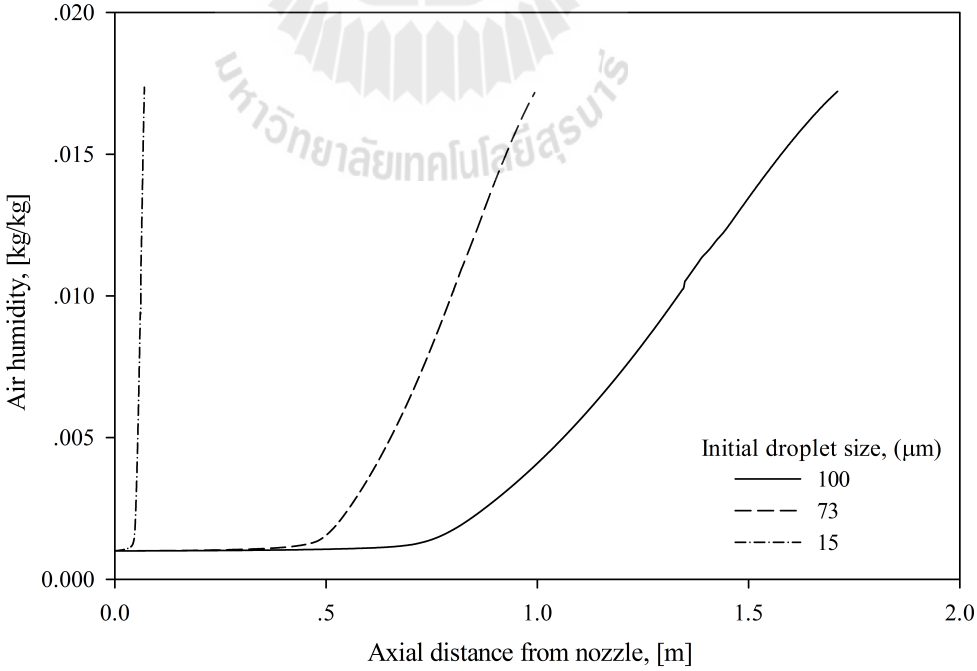

Figure 79: Air humidity profiles in the dryer for droplets of various initial sizes.

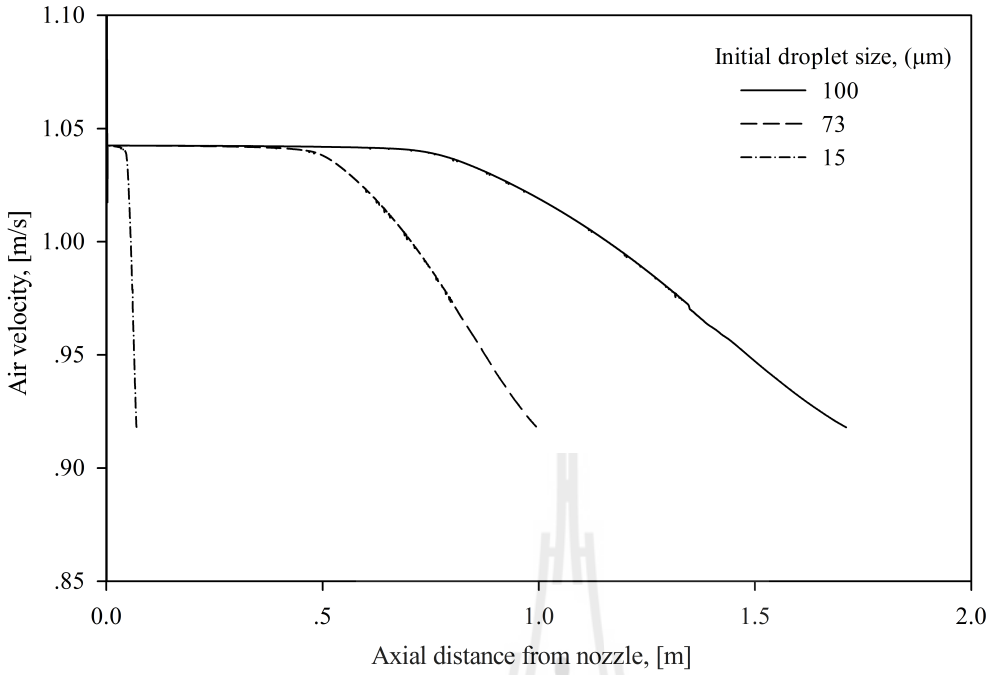

Figure 80: Air velocity profiles in the dryer for droplets of various initial sizes.

The relative velocity of droplets of large initial size is slightly higher than the one of small droplets, as illustrated in Fig. 81. This will lead to the enhancement of rate of convective heat and mass transfer between the droplet and air due to the formation of thinner boundary layers at the outer droplet surface. However, the larger the droplet size, the less surface area is available for mass and heat transfer with surrounding drying air resulting in the low rate of heat and mass transfer. Comparing two opposing contributions of droplet size into the heat and mass transfer, we can conclude that the later one has more effect on the rate of transfer. As a result, the heat and mass transfer rates decrease for large droplets, as illustrated in Fig. 82 by lower values of heat and mass transfer coefficients.

The convective heat and mass transfer coefficients are enhanced by increasing the air temperature and the droplet relative velocity, and by decreasing the droplet size. During the initial heating-up period, both coefficients do not change significantly as the air temperature and the droplet size are almost constant, although the relative droplet velocity decreases. In the constant rate period, the droplet size and the air

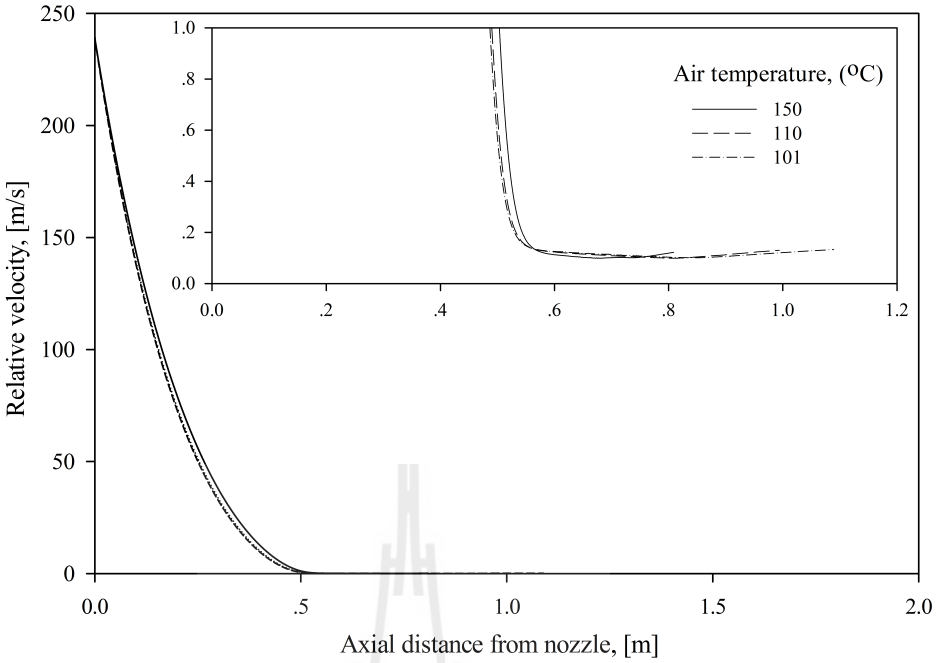

Figure 81: Profiles of droplet relative velocity for droplets of various initial sizes.

temperature decline, but the droplet relative velocity remains constant. However, the effect of droplet size on convective heat and mass transfer is larger than that of air temperature resulting in the enhancement of heat and mass transfer coefficients. In the falling rate period, the droplet size and relative velocity are constant, but the air temperature continue to decrease leading to the slight reduction of convective heat and mass transfer coefficients, as observed in Fig. 82.

The longer time is required to dry droplets of large initial size than that of the small ones, as shown in Fig. 83. The low drying rate by declined rates of convective heat and mass transfer and the large amount of water to be evaporated to reach the specified final moisture content of product lead to the long drying time of large droplets. The final temperatures of droplets of various sizes are close to each other due to the identical outlet air temperature.

The high initial velocity of large droplets results in the long drying distance during the initial heating-up period, as illustrated in Fig. 84. The drying of large droplets requires the long distances in the dryer in the constant and falling rate periods due

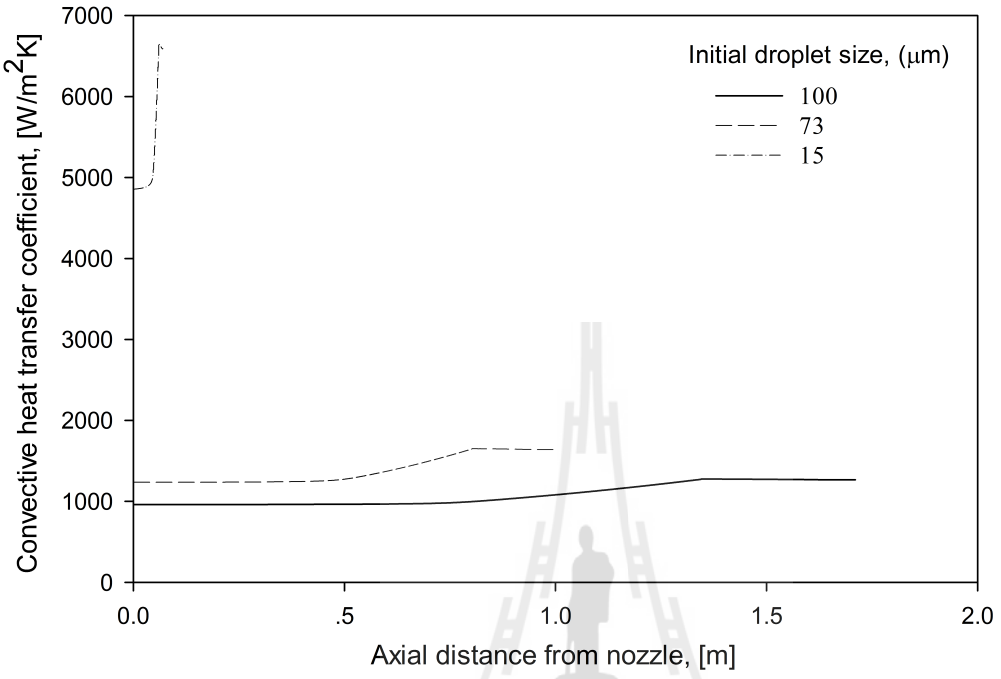

(a)

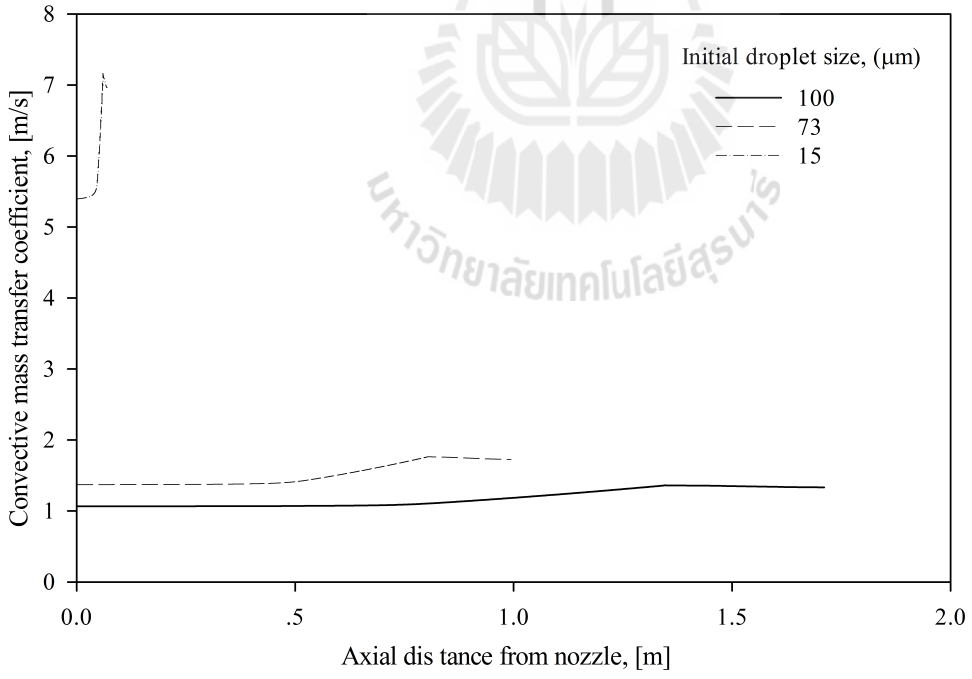

(b)

Figure 82: Profiles of convective (a) heat and (b) mass transfer coefficients in the dryer for droplets of various initial sizes.

to the great amount of water in the droplet, high droplet velocity and declining rate of heat and mass transfer.

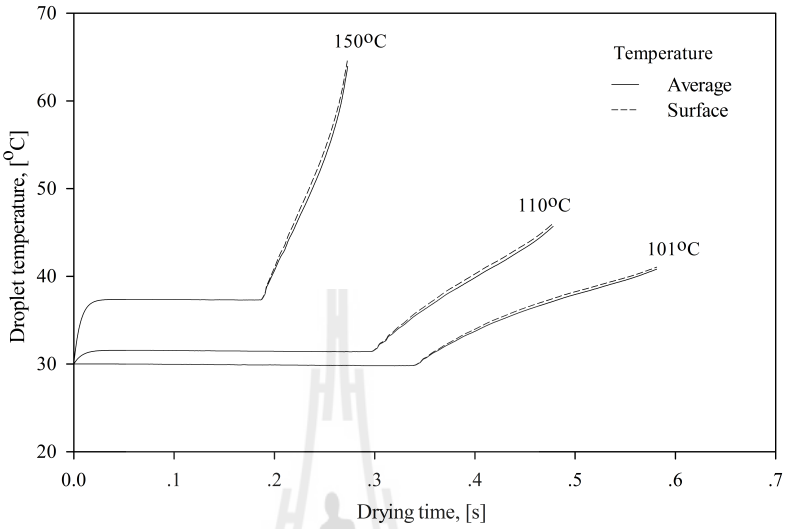

Figure 83: Variations of droplet temperature with drying time for droplets of various initial sizes.

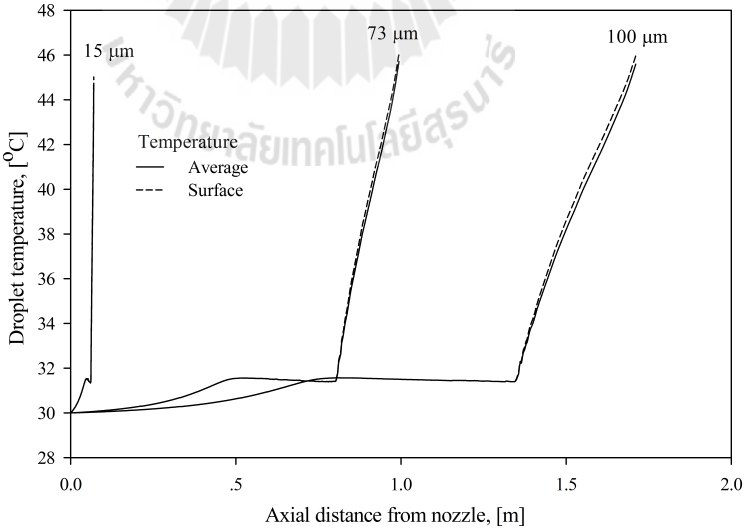

Figure 84: Profiles of average droplet temperatures in the dryer for droplets of various initial sizes.

5.2.7 Effect of nozzle type

The effect of atomizer type on the drying mechanism of slurry droplets in the spray dryer was studied using the rotary and centrifugal-pressure nozzles. The drying conditions, the slurry feed rate and the dryer geometry were identical in both cases. The geometrical and operational parameters of both types of nozzles have been chosen so as to generate droplets of the same Sauter mean diameter of 50 μm.

The droplets leaving a rotary atomizer have two velocity components, radial and tangential, as shown in Fig.85. The droplet tangential velocity rapidly decays in a short axial distance from the nozzle according to the balance of forces in tangential direction. Initially, the radial droplet velocity increases with axial distance due to the contribution of tangential force, then reaches a maximum value at the point of depletion of tangential velocity, and finally decreases owing to the influence of drag force. The droplet axial velocity rises along the axial distance of dryer as a result of contribution of the gravity force and the force exerted on particle by the flowing air.

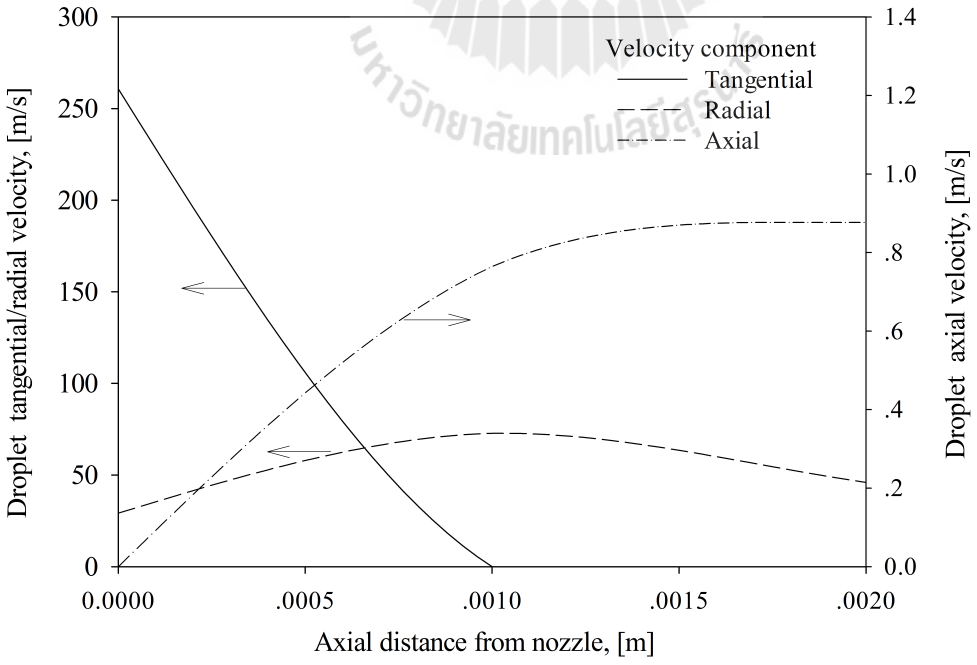

Figure 85: Tangential, radial and axial velocities profiles of droplets generated by rotary nozzle.

Droplets generated by the centrifugal-pressure nozzle also have two initial components of velocity, axial and tangential, as indicated in Fig. 86. The droplet tangential velocity depletes quickly in the axial direction similar to one for droplets formed by the rotary nozzle. The radial velocity profile also resembles closely one generated by the rotary atomizer. The droplet axial velocity does not change significantly along the axial dryer distance due to a large initial velocity.

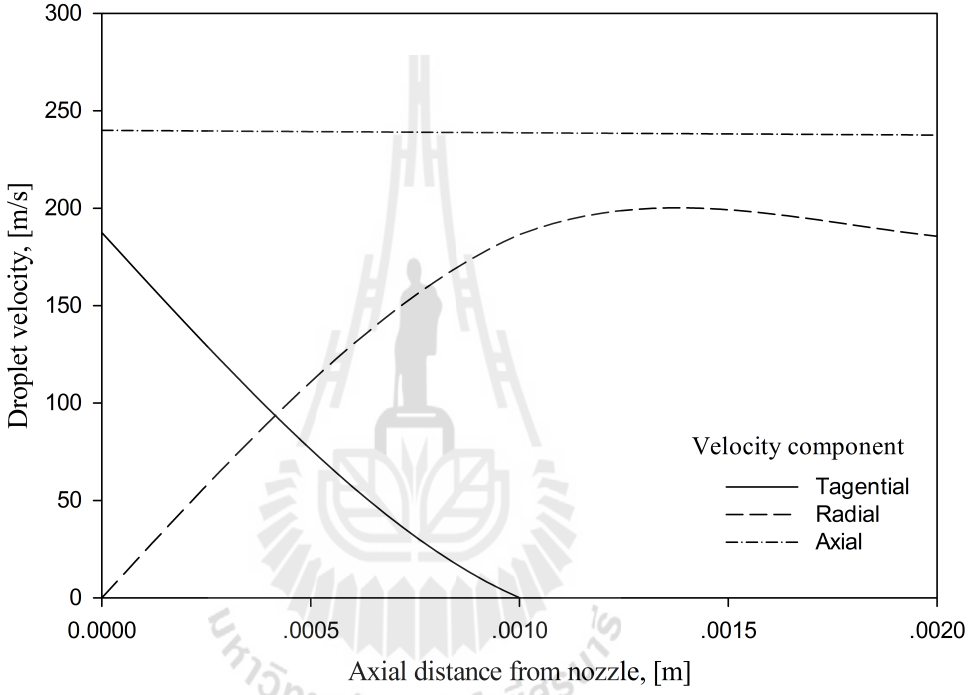

Figure 86: Tangential, radial and axial velocities profiles of droplets generated by centrifugal-pressure nozzle.

Figure 87 illustrates the trajectories of droplets generated by different nozzles. The droplets formed by rotary nozzle travel a longer distance in the radial direction but dry in a shorter distance in the axial direction than those generated by centrifugal-pressure nozzle.

The droplet discharged by rotary nozzle moves very quickly in the radial direction because of great initial velocities in the tangential and radial directions. After the droplet reaches equilibrium, it will fall down due to the gravity and the force applied on the droplet by the flowing air.

The droplets leaving the centrifugal-pressure nozzle form the hollow cone spray as a result of swirling motion of liquid in the nozzle. Since the initial droplet velocity in the axial direction is larger than that in the radial one, droplets move further in the axial direction until the radial velocity component vanishes in comparison with droplets generated by rotary nozzle.

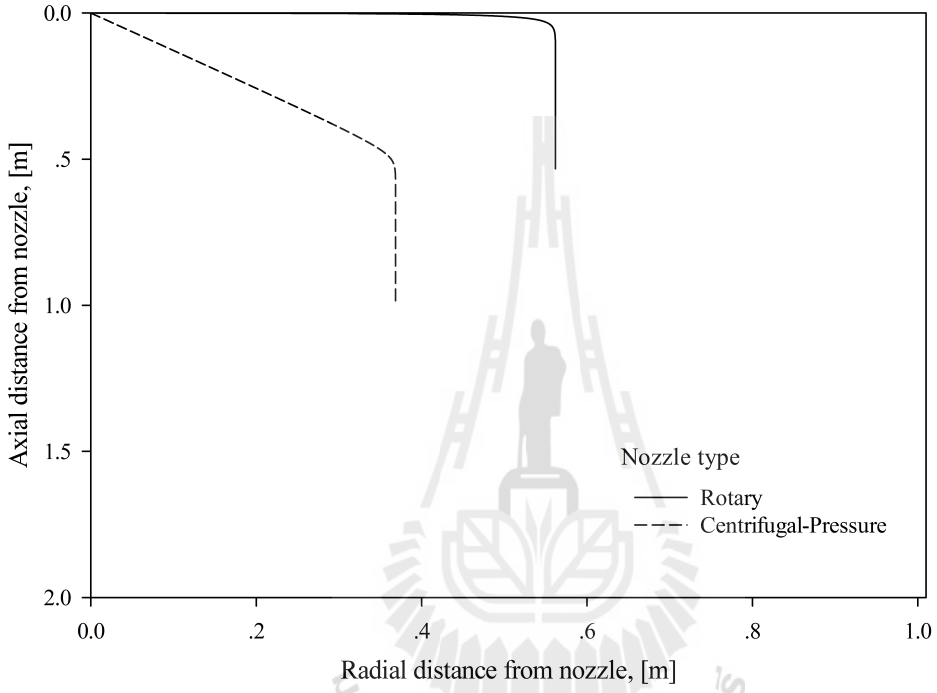

Figure 87: Trajectories of droplets generated by rotary and centrifugal-pressure nozzles.

Therefore, the constant drying rate period starts in a shorter distance from the nozzle for droplets formed by rotary nozzle (0.04 m) than the ones by centrifugal-pressure nozzle (0.48 m). However, droplets generated by both nozzles travel the same axial distances in both constant and falling rate periods, as observed in Fig. 88, because of the similar drying rates at the same drying conditions.

The time variations of average temperature and moisture content of droplets produced by both atomizers are identical in the constant and falling rate periods, as shown in Fig. 89, conforming the equality of drying rates.

The drying rates of droplets generated by rotary and centrifugal-pressure nozzles

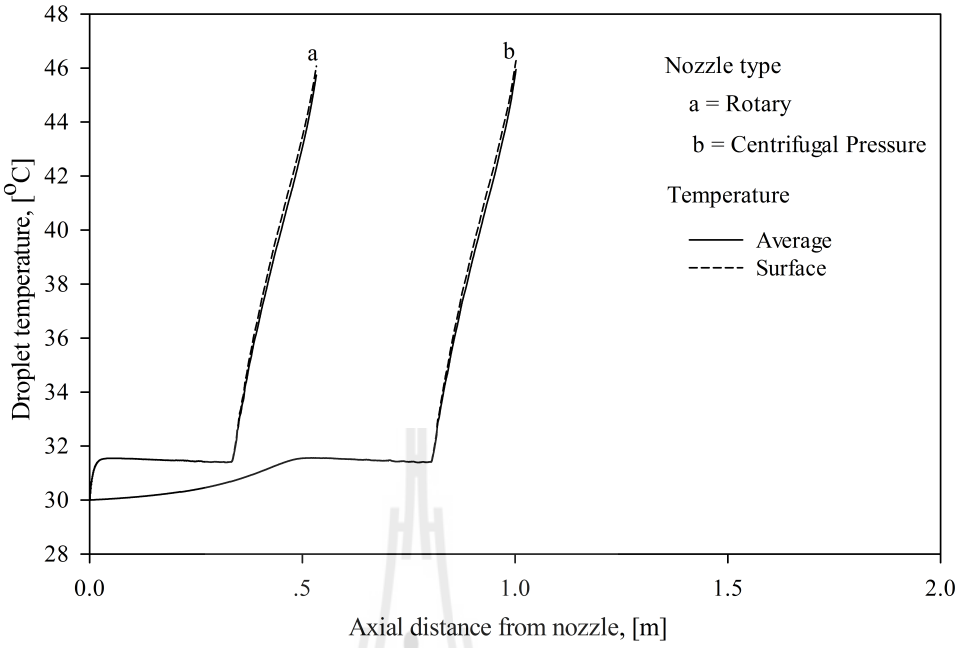

Figure 88: Profiles of average and surface droplet temperatures in the dryer for droplets generated by rotary and centrifugal-pressure nozzles.

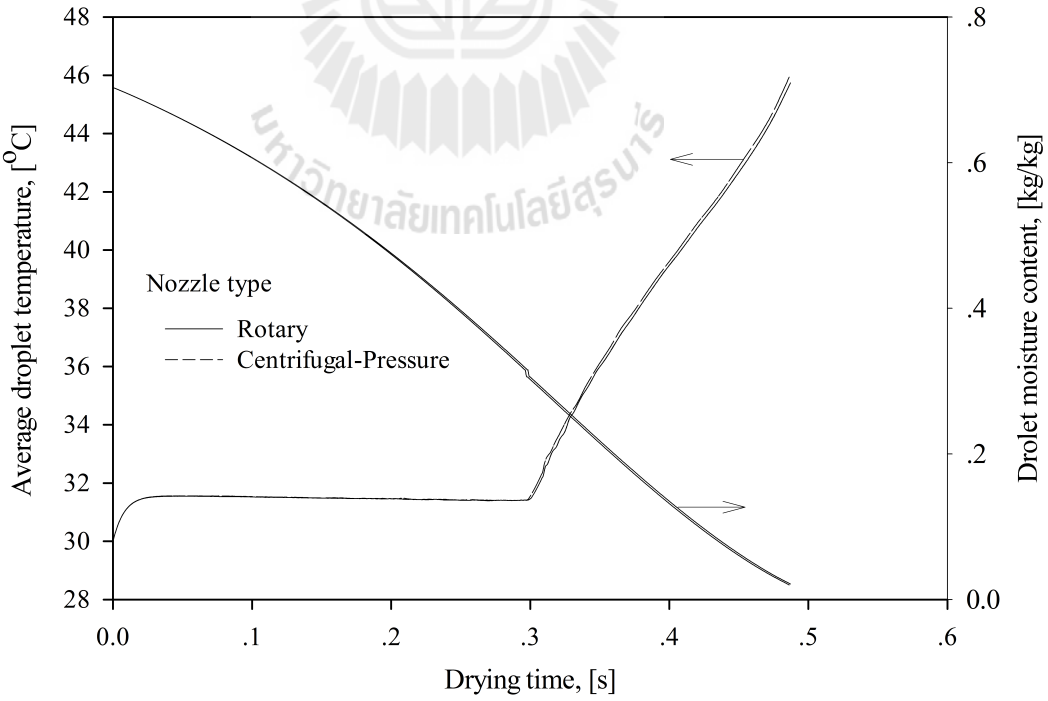

Figure 89: Variations of droplet temperature and moisture content in the dryer for droplets generated by rotary and centrifugal-pressure nozzles.

are similar to each other owing to the resembling rates of change of convective heat and mass transfer coefficients, as illustrated in Figs. 90 (a) and (b).

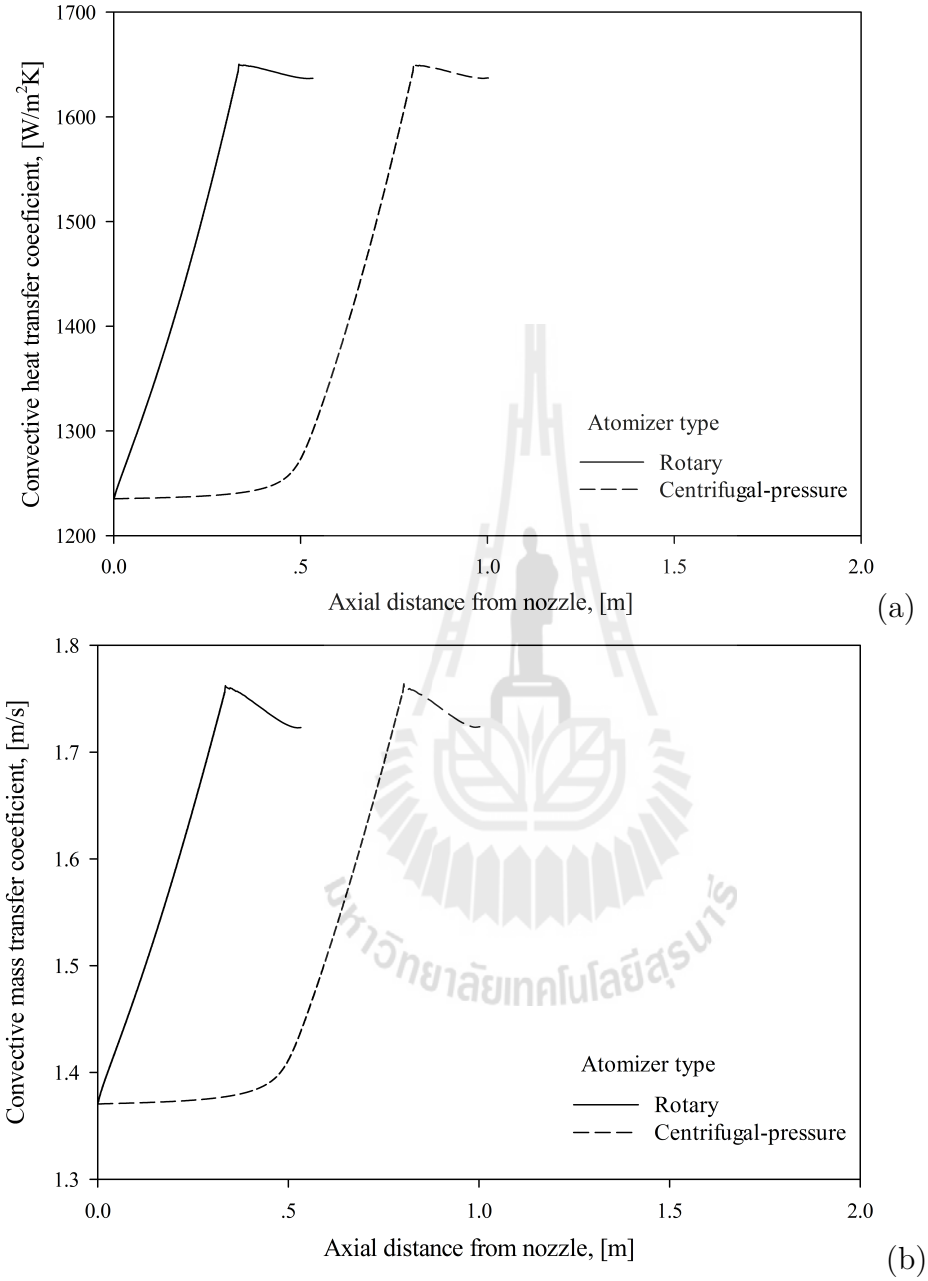

Figure 90: Profiles of convective heat (a) and mass (b) transfer coefficient in the dryer.

The slopes of change of the air temperature, velocity and humidity along the axial distance of spray dryers equipped with rotary and centrifugal-pressure nozzles are also similar in the constant and falling drying periods, as shown in Fig. 91, due to the similar rates of heat and mass transfer.

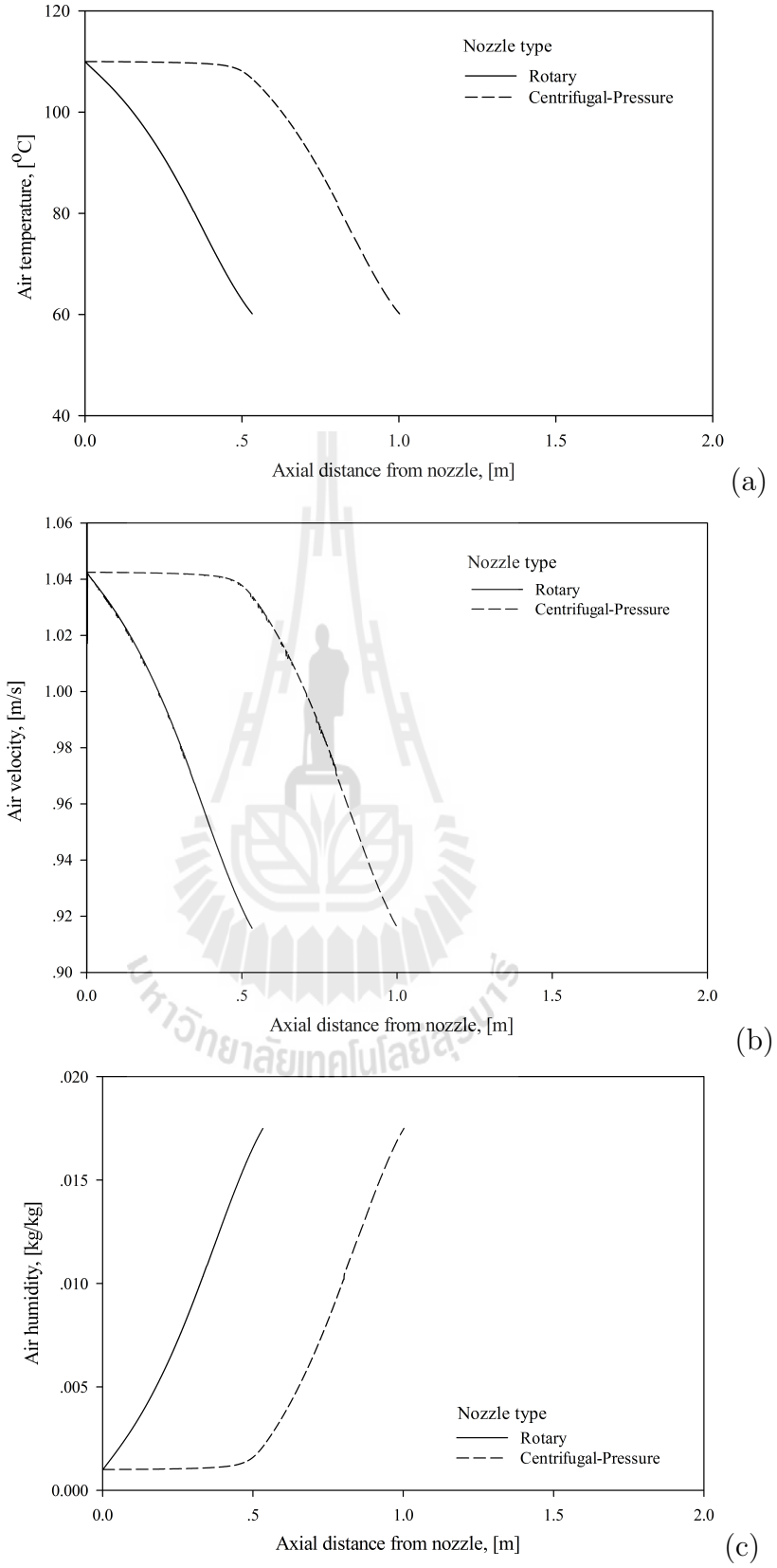

Figure 91: Profiles of air (a) temperature, (b)velocity and (c) humidity in dryers equipped with rotary and centrifugal-pressure nozzles.

5.3 Analysis of spray drying of hydroxyapatite in industrial spray dryer

The objective of this study is to investigate the drying mechanism of high-value particles in an industrial spray dryer. The knowledge of a detailed drying mechanism is essential for selection of operational conditions for production of advanced material. For this purpose, hydroxyapatite is selected as a promising material for a wide range of biomedical and other advanced applications.

In the preceding sections of the present work, the comprehensive drying models of slurry droplets were developed and validated by comparison with experimental data on drying of nanosized silica particles. These models were included in the overall model of spray dryer to explore the effect of process parameters on drying mechanism of silica droplets in a spray dryer. In the present study, the drying mechanism of hydroxyapatite droplets in an industrial spray dryer will be investigated numerically using the developed models and compared with drying mechanism of silica droplets.

The production rate of dried hydroxyapatite product is set at 100 kg/h and the final agglomerate size at 50 μm. An industrial-scale spray dryer was studied with a chamber of total height of 3.730 m consisting of cylindrical, 2.005 m high and 2.215 m in diameter, and conical sections. The slurry feed is supplied to the chamber concurrently with a drying air and a centrifugal-pressure nozzle is used for droplet generation. The operational parameters are summarized as follows: the drying air mass flow rate was set at 3.7 kg/s, drying air temperature at 110 °C, drying air humidity at 0.001 kg/kg, slurry concentration at 30 wt.

Figure 92 shows the droplet trajectories in the dryer. The simulation results confirm that drying of hydroxyapatite slurry can successfully be accomplished in the present industrial-scale spray dryer to produce the final agglomerates of 50 micron under the drying conditions summarized above. The drying of droplets will be finished in short radial and axial distances in the chamber thus avoiding contact of moist droplets

with a side wall of cylindrical and a bottom wall of conical sections and subsequent build-up of deposit.

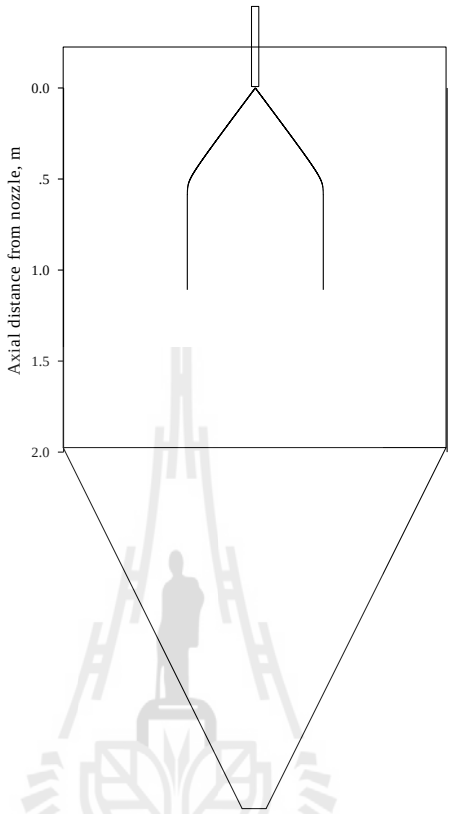

Figure 92: Trajectories of hydroxyapatite droplets in the dryer.

The silica product particles of the same size and porosity as hydroxyapatite ones are selected for comparison purposes. However, the droplets of hydroxyapatite and silica are of different initial sizes because of the dissimilar material densities. The density of silica is 2220 kg/m^3 and that of hydroxyapatite 2462 kg/m^3. The initial size of droplets $d_{p,init}$ is evaluated by fixing the slurry concentration C_{sl}, porosity ε and radius of final product r_{fp} as

$$d_{p,init} = 2r_{fp}\left[(1-\varepsilon) + \frac{\rho_s\,(1-\varepsilon)}{\rho_w}\left(\frac{100}{C_{sl}} - 1\right)\right]^{\frac{1}{3}} \tag{192}$$

A hydroxyapatite droplet is of larger initial size and it contains a larger amount of water than that of silica. As a result, the hydroxyapatite droplets are dried in a longer axial distance in the dryer in comparison with silica droplets, as illustrated in

Fig. 93.

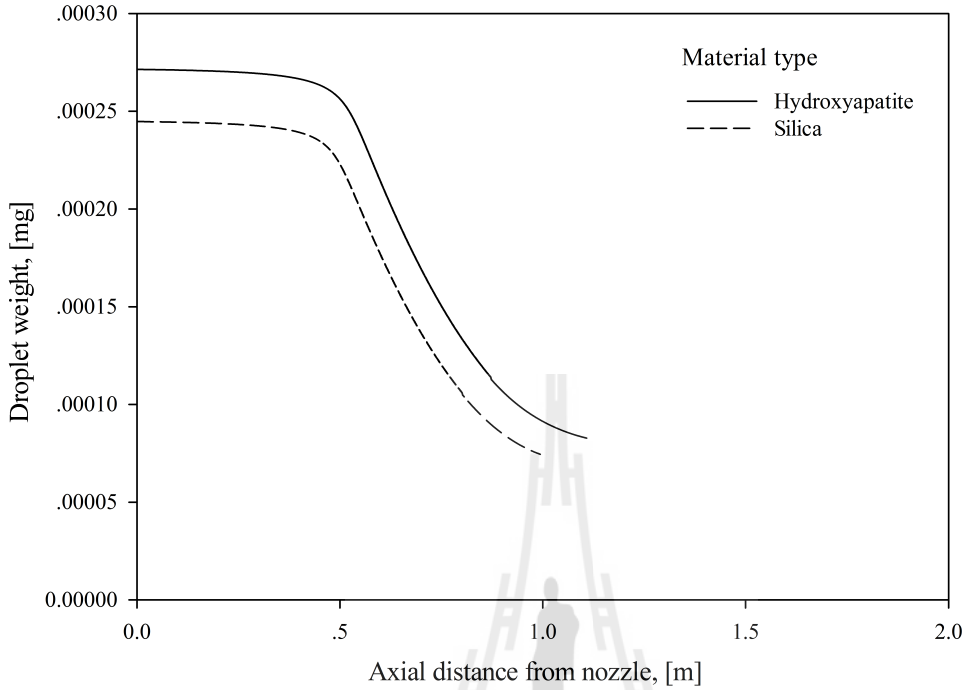

Figure 93: Profiles of weight losses of hydroxyapatite and silica droplets in the axial direction of spray dryer.

The relative velocities of droplets of both material types bit differ in the initial heating-up period, but the difference vanishes in the constant and falling rate periods, as illustrated in Fig. 94. Therefore, the effect of relative velocity can be neglected on the convective heat and mass transfer from the drying air to the droplet outer surface.

The droplets of both materials are of the same initial moisture contents specified by inlet slurry concentration. However, the moisture content of silica droplet decreases faster than that of hydroxyapatite droplet in the constant and falling rate periods, as illustrated in Fig. 95, due to the high rate of convective heat and mass transfer between droplets and drying air. In the constant rate period, the rate of heat and mass transfer is high due to the small size of silica droplets. Although the droplet sizes of both materials are identical in the falling rate period, the enhanced rate of heat and mass transfer in case of silica particles can be attributed to the high air temperature owing to the low energy consumption on evaporation of small amount of

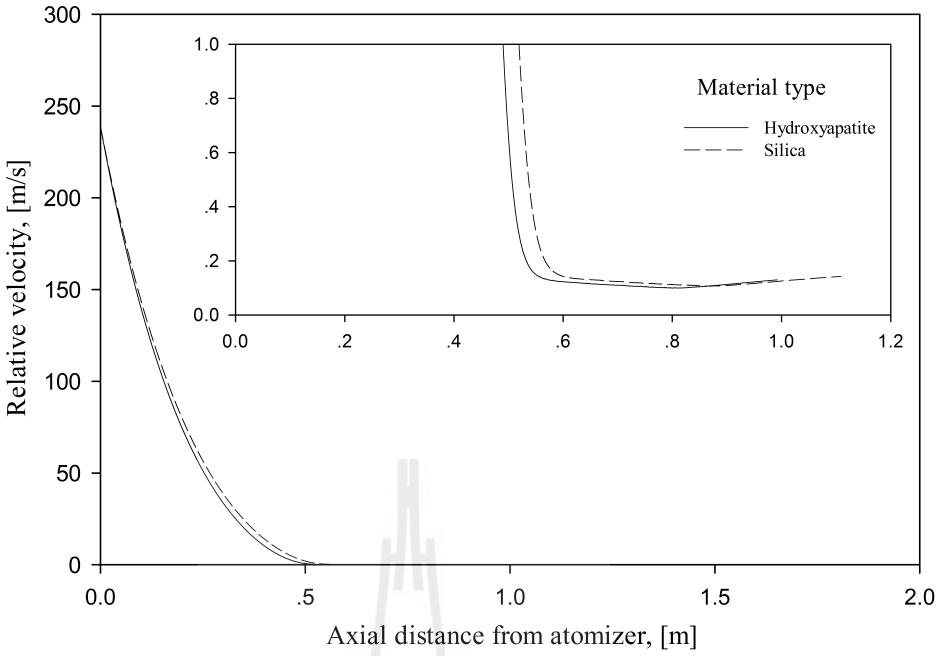

Figure 94: Profiles of relative velocities of hydroxyapatite and silica droplets in the axial direction of spray dryer.

water in the droplet.

The air temperature decreases and humidity increases more slowly during drying of hydroxyapatite droplets than in case of silica, as indicated in Fig. 96. These results also confirms the lower rate of heat and mass transfer between the drying air and hydroxyapatite droplets. The larger humidity and higher temperature of outlet air in the drying of hydroxyapatite droplets results from the higher initial amount of water in the droplet in comparison with drying of silica droplets.

The hydroxyapatite droplets travel a longer axial distance in the dryer than silica droplets in the constant rate period due to the lower rate of heat and mass transfer of large droplets and larger amount of water to be evaporated during drying, as shown in Fig. 97. In the falling rate period, the rate of average temperature increase of hydroxyapatite droplet is slower than that of silica owing to the low rate of heat and mass transfer by low air temperature. The difference of average and surface temperatures in case of hydroxyapatite droplets is significantly larger than that of silica due to the difference in thermal properties of solid materials.

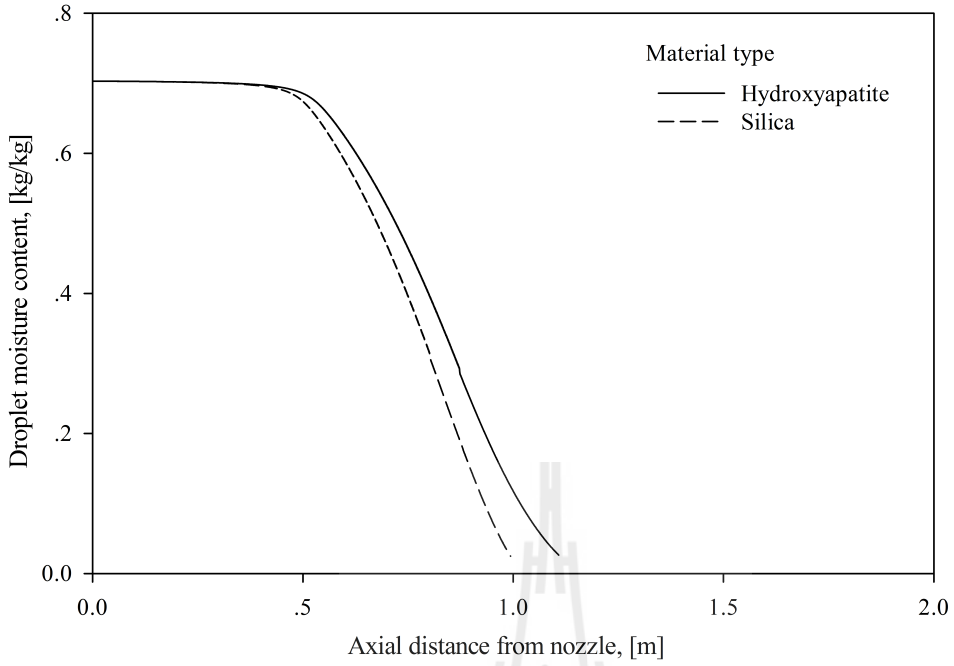

Figure 95: Profiles of moisture content of hydroxyapatite and silica droplets in the axial direction of spray dryer.

A high heat capacity and low thermal conductivity of hydroxyapatite in comparison with silica, as illustrated in Fig. 98, lead to the low rate of heat transfer from the outer droplet surface to evaporation interface by conduction through the crust layer and considerable heat accumulation in dry crust which results in a high surface temperature.

The temperature difference between the outer surface of hydroxyapatite droplet and evaporation interface is significantly larger than the one in the silica droplet, as shown in Fig. 99 for the same crust layer thicknesses. An appreciable heat transfer resistance in the crust layer of hydroxyapatite droplet may account for large temperature difference and high droplet surface temperature due to the low thermal conductivity.

The concentration profiles of water vapor in the dry crust layer of droplets are shown in Fig. 100. The concentration of water vapor at the evaporation interface of hydroxyapatite droplet is lower than that of silica droplet due to the low rate of water evaporation associated with the low heat supply to evaporation interface. A high crust temperature of hydroxyapatite leads to a high rate of mass transfer through the

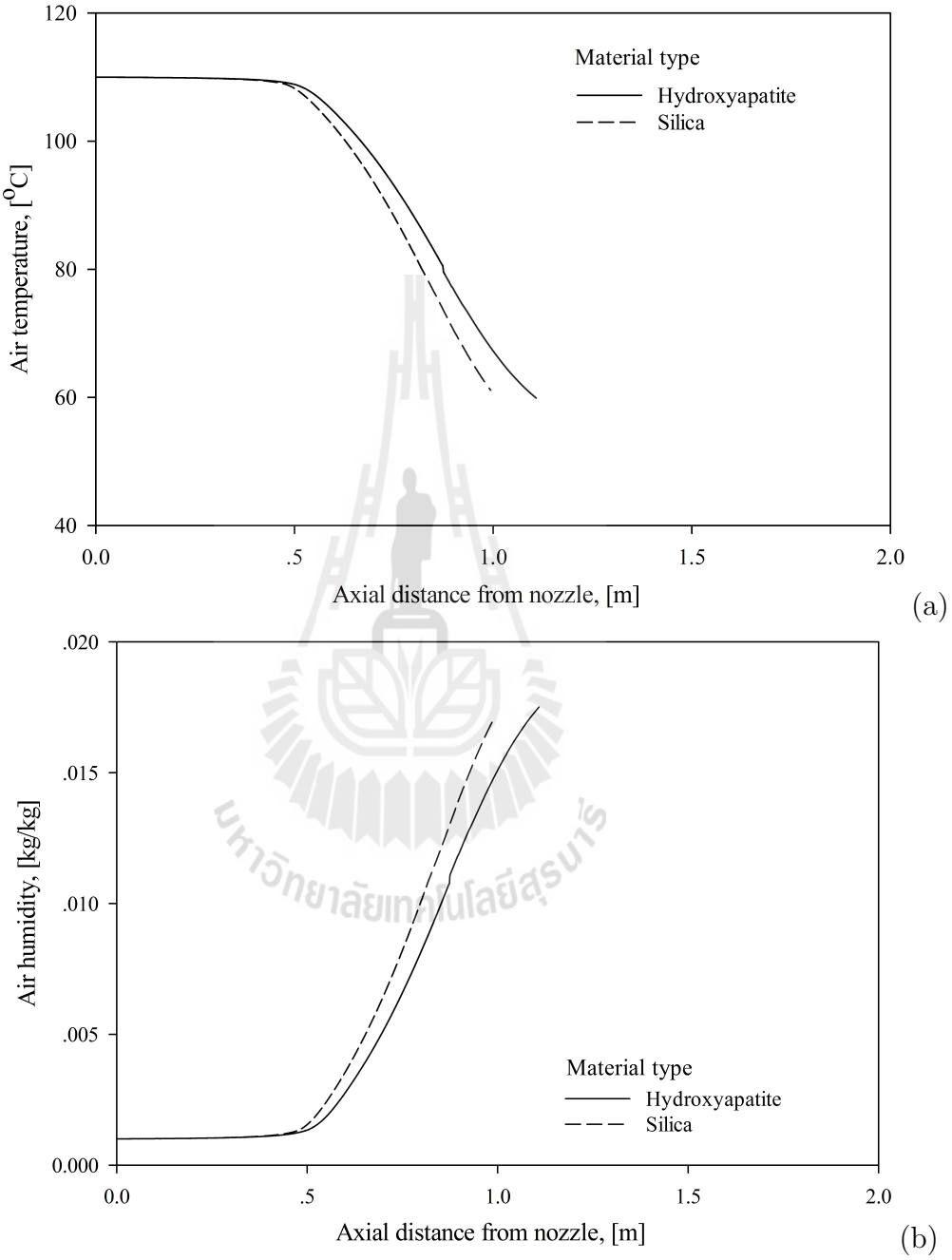

Figure 96: Profiles of air (a) temperature and (b) humidity in spray drying of hydroxyapatite and silica droplets.

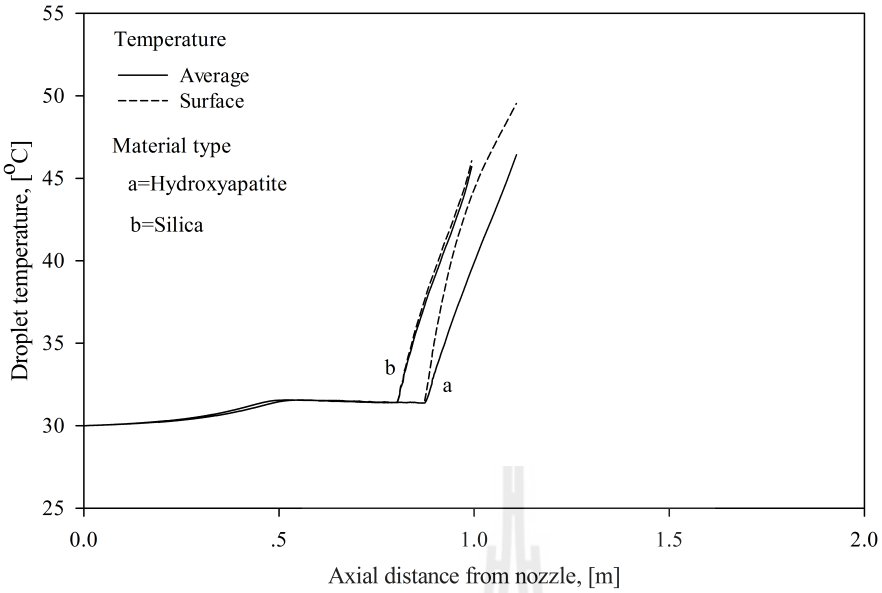

Figure 97: Profiles of average and surface temperatures of hydroxyapatite and silica droplets in spray dryer.

dry crust resulting in the lower water vapor concentration at the same thickness of dry crust.

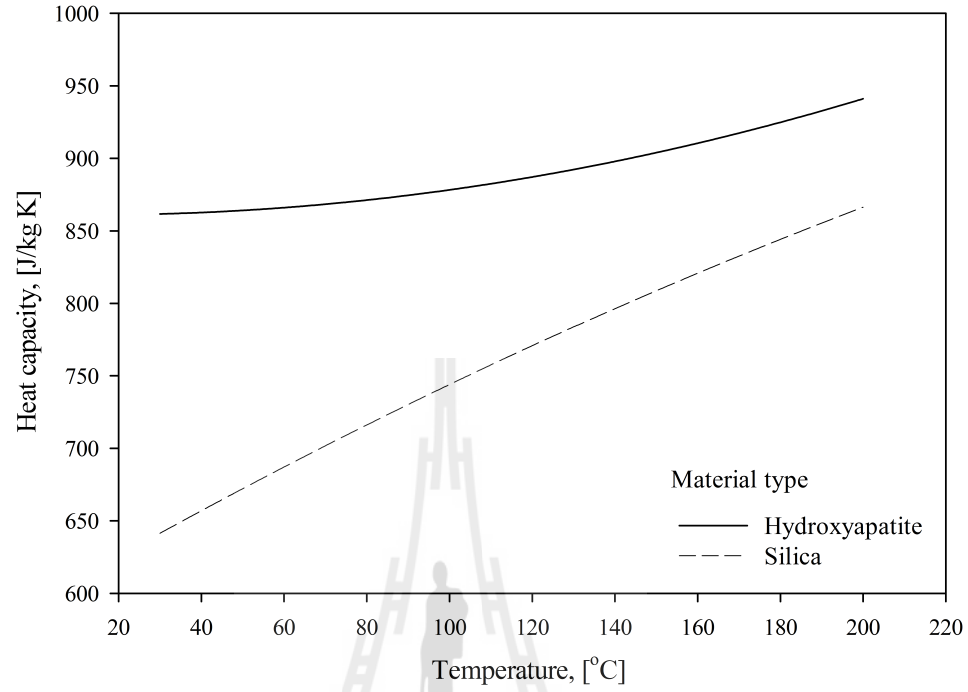

(a)

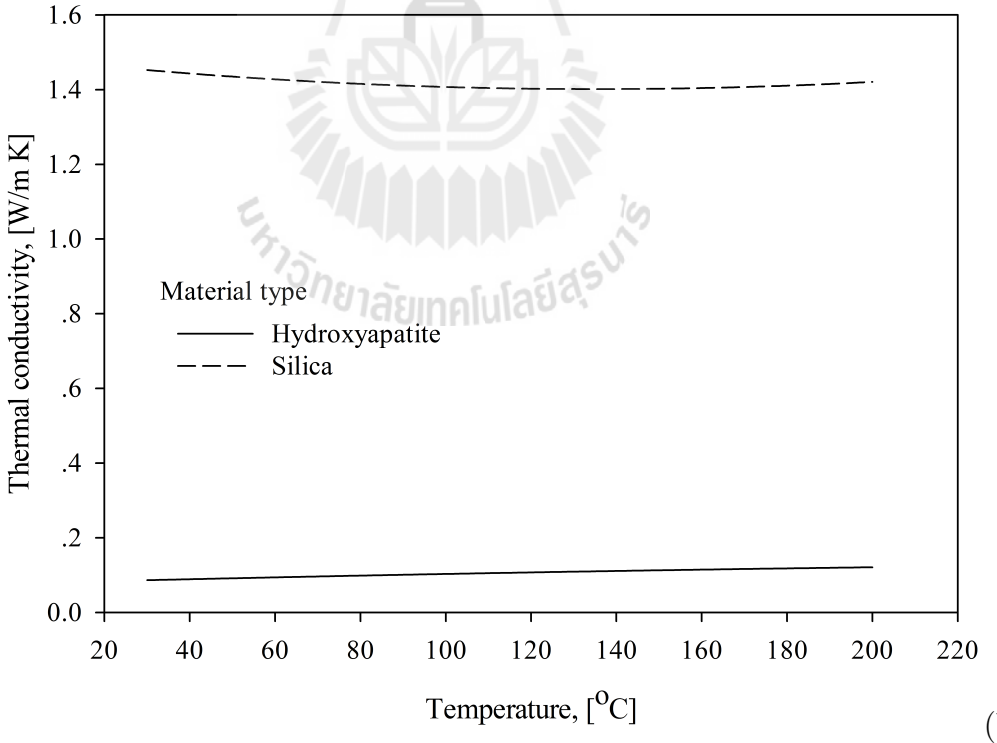

(b)

Figure 98: Profiles of convective heat (a) and mass (b) transfer coefficient in spray drying of hydroxyapatite and silica droplets.

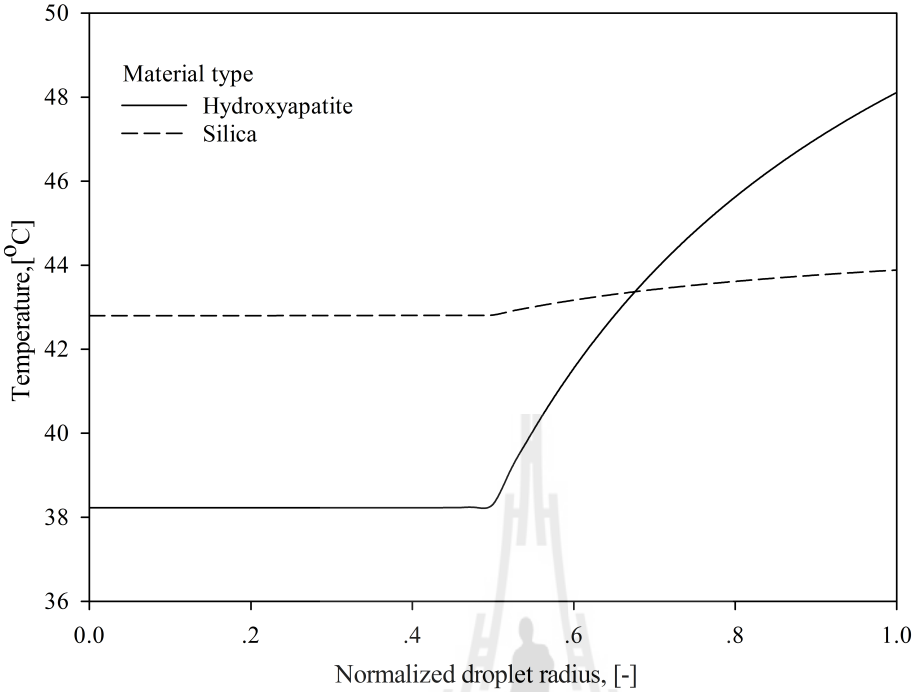

Figure 99: Temperature distributions in hydroxyapatite and silica droplets.

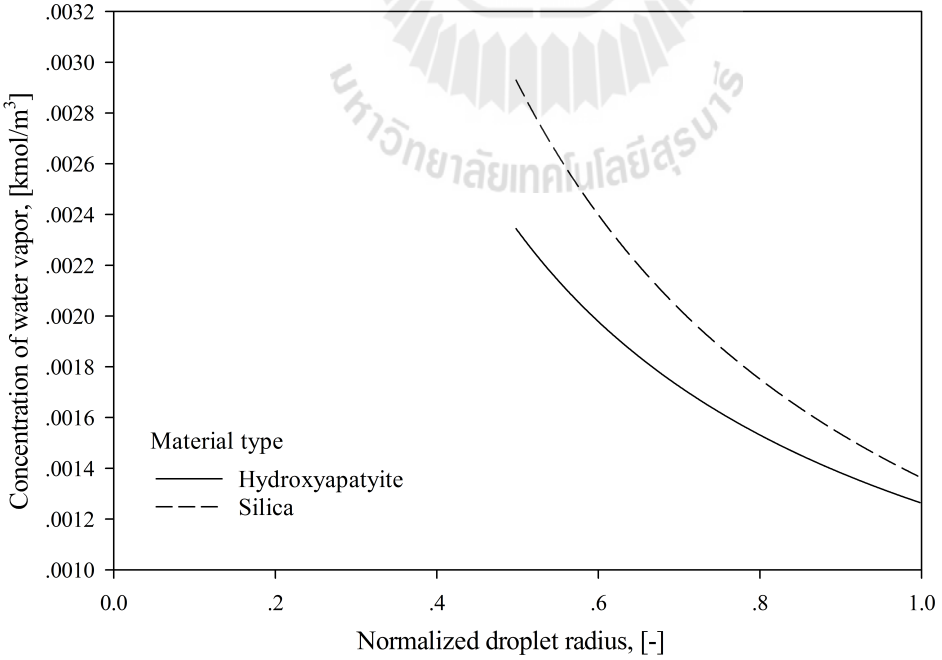

Figure 100: Concentration distributions of water vapor in hydroxyapatite and silica droplets.

6 Conclusions

The research aim of this project was to analyze the drying mechanism of slurry droplets in an industrial scale spray dryer for production of high-value particles. For this purpose, a mathematical model was developed comprising a comprehensive model for the heat and mass transfer for a single droplet and a model for the flow of droplets and gas, and the heat transfer and mass transfer in the dryer.

Using the developed model, the drying behavior of a single slurry droplet was investigated in the first part of this project. The detail analysis was carried out on effects of wide range of operational conditions and particle morphology on the drying of a slurry droplet. In the second part, the drying mechanism of slurry droplets was explored in the industrial scale dryer. The influences of operational parameters and a nozzle type were examined on the drying behavior of droplets. Finally, the formation of hydroxyapatite agglomerates, as an example of high-value particles, was studied by spray drying.

Drying kinetics of a slurry droplet

The comprehensive model was established for description of the drying kinetics of a slurry droplet in the constant and falling rate periods. This model accounts for the heat and mass transfer resistances both inside and outside the droplet as well as the movement of evaporation interface as drying progresses. The resulting system of partial differential equations with moving boundary was solved numerically.

The model is capable to predict profiles of temperature and vapor concentration in the radial direction of the droplet along with the average and surface droplet temperatures, and the droplet weight and moisture content over the course of drying.

The model was validated by comparison of simulation results with experimental data on drying of a droplet of colloidal silica nanoparticles. The computer simulation studies were conducted on the effects of the drying air temperature, air feed rate, slurry concentration, initial droplet temperature, particle diameter and porosity of

agglomerated product on a slurry droplet drying.

Major conclusions resulting from the analysis of mechanism of drying of a slurry droplet are summarized as follows:

- Numerical simulations of a slurry droplet drying were in good agreement with experimental results confirming the validity of the developed advanced drying model.
- The drying rate of a slurry droplet was governed by the heat and mass transfer resistances outside the droplet in the constant rate period and by resistances both inside and outside the droplet in the falling rate period.
- The droplet drying rate increased significantly with increasing the temperature of drying air, air flow rate and slurry concentration, and with decreasing the agglomerate size.
- The loose agglomerate was dried over a longer period of time in comparison with the dense one. The average temperature of dense agglomerate was higher than that of loose one during the falling-rate period. The heat transfer through the crust layer by conduction was more profound in the case of the dense layer. However, the mass transfer was accelerated in the crust layer of high porosity.
- The agglomerate surface, dry crust and wet core temperatures, and the temperature difference between the agglomerate surface and the wet core increased with drying time during the falling rate period. The accumulation of water vapor in the crust also enhanced during drying.

Drying mechanism of slurry droplets in spray dryer

A mathematical model was developed for spray drying of slurry droplets in the industrial scale spray dryer. The dryer model combines a droplet model for the heat and mass transfer for a single droplet, an atomizer model for the droplet velocities leaving the nozzle, and a chamber model for the flow of droplets and drying gas,

and the heat and mass transfer in the spray dryer chamber. The present model can be used to predict the profiles of droplet average temperature, moisture content and velocities, and air temperature, humidity and velocities along the axial distance of the dryer as well as the distributions of temperature and water vapor concentration inside the droplet at any axial position in the dryer.

The effects of operational parameters such as the drying air temperature and flow rate, slurry concentration and droplet size as well as the nozzle type were investigated on the drying behavior of slurry droplets of nanosized silica in the spray dryer.

The main results of the analysis of slurry drying in the spray dryer are summarized as follows:

- The average droplet temperature increased rapidly up to the wet bulb temperature during the initial heating-up period.

  The air temperature quickly decreased and humidity increased, but the average droplet temperature remained constant in the axial direction of the dryer during the constant rate period. The temperature distribution in the droplet was nearly uniform.

  The rates of change of the air temperature increased and humidity declined, and the average droplet temperature rose in the falling rate period. As a result, the temperature and vapor concentration differences between the outer droplet surface and the evaporation interface expanded with drying time.

- The drying was completed in a short axial distance in the dryer for the droplets of small initial size and the concentrated slurry, and using the hot inlet air.

  The drying was accomplished over a short period of time for the small droplets and the concentrated slurry, and using the inlet air at high temperature and flow rate.

- The temperature of air in the dryer increased with increasing the inlet air flow rate and temperature.

The air humidity was low during drying of concentrated slurry at high air feed rate.

The high velocity air stream was generated in axial direction of the dryer at high inlet air flow rate and temperature, and using the concentrated slurry.

- The average droplet temperature in the constant rate period remained constant at the wet bulb temperature. In the falling rate period, the high average droplet temperature was observed at high air feed rate and temperature, and for concentrated slurry.

  The droplet moisture content decreased rapidly up to the desired moisture content by increasing the air feed rate and temperature, slurry concentration and also by using droplets of small initial sizes.

- The heat transfer resistance and the accumulation of water vapor inside the droplet declined by decreasing the air feed rate and temperature, and slurry concentration.

- The droplets formed by the rotary nozzle travelled a longer distance in the radial direction but they were dried in a shorter distance in the axial direction than those generated by the centrifugal-pressure nozzle.

  The time variations of average temperature and moisture content of droplets produced by both atomizers are identical in the constant and falling rate periods, because of the similar drying rates at the same drying conditions.

Drying mechanism of high value particles in spray dryer

The drying mechanism of high-value particles of hydroxyapatite in an industrial spray dryer was investigated numerically using the developed models and compared with the drying mechanism of silica droplets of the same final size. Hydroxyapatite was selected as a promising material for a wide range of biomedical and other advanced applications.

The conclusions resulting from the analysis of mechanism of slurry drying of a high value material are summarized as follows:

- The simulation results confirmed that drying of hydroxyapatite slurry can successfully be accomplished in the present industrial scale spray dryer to produce final agglomerates of 50 micron without contact of partially dried particles with dryer wall.

- Similar mechanisms were observed for the drying of hydroxyapatite and silica slurry droplets, but the rate of heat and mass transfer between air and droplets was lower in the case of drying of hydroxyapatite droplets.

  The heat transfer resistance and heat accumulation in the dry crust of hydroxyapatite were larger than in silica material.

- The air temperature decreased and humidity increased more slowly during drying of hydroxyapatite droplets than in the case of silica.

- The hydroxyapatite droplets are dried in a longer axial distance in the dryer in comparison with silica droplets.

  The moisture content of silica droplet decreases faster than that of hydroxyapatite droplet in the constant and falling rate periods.

  The difference of average and surface temperatures is significantly larger in the case of hydroxyapatite droplets than that of silica due to the difference in thermal properties of solid materials.

- The temperature difference between the outer droplet surface and evaporation interface is considerably larger in the hydroxyapatite droplets than the one in the silica droplets.

  The accumulation of water vapor concentration in the dry crust of hydroxyapatite was lower than in silica material at the same crust thickness.

มหาวิทยาลัยเทคโนโลยีสุรนารี

References

Araujo R.R., Teixeira C.C.C. and Freitasa L.A.P., The preparation of ternary solid dispersions of an herbal drug via spray drying of liquid feed, *Drying Technology*, **28**, 412-421, 2010.

Archie G.E., The electrical resistivity log as an aid in determining some reservoir characteristics, *Trans. AIME*, **46**, 4561, 1942.

Ameri M. and Maa Y.-F., *Drying Technology*, **24**, 763-768, 2006.

Bhushan B., (Ed.) Springer handbook of nanotechnology, pp. 1916, 2007.

Chan H.K., Dry powder aerosol drug delivery opportunities for colloid and surface scientists, *Colloids and Surfaces A: Physicochemical and Engineering Aspects*, **284-285**, 50-55, 2006.

Charlesworth D. H. and Marshall W. R., Evaporation from drops containing dissolved solids, *AIChE Journal*, **6**, 9-23, 1960.

Chiou D., Langrish T.A.G. and Braham, R., Partial crystallisation behaviour during spray drying: simulations and experiments, *Drying Technology*, **26**, 27-38, 2008.

Crowe C.T., Modelling spray-air contact in spray-drying systems. In: Mujumdar, A.S. (Ed.), *Advances in Drying*, vol. **1**, Hemisphere, New York, pp. 63-99, 1980.

Dalmaz N., Ozbelge H. O., Eraslan A. N. and Uludag Y., Heat and mass transfer in drying of a suspension droplet: A new computational model, *Drying Technology*, **25**, 391-400, 2007.

Elperin T. and Krasovitov B., Evaporation of liquid droplets containing small solid particles, *Int. J. Heat Mass Transfer*, **38**, 2259-2267, 1995.

Farid M., A new approach to modelling of single droplet drying, *Chemical Engineering Science*, **58**, 2985-2993, 2003.

Holterman H.J., Kinetics and evaporation of water drops in air, IMAG, Wageningen, Report no. 2003-12, 67 pp., 2003.

Huang L.X. and Mujumdar A.S., Classification and selection of spray dryers, *Chemical Industry Digest*, **7-8**, 75-84, 2003.

Iskandar F., Nanoparticle processing for optical applications - a review, *Advanced Powder Technology*, **20**, 283-292, 2009.

Iskandar F., Lenggoro I.W., Xia B. and Okuyama K., Functional nanostructured silica powders derived from colloidal suspensions by sol spraying, *Journal of Nanoparticle Research*, **3**, 263-270, 2001.

Iskandar F., Nandiyanto A.B.D., Yun K.M., Hogan C.J., Okuyama K. and Biswas P., Enhanced photocatalytic performance of brookite TiO2 macroporous particles prepared by spray drying with colloidal templating, *Advanced materials*, **19**, 1408-1412, 2007.

Kaewpanha M., Lauruengtana V., Furuta T., Charinpanitkul T., Ruktanonchai U., Tanthapanichakoon W., Yoshii H. and Soottitantawat A., Encapsulation of lemongrass oil with modified starch by spray drying, in *CERT proceedings of research progress 2010*, Chulangkorn University, 51-54, 2010.

Keey R.B., Introduction to Industrial Drying Operations, Pergamon, Oxford, pp. 15-99, 1978.

Keey R.B. and Pham Q.T., Behaviour of spray dryers with nozzle atomizers, *Chemical Engineer* (London), **311**, 516-521, 1976.

Kieviet, F.G, Modeling Quality in Spray Drying, PhD thesis, Endinhoven University of Technology, Netherlands, 1997.

King C.J., Kieckbusch T.G. and Greenwald C.G., 1984. Food-quality factors in spray drying. In: *Advances in drying*, Ed. A.S. Mujumdar, Hemisphere, New York, Vol. **1**, 71-120.

Klinkulabhira S. et al., *CERT proceedings of research progress 2010*, Chulangkorn University, 73-75, 2010.

Kuts P.S., Strumillo C. and Zbicinski I., Evaporation kinetics of single droplets containing dissolved biomass, *Drying Technology*, **14**, 2041-2060, 1996.

Lam C.W., James J.T., McCluskey R., Arepalli S. and Hunter R.L., A review of carbon nanotube toxicity and assessment of potential occupational and environmental health risks, *Critical reviews in toxicology*, **36**, 189-217, 2006.

Langrish T., New engineered particles from spray dryers: Research needs in spray drying, *Drying technology*, **25**, 981-993, 2007.

Masters K., Spray drying handbook: Longman, 1985.

K. Masters, Spray drying in practice, SprayDryConsult Intl., Denmark, 2002.

K. Masters, Applying spray drying to customised powder manufacture, *Chinese J. Chem. Eng.*, **12**, 744749, 2004.

Mezhericher M., Levy A. and Borde I., Theoretical Models of Single Droplet Drying Kinetics: A Review, *Drying technology*, **28**, 278-293, 2010.

Mujumdar A.S., Handbook of industrial drying: CRC Press, 2007.

Nesic S., The evaporation of single droplets-experiments and modeling, *Drying' 89*, 386-393, 1990.

Nesic, S. and Vodnik J., Kinetics of droplet evaporation, *Chemical Engineering Science*, **46**, 527-537, 1991.

Oakley D.E., Bahu R.E. and Reay D., The aerodynamics of concurrent spray dryers, In: Roques M. (Ed.), Proceedings of the Sixth International Drying Symposium (IDS 88) (pp. OP 373-OP 378), September, Versailles, France, 1988.

Oakley D.E. , Scale-up of spray dryers with the aid of computational fluid dynamics, *Drying Technology*, **12**, 217-233, 1994.

Ochoa-Tapia J.A., Stroeve P. and Whitaker S., Diffusive transport in two-phase media: Spatially periodic models and Maxwell's theory for isotropic and anisotropic systems, *Chemical Engineering Science*, **49**, 709-726, 1994.

Okuyama K., Abdullah M. , Lenggoro I.W. and Iskandar F., Preparation of functional nanostructured particles by spray drying, *Advanced Powder Technology*, **17**, 587-611, 2006.

Ozmen L. and Langrish T.A.G., A study of the limitations to spray dryer outlet performance, *Drying Technology*, **21**, 895-917, 2003.

Pakowski Z. and Mujumdar A.S., Basic process calculations in drying, in *Handbook of industrial drying*: CRC Press, pp. 71-112, 1995.

Parti M. and Palancz B., Mathematical model for spray drying, *Chemical Engineering Science*, **29**, 355-362, 1974.

Pearce D.L., A novel way to measure the concentration of a spray in a spray dryer, *Drying Technology*, **24**, 777-781, 2006.

Place G., Ridgway K. and Danckwerts P.V., Investigation of air-flow in a spray drier by tracer and model techniques, *Transactions of the Institution of Chemical Engineers*, **37**, 268-276, 1959.

Ranz W.E. and Marshall W.R., Evaporation from drops, *Chemical Engineering Progress*, **48**, 141-146, 1952.

Re M.I., Formulating drug delivery systems by spray drying, *Drying Technology*, **24**, 433-446, 2006.

Reay, D., Fluid flow, residence time simulation and energy efficiency in industrial dryers, In: Roques, M. (Ed.), Proceedings of the Sixth International Drying Symposium (IDS 88) (pp. KL.1-KL.8). September, Versailles, France, 1988.

Revised Release on the IAPWS Industrial Formulation 1997 for the Thermodynamic Properties of Water and Steam. The International Association for the Properties of Water and Steam, 2007.

Riveros B., Ferrera J. and Borquez R., Spray drying of a vaginal probiotic strain of lactobacillus acidophilus, *Drying Technology*, **27**, 123-132, 2009.

Singkhimuk S., Ruktanonchai U. and Soottiantawat A., Microencapsulation of extracted cintronella oil with rice starch by spray drying, in *CERT proceedings of research progress 2010*, Chulangkorn University, 76-80, 2010.

Strumillo C. and Kudra T., In: Drying: Principles, Application and Design, Gordon and Breach, New York, pp. 45-54, 1986.

Suh W.H., Jang A.R., Suh Y.H. and Suslick K.S., Porous, hollow, and ball-in-ball metal oxide microspheres: preparation, endocytosis, and cytotoxicity, *Advanced Materials*, **18**, 1832-1837, 2006.

Tavman I.H., Effective thermal conductivity of granular porous materials, *Int. Comm. Heat Mass Transfer*, **23**, 169 -176, 1996.

Truong V., Bhandari B.R. and Howes T., Optimization of co-current spray drying process of sugar-rich foods. Part I Moisture and glass transition temperature profile during drying, *Journal of Food Engineering*, **71**, 55-65, 2005.

Wang S. and Langrish T., A review of process simulations and the use of additives in spray drying, *Food Research International*, **42**, 13-25, 2009.

Woodside W. and Messmer J. H. , Thermal conductivity of porous media. I. Unconsolidated sands, *J. Appl. Phys.*, **32**, 1688, 1961.

Zbicinski I., Development and experimental verification of momentum, heat and mass transfer model in spray drying, *Chemical Engineering Journal*, **58**, 123-133, 1995.

Zhou B., Balee, R. and Groenendaal R., Nanoparticle and nanostructure catalysts: technologies and markets. *Nanotechnology Law and Business*, **2**, 222-229, 2003.

List of Publications and Conference Contributions Related to this Research Project

Publications in Referred International Journals

W. Julklang, B. Golman, Influence of Operational Conditions on the Drying Kinetics of a Slurry Droplet in a Spray Dryer, Engineering Transactions, Vol. 15, No. 2, 59 - 65 (2012).

B. Golman, W. Julklang, Analysis of Drying Kinetics of a Slurry Droplet in the Falling Rate Period of Spray Drying, World Academy of Science, Engineering and Technology, International Science Index 81, International Journal of Chemical Science and Engineering, Vol. 7, No. 9, 786 - 791 (2013).

W. Julklang, B. Golman, Analysis of Slurry Drying in a Spray Dryer, International Journal of Engineering and Technology, Vol. 6, No. 6, 5178 - 5189 (2014).

B. Golman, W. Julklang, Study on Spray Drying for the Production of High Value Particles, Chemical Engineering Transactions, Vol. 39, accepted for publications (2014).

Referred Proceedings of International Conferences

W. Julklang, B. Golman, Influence of operational conditions on the drying kinetics of a slurry droplet in a spray dryer, TIChE International Conference 2012, October 25 26, 2012, Nakhon-Ratchasima, Thailand.

W. Julklang, B. Golman, Study of heat and mass transfer during falling rate period of spray drying of a slurry droplet with nanoparticles, Pure and Applied Chemistry International Conference (PACCON2013), January 23-25, 2013, Chon Buri, Thailand Proceedings of Pure and Applied Chemistry International Conference 2013, p. 441-444.

B. Golman, W. Julklang, Analysis of drying kinetics of a slurry droplet in the falling rate period of spray drying, ICNCE 2013 : International Conference on Nano-engineering and Chemical Engineering, Rome, Italy, September 26-27, 2013.

Curriculum Vitae

Dr. Boris Golman completed his graduate studies in Chemical Engineering at the D.Mendeleyev University of Chemical Technology in Moscow, Russia, and in Chemical Environmental Engineering at the Kitami Institute of Technology, Kitami, Japan. He obtained his Ph.D. in Materials Science and Engineering in 1998 at the Hokkaido University, Sapporo, Japan.

He worked as Researcher at the All-Union Institute of Petrochemical Industry in Moscow between 1983 and 1985, Assistant Professor at Hokkaido University from 1988 to 1996 and Visiting Research Fellow at Science and Technology Research Center of Mitsubishi Chemical Holdings Group in Yokohama from 2006 to 2010. Currently he is working as Assistant Professor of Chemical Engineering, Suranaree University of Technology, Nakhon Ratchasima, Thailand.

He has published more than 75 research articles in referred journals and conference proceedings on powder technology and materials engineering related areas.

His research interests are in the areas of production of functional particles, powder flow, mathematical modeling of powder processing and reaction processes.